Terrestrial radio remote sensing of the upper atmosphere

Koh, Kuang Liang

Award date:
2018

Awarding institution:
University of Bath

Terrestrial radio remote sensing of the upper atmosphere

Kuang Liang Koh

A thesis submitted for the degree of Doctor of Philosophy

University of Bath
Department of Electronic and Electrical Engineering

May 17, 2018

ACKNOWLEDGEMENTS

Without the guidance and advice of my supervisor Martin Füllekrug I would never have made it this far. Thanks also go to my second supervisor, Robert Watson, everyone I've worked with and consulted, family and friends who have supported and encouaged me throughout.

Abstract

The upper atmosphere contains a layer of conductive gas that is the D region ionosphere. The D region is affected by various sources that originate both from Earth and the lower atmosphere and also from space. Yet, there are few methods to study this region due to its altitude. This PhD sets out to improve on the existing widely used sub-ionospheric radio remote sensing method. Existing observations typically use a 20 ms time resolution such that the narrowband transmissions monitored can be approximated to a single frequency. A new, 1 μs time resolution technique is detailed in this thesis that is able to show the frequency response and the fast variability of the transmission propagation. The new technique was applied with transmissions at multiple frequencies yielding experimental results that (1) suggest a new mechanism of ionospheric perturbation by thunderstorm electrostatic field and; (2) provide the first observations of the frequency dependence of wide angle sprite scattering. This technique can be applied to further observations in support of the ASIM and TARANIS space missions to study upper atmospheric lightning. More generally, it can also be applied to the studies of D region processes and other sources of ionospheric perturbations.

Contents

Chapter 1

Introduction to the thesis

The upper atmosphere and more specifically, the mesosphere, lower thermosphere region ∼50–95 km is affected by many processes of terrestrial, extraterrestrial or even extrasolar origins [Silber and Price, 2017, and references therein]. This region is also the lowest layer of the ionosphere, the D region. The ionosphere is a layer of conductive gas that forms the atmospheric global electric circuit and has a number of effects on weather processes in the lower atmosphere [Williams and Mareev, 2014]. The D region can thus be said to be the connection between terrestrial weather and space weather. However, this is also a region of the atmosphere that is most difficult to study. The altitude is too high for most direct measurements except by rocket or balloon measurements, but too low for detailed observation by satellites. Rocket and balloon measurements can only sample discrete points in space or time and hence cannot provide a big picture view. Sub-ionospheric radio remote sensing is a technique that is able to achieve continuous observation of large portions of the D region at once. This can reveal long term trends which are important in climatological studies [Clilverd et al., 2017]. However, to obtain D region parameters from sub-ionospheric radio observations, complex modelling of the radio propagation is required. The modelling is an inversion problem that is neither absolute nor linear, usually ill-posed and will not yield unique solutions [Sechrist, 1974]. The observations are also integrated measurements over long paths hence having poor spatial resolutions. This is particularly problematic for localised ionospheric perturbations such as those from thunderstorms.

Ionospheric perturbations related to thunderstorm electrical activity manifest as

spectacular optical phenomena [Franz et al., 1990, Fukunishi et al., 1996, Pasko et al., 2002, Pasko, 2003]. These are upper atmospheric lightning discharges that were first postulated by [Wilson, 1924], but only recently observed. They result from interactions between the strong electric fields above thunderstorms and the conductive gas of thte D region. γ-ray flashes of terrestrial origins have also been linked to the presence of the thunderstorm electric field [Fishman et al., 1994]. These phenomena are the motivation for the planned space missions, ASIM and TARANIS [Blanc et al., 2007] with objectives to provide detailed observations of upper atmospheric thunderstorm electrical activity from space. Lightning electromagnetic emissions can propagate as whistler mode waves to interact with radiation belt particles causing the electron to precipitate into the D region. This is potentially a significant loss mechanism for radiation belt electrons [Gemelos et al., 2009, Bourriez et al., 2016]. This is important for satellite operations as they can be affected by conditions in the radiation belts.

Moreover, thunderstorms and lightning can be a threat to life and property through flash floods, strong winds and lightning damage. There are also indirect effects on health [e.g. Elliot et al., 2014] and climate [Schumann and Huntrieser, 2007]. Yet, there are still many unknowns about thunderstorms. Their electrification process for example [Saunders, 2008], leading to conflicting results in climate modelling studies [Romps et al., 2014, Finney et al., 2018]. Another unknown is the electric field that exist in the thundercloud and the initiation of lightning. Electric fields that have been measured in the thundercloud are not high enough to support conventional dielectric breakdown for lightning initiation so that the mechanism for the initiation of lightning leaders is still a mystery and subject to active research [Dwyer and Uman, 2014, Rison et al., 2016, Chilingarian et al., 2017].

The thesis sets out to improve on existing techniques for sub-ionospheric radio analysis with the proposed application of investigating thunderstorm electrical effects on the D region ionosphere. Existing measurements of sub-ionospheric narrow band man-made VLF radio transmissions is performed with $\sim$20 ms time resolution which approximate the transmissions to a single frequency. A high time resolution signal processing technique was developed and used to observe thunderstorm related disturbances.

1.1 Thesis structure

This thesis is submitted in the alternative format such that the main findings of the PhD are included in paper format intended for journal publication. Nevertheless, the next chapter provides a background to the results. It contains a review of the existing theory behind various phenomena related to thunderstorms and lightning effects on the lower ionosphere. This is discussed together with observations reported in the literature and is essential for the interpretation of the experimental results obtained. More detailed discussions are included in the papers attached. A description of the signal processing techniques is also given. The main signal processing techniques are described in the papers presented in the next chapters. The result of this PhD are split into three papers, each with a commentary preceeding the paper. The papers are:

1. "Lower ionosphere effects on narrowband VLF transmission propagation: fast variabilities and frequency dependence"; This paper was accepted in Radio Science and serves to introduce the signal processing and the interpretation of the outputs together with some initial results.

2. "Lower ionospheric conductivity modification during a convection surge"; This paper is in draft form prepared for submission.

3. "Multi-frequency observations of Early sub-ionospheric radio disturbances caused by lightning"; This paper is also in draft form prepared for submission.

Some concluding remarks are given in the final section of this thesis.

Chapter 2

Background

2.1 Earth's atmosphere

The atmosphere is a layer of gas that is bound to the Earth by its gravity field. This creates a horizontally stratified atmosphere of pressure and density that decreases roughly exponentially with altitude. The temperature of the atmosphere also exhibits strong altitude dependence and layers in the atmosphere are defined in meteorology by their temperature profile. The layer closest to the Earth's surface, the troposphere, has temperatures that generally decrease with height. The stratosphere, just above the troposphere, has a temperature profile that increases with height. Similarly, the layers above, the mesosphere and thermosphere, are also distinguished by changes in the temperature gradient. The temperature, pressure and density of the atmospheric gases influence many of the phenomena in the atmosphere.

The atmosphere is also increasingly ionised above the stratopause ($>$50 km) such that it can be considered to be conductive[1]. This conductive gas produces effects that are studied in different fields: (1) atmospheric winds in the conductive gas produce short term variations in the magnetic field around Earth; (2) it forms a spherical capacitor with the Earth's surface forming a atmospheric global electric circuit; (3) it provides a reflecting layer hence forming a waveguide for long range radio propagation. This ionised atmosphere is called the ionosphere and has

[1]Lower atmospheric gases are weakly ionised and carry part of the Wilson current. However, they can be considered to be non-conductive for radio waves.

layers, D, E and F regions distinguished by peaks in ionisation that are produced by the absorption of ionising radiation. The absorption rate is different for the various ionising radiation components and is balanced by chemical recombination processes that remove electrons leading to the formation of the ionisation peaks of each layer. The atmospheric thermodynamic properties determine a scale height that affects the peak electron concentration and the height at which this peak occurs. Other factors that may influence these characteristics are the solar zenith angle and the intensity of the radiation for example [Budden, 1988, section 1.5].

Of interest in this work is the lowest layer, the D region of the ionosphere where the ionisation is dominated by solar lyman-α. Since solar radiation is only present during the day, D region ionisation has a strong diurnal pattern. The D region extends downwards and is more conductive at a given height in the day. At night, the D region is higher in altitude and the conductivity gradient is sharper (i.e. it increases at a faster rate). The full theory governing the formation of each layer is described in [Rishbeth and Garriott, 1969].

2.2 Sub-ionospheric radio propagation

Radio waves are radiated from different sources of the surface of the Earth, man-made transmissions and lightning for example. When considering wave propagation, only the frequencies 10–500 kHz is considered in this thesis as in this frequency range, the ionosphere acts as a conductive layer such that most of the radio energy incident on the ionosphere would be reflected back towards Earth. This traps the radio energy in the cavity between the Earth and the ionosphere and is the mechanism for radio propagation beyond the horizon. The conducting surfaces of the Earth and the ionosphere can be described as a waveguide. The propagation of electromagnetic waves can be determined by solving Maxwell's equations, but for the Earth ionosphere waveguide this is not a trivial problem. Several strategies have been developed and the easiest one to illustrate is the mode theory. Assuming first that the ionosphere is a sharp conductive surface. Therefore, a plane wave obliquely incident on this surface would be reflected back down to Earth. The reflected wave would in turn be obliquely incident on the Earth's surface and reflect back up to the ionosphere. This second reflected wave must be consistent with the original plane wave to satisfy the boundary conditions which

requires

$$R_i R_g e^{-2ikh\sin\theta} = 1 \tag{2.1}$$

which is the fundamental equation of mode theory [Budden, 1988, equation 8.4]. The variables R_i and R_g are the reflection coefficients at the ionosphere and ground respectively, $k = \frac{\omega}{c}$ is the wavenumber, h is the height of the ionosphere and θ is the angle of the wave normal with the reflecting surface. This wave propagating in the waveguide can thus be described simply as the summation of two crossing plane waves, one is the first plane wave and the other is the first reflected wave. Since $\sin\theta$ is cyclical, there can be many modes, each formed by two crossing plane waves. This mode theory can be extended to consider more realistic scenarios like a stratified ionosphere and the curved surfaces of the waveguide, but will not be discussed here.

When considering reflection of radio waves off the ionosphere, the electrical properties of the ionospheric gas is important. This is defined by the number density and collision frequency of the electrons and ions. An important quantity in when considering plasma conductivity is the plasma frequency ω_N which is proportional to the number density $\sqrt{N}$. For electrons,

$$\omega_{Ne}^2 = \frac{N_e e^2}{\varepsilon_0 m_e} \tag{2.2}$$

, where e is the electronic charge, N_e and m_e are the number density and mass of electrons respectively and ε_0 is the permittivity of free space. This defines the contribution of the electrons to the charge polarisation in the plasma. The permittivity of the plasma can be defined as

$$\varepsilon = n^2 = 1 - \frac{\omega_{Ne}^2/\omega^2}{1 - iv_c/\omega} \tag{2.3}$$

where v_c is the collision frequency, ω is the wave frequency, and n is the refractive index (approximating the relative permeability$\mu = 1$). The magnetic field is assumed to be negligible. The same can be found for the contribution of ions, but since the mass of ions is many times larger, the plasma frequency is low. Thus for most wave frequencies $>$15 kHz (the frequencies used in this thesis), this contribution is usually not significant [Cummer et al., 1998, section 3.2]. It can be seen that both the fundamental equation of modal propagation and

the refractive index of the ionosphere and hence the reflection coefficient R_i are frequency dependent.

The propagation of radio waves in the Earth ionosphere waveguide is called sub-ionospheric propagation. It is seen from equations 2.1 and 2.3, that this propagation is dependent on the ionospheric conductivity profile. Since the surface of the Earth is relatively constant in time, sub-ionospheric radio propagation can be used as a method to observe changes in the ionospheric conductivity. Conveniently, a number of countries operate high power long range naval communication transmissions at VLF (typically 15–30 kHz) with relatively stable amplitude and phase characteristics. These transmissions can be observed at remote sites to probe the lower ionosphere, for example, to determine its height during different periods [e.g. Thomson et al., 2011, 2017]. LF/MF (30 kHz–3 MHz) transmissions have also been used [Farges et al., 2007, Higginson-Rollins and Cohen, 2017]. The transmissions monitored are usually phase modulated transmissions, with many using the Minimum Shift Keying (MSK) modulation scheme. Observations are made with typically 20 ms sampling time resolution (or decimated to be equivalent to 20 ms resolution) and approximate the transmission to a single frequency. MSK transmissions actually have multiple frequency components so that both carrier phase and the group delay can be measured. Polarisation of the sub-ionospheric radio waves have also been measured to change during disturbances of different origins [Gross et al., 2018]. Sub-ionospheric radio remote sensing has also been applied using lightning, by looking at the frequency response of the propagation [Cummer et al., 1998], and using the time delay between the ground and successive sky waves [Lay and Shao, 2011].

2.3 Thunderstorms and their effect on the lower ionosphere

Thunderstorms are an essential part of the atmospheric global electric circuit as they provide the electromotive force that maintains the potential gradient. During convection, the collisions between ice and graupel particles in the mixed phase region (0 °C or ∼4 km altitude in the summer) imparts positive charge to the lighter ice crystals and negative charge to the heavier graupel particles in general. The

lighter ice crystals are lofted above the graupel in the convective updraught thus setting up distinct charge regions in the thundercloud. Although other mechanisms are possible, this non-inductive process is likely to be the dominating mechanism in thundercloud charging [Saunders, 2008, and references therein].

Build up of charges in each charge region leads to an increasing electric field that eventually discharges in the form of lightning. This is commonly explained by convention gas breakdown physics where the electric field strength becomes large enough to overcome the ionising energy of the gas molecules in air. However, empirical observations so far have not indicated that electric fields in thunderstorms approach the breakdown field. Additional factors have been proposed in attempting to bridge this gap, for e.g., secondary electrons from cosmic rays feeding a relativistic runaway breakdown process [Gurevich et al., 1992] and field enhancement by hydrometeors, but a satisfactory explanation remains elusive.

The thundercloud electric field also exists outside the cloud. In particular, the electric field extends above the thunderstorm, decreasing in strength with distance from the cloud. The thunderstorm charge structure can be approximated to a vertical dipole[2], so the field above is proportional to r^{-3}, where r is the vertical distance above the thunderstorm. The conventional gas breakdown threshold field, E_k, however, decreases at an even faster rate. E_k is proportional to pressure and since the atmospheric pressure decreases with altitude at an exponential rate, E_k decreases similarly. Without considering other factors, the thunderstorm electric field should exceed the conventional breakdown field E_k [Pasko, 2010, figure 2] and produce a discharge somewhere above the thunderstorm - a scenario that was first considered by [Wilson, 1924].

Normally the thunderstorm electric field arising from the cloud charge structure induces screening charge at the bottom of the conductive ionosphere so that it does not penetrate to altitudes where it can cause breakdown. However, it is possible for the thunderstorm electric activity to influence lower ionospheric conductivity via a number of mechanisms; (1) heating from thundercloud electrostatic field; (2) heating via lightning ElectroMagnetic Pulse (EMP) or QuasiElectrostatic (QE) fields set up from lightning charge moment change and; (3) heating and ionisation via lightning EMP or QE. These mechanims will be described in more detail in

[2]Only crude approximation for illustration, the charge structure is complex in reality. Especially for large systems, supercells and MCSs for example

the sections 2.3.2 and 2.3.3 below.

2.3.1 Observation of Early events

The D region ionosopheric perturbations associated with these mechanisms are localised in time and space such that it is difficult to observe except with sub-ionospheric radio remote sensing. Important features of disturbances on sub-ionospheric radio related to thunderstorm electrical activity are the rise and recovery times and the onset delay times. The rise times are typically rapid compared to the recovery times. The onset delay refers to the time between an identified causative lightning and the start of the disturbance rise time. For brevity, disturbances with short onset delays $<$20 ms will be referred to as 'Early events' and disturbances with longer delays as 'Trimpis' in this chapter. This terminology is used to describe the phenomenology whilst avoiding association with any particular physical mechanism.

Initial observations of lightning related disturbance events were associated with energetic electron precipitation triggered by whistler mode waves originating from lightning electromagnetic radiation [Voss et al., 1984, 1998, Inan et al., 2007]. These were referred to as Trimpis and exhibited onset delays that were attributed to the propagation time of the whistler mode wave to the radiation belts and for the electrons to precipitate along the magnetic field lines into the lower ionosphere. This onset delay is thus dependent on the geomagnetic latitude; the propagation path is longer for higher latitudes (higher L shells) [Inan et al., 2010, section 2]. Later observers recognised that some Trimpi events had delays that were less than the time resolution of measurement at the time (100 ms) such that the electron precipitation mechanism was implausible [Armstrong, 1983]. These were later categorised as Early events and suggested to have a more direct mechanism [Inan et al., 1988]. Early events are also observed to have a larger variation in their recovery times ($\sim$10–200 s) compared to Trimpis ($\sim$100–200 s) [Sampath et al., 2000].

2.3.2 Heating by electrostatic field from thundercloud charge

The screening of the thunderstorm electrostatic field reduces its strength but it still exists in the ionosphere. It was proposed that this steady weak electrostatic field could produce a sustained heating effect that is perturbed when lightning discharge produces a sudden change in the thundercloud charge structure, thereby producing Early events [Inan et al., 1996, Pasko et al., 1998a]. The sudden change in the steady heating state should then recover with the re-charging of the thunderstorm which is consistent with the time scales for Early event recovery. This mechanism produces only small changes in the conductivity which cannot explain larger observed Early events. Taking the geomagnetic field into account, a modelling study showed that the conductivity change can be larger at low geomagnetic dip angles [Kabirzadeh et al., 2017].

Sub-ionospheric radio observations using broadband lightning ElectroMagnetic Pulse (EMP), however, does show a relationship between thunderstorm and lightning activity with night time lower ionospheric conductivity variations [Shao et al., 2013]. It was found that the ionospheric conductivity profiles above thunderstorms were different from fair weather periods [Lay et al., 2014]. However, the intermittent nature of lightning EMP means it is not possible to associate the variations with individual lightning discharges and the variations could instead be driven by the slower changes in the thunderstorm cloud charging. This was explored by modelling using detailed chemical kinetics and found to produce significant reductions in conductivity [Salem et al., 2016]. The influence of thunderstorm cloud charging variations is supported by a sub-ionospheric radio disturbance observation that exhibited a rise time of 20–60 s coinciding with a pronounced increase in the weak intra-cloud lightning activity of a thunderstorm near the receiver [Koh et al., 2018c]. The long rise time was attributed to thunderstorm electrostatic field change due to a surge in convection as the updraught produces further charge separation.

2.3.3 Lightning heating and ionisation of the ionosphere and Transient Luminous Events

The screening charge has a relaxation time that is inversely proportional to conductivity so that transient strong electric fields can exist at higher altitudes above the thunderstorm before the screening charge can react. Fast changes in the electric field can be produced by the thunderstorm via lightning discharges. There are two main mechanisms; (1) lightning EMP which is produced by the acceleration of charges and; (2) QuasiElectrostatic (QE) fields that form above the screening layer when thundercloud charge is rapidly neutralised by lightning [Liu et al., 2015, and references therein]. The strength of the electric field in the ionosphere due to EMP should be relative to the current rise time (i.e. charge acceleration) and for QE is related to the change in charge moment.

The existence of transient electric fields in the ionosphere produces heating and ionisation effects. The heating effect of electromagnetic radiation was first recognised from the cross modulation of radio transmissions [Tellegen, 1933]. This mechanism was further investigated using powerful terrestrial VLF radio transmitters producing appreciable heating effects at high altitudes $\sim$80 km [e.g. Inan, 1990, Dowden and Adams, 1992, Barr, 1996]. The heating by radio transmitters at VLF should also be produced by lightning EMP. However, the temperature relaxation times of ionosphere is $<$1 s at $<$90 km altitude so that the heating effect of the short EMP would be brief. Sub-ionospheric radio remote sensing with MF amplitude modulated transmissions appear to be able to detect the EMP heating effect [Farges et al., 2007]. The recovery times of the disturbances are in agreement with the expected temperature relaxation times of $<$1 s.

In addition to heating, stronger fields also produce ionisation which can significantly alter ionospheric conductivity. This can also produce optical emissions, for example, sprites, sprite halos and elves[3] that are collectively termed Transient Luminous Events (TLEs) [Pasko et al., 2012]. Heating and ionisation by QE fields resulting from strong lightning discharges were modelled and found to be consistent with sprite observations [Pasko et al., 1995, 1996, 1997, 1998b, Qin et al.,

[3]The term ELVES is actually an acronym for 'Emissions of Light and VLF perturbations due to EMP Sources' coined by [Fukunishi et al., 1996]. It is not presented as an acronym (i.e. capitalised) in this thesis to be consistent with not giving names to phenomena that will associate a particular physical mechanism.

2011]. The luminosity of sprite plasma is brief, associated with the relaxation of the screening charge to remove the QE field but the relaxation of the excess ionisation produced at sprite altitudes 60–85 km [Gerken et al., 2000] is much slower ∼10–100 s, consistent with Early event observations. The link with sprites led to many studies of concurrent Early events to confirm that sprites are indeed the result of ionisation, but with conflicting results [Koh et al., 2018a, section 1 and references therein]. Halos are another optical phenomenon that are produced by the QE mechanism and were also thought to produce Early events. Using a linear array of receivers (HAIL array), sub-ionospheric radio disturbances were found to agree with an ionospheric conductivity perturbation that is 150 km wide - consistent with a forward scattering pattern from Halos [Johnson et al., 1999, Moore et al., 2003]. Strong EMP is also thought to be able to produce ionisation and optical emissions (elves) [Inan et al., 1991, Taranenko et al., 1993a,b]. From optical observations, elves occur at higher ∼85–95 km altitudes [van der Velde and Montanyà, 2016] than sprites and halos. The altitude meant that for commonly monitored VLF radio transmission frequencies 15–30 kHz, the disturbance produced would not be detectable except for the strongest elves [Koh et al., 2018a, section 8 and references therein]. However, Early events were observed to occur coincidentally with sferic bursts which exhibited slow onsets up to 3 s; this was postulated to be the effect of lightning EMP conditioning the ionospheric conductivity before a subsequent discharge produces a sprite [Haldoupis et al., 2006]. Subsequent modelling predicts that successive lightning EMP may be able to produce such Early/slow events [Marshall et al., 2010]. At such altitudes, the ionisation recovery is thought to be longer and were proposed as the mechanism of LOng Recovery Early (LORE) events [Haldoupis et al., 2013].

2.4 Analysis of atmospheric signals

It is common in engineering to represent signals using the Fourier Transform (FT), i.e., as a sum of sinusoids with different frequencies. This is possible for deterministic signals, the user defined input to a control system for example. However, when a signal is measured there is always a degree of randomness that is associated with some naturally occurring physical process, for example, the Maxwell-Boltzmann distribution of gas particle velocities, Poisson distributed lightning occurence,

Gaussian distributed Johnson-Nyquist noise (electronic thermal noise). Additionally, it is impossible to measure an infinite length of signal as defined in the FT. Therefore, the properties of measured signals are always estimated from a finite length observation which is equivalent to applying a time window to the signal, i.e. $ws(t)$, where $s(t)$ is the time series signal and w is some window function that is only non-zero $t_1 < t < t_2$. The FT can then be applied to the finite length, time windowed signal to estimate its power spectrum.

Previously, analysis of lightning signals was almost exclusively performed using the time series [e.g. Schonland et al., 1940]. A lightning impulse encompasses signals from different processes, the leader and the return stroke for example, that happen in a short duration typically <1 s [Rakov et al., 1994]. Time resolution is thus important in the analysis of such signals. It is possible to perform a short time FT by taking a narrow window. Consider a basic rectangular window $w(t)$ where all samples are given the same unitary weight. The FT of the window can be found analytically as it is a deterministic signal and has a characteristic $\frac{\sin(\omega\tau_w/2)}{\omega\tau_w/2}$ shape, where $\tau_w = t_2 - t_1$ is the time length of the window. This shape is known as the sampling function and is zero where $\frac{\omega\tau_w}{2}$ is an integer multiple of π. The width from the maximum of the sampling function at $\omega = 0$ to the first zero at $\omega = \frac{2\pi}{\tau_w}$ decreases with τ_w. The FT of the windowed signal is the convolution of the signal frequency spectrum with the sampling function for the window. The result is a spreading of the energy from one frequency component onto the neighbouring frequency components (spectral leakage) that is determined by the sampling function. To improve time resolution, τ_w can be made smaller but spectral leakage increases and spectral quality degrades.

To illustrate, consider a signal sampled in time, each sample represents an infinitesimally short duration so that the window period is the number of sample periods, i.e., $\tau_w = (N_w - 1)T_S$, where N_w is the number samples in the window and T_S is the sampling period. The width of the sampling function to the first zero is $\frac{\omega_S}{N_w - 1}$ where $\omega_S = \frac{2\pi}{T_S}$ is the angular sampling frequency. The FT of a signal can be calculated for a single sample but the energy of any frequency component would be spread across the entire spectrum. The corrollary is that the FT of a single sample of a signal has frequency components that all have the same value as the value of that sample and zero phase. Thus, the original time series signal is already the single sample FT for all the samples in the signal.

However, the real valued time series signal is inconvenient for calculations involving phase and frequency. In interferometry for example, sub sample rate timing accuracy can be obtained using phase information [Mezentsev and Füllekrug, 2013, Füllekrug et al., 2014], or signal to noise ratio can be improved [Schimmel and Paulssen, 1997]. A trade-off can be made by sacrificing time resolution but is not ideal. Another strategy is to use the Hilbert transform to convert the real valued signal to a complex analytic signal. The Hilbert transform is used in several different fields, including seismology [Taner et al., 1979]. Its effect can be described as a $\frac{\pi}{2}$ phase shift of negative frequency components and a $-\frac{\pi}{2}$ phase shift of positive frequency components in a real valued signal. The Hilbert transformed signal can then by multiplied the imaginary unit i, which is equivalent to phase shifting the positive frequencies back. Then, the complex analytic signal can be obtained adding this imaginary number to the real valued original signal. This is formulated as

$$s_c(n) = s(n) + i\mathcal{H}\{s(n)\} \tag{2.4}$$

where $\mathcal{H}$ is the Hilbert transform operator and x_c is the complex analytic signal. The amplitude envelope and the phase of this signal can be calculated for every sample of this signal by taking the modulus and argument respectively, i.e. $|s(n)|$ and $\arctan(\frac{\Im(s_c(n))}{\Re(s_c(n))})$, hence, time resolution is preserved whilst phase information is extracted.

In practice, the complex analytic signal can be obtained by taking the FT of $x(t)$ and zeroing the negative frequencies before taking the inverse FT to revert to the time domain. This works by recognising Euler's formula so that a real valued sinusoid can be described using two complex valued exponentials of opposite polarity frequencies, e.g., $\cos(\omega t) = \frac{e^{i\omega t}+e^{-i\omega t}}{2}$. Only the complex valued signal of positive frequency is left after removing the negative frequency. The amplitude of this signal has to be doubled to restore the original signal amplitude. The complex analytic signal can then be described as a summation of complex phasors of positive frequencies as per the complex form of the FT,

$$s_c(n) = \frac{1}{\pi}\sum_{\omega=0} X(\omega)e^{i\omega n T_S} \tag{2.5}$$

. The amplitude $|s_c(n)|$ is thus the resultant amplitude of the sum of the complex phasors of all positive frequency components. Similarly, the phase $\varphi =$

$\arctan(\frac{\Im(s_c(n))}{\Re(s_c(n))})$ is the resultant of all the frequency components. Since the φ can be calculated every sample, an instantaneous frequency can be found from the phase rate of change with time, $f_i = \frac{1}{2\pi}\frac{\mathrm{d}}{\mathrm{d}t}\varphi$.

2.4.1 Narrow band signals and impulsive signals

The instaneous phase of a complex analytic signal with a single frequency is easy to define but it is not so for a signal with multiple frequency components [Bracewell, 1990]. Man-made commnication signals typically modulate information on a carrier wave for transmission. The modulation is designed to be narrow-band and frequency efficient so as to maximise the data rate without interfering other transmissions on adjacent frequencies. For these narrow band transmissions, the amplitude envelope is wide and the phase and instantaneous frequency can be described as representative of the frequency components that are largest and hence exert the most effect on the received signal in the summation of equation 2.5. Many transmissions are continous wave signals (i.e. the amplitude envelope is constant), modulated in phase or frequency. These signals transition from one frequency to another with time, for example, Minimum Shift Keying is a binary frequency modulation scheme where the transmitted frequency is at one of two sideband frequencies at any time [Pasupathy, 1979]. The instantaneous frequency is hence the transmitted frequency that changes with time and the phase is always defined. Amplitude modulated transmissions can be described as a single frequency component with varying amplitude, hence the instantaneous frequency is simply a constant at the carrier frequency but the amplitude envelope changes with time. For amplitude modulated transmissions that modulate to 'off', the instantaneous frequency and phase are undefined during the 'off' symbols [Koh et al., 2018c, section 3].

The radiated electric field from a lightning return stroke for example, has a continuous spectrum that displays a series of peaks and troughs in an interference pattern that is dependent on the propagation distance [Liu et al., 2018, figure 1]. Such signals exhibit rapid changes in instantaneous frequency and phase . In such cases, φ and f_i can be undefined when $|s_c(n)|$ is small. Only when the amplitude envelope is largest can the instantaneous frequency and phase be said to represent the dominant frequency components of the signal. This makes sense as the signal

to noise ratio is best at the highest amplitude.

The cross-correlation of two signals s_1 and s_2 can be calculated as

$$\Phi_{1,2}(m) = \left| \frac{1}{M} \frac{\sum s_1(n) s_2(n+m)}{\sum |s_1(n)||s_2(n+m)|} \right| \tag{2.6}$$

and can be considered as a minimisation of the least squares difference between s_1 and s_2. This produces a sharp peak for wide band signals. However, for narrow band signals, the cross correlation produces broader, less defined peaks. Hence, for wideband signals, the peak of the cross-correlation coefficient is a good estimate of the delay of s_1 relative to s_2. This delay can also be understood as the gradient of the phase frequency response, or group delay and is a single value across all frequencies for a simple time delay. However, it can vary with frequency, in which case the phase frequency response is non-linear. This non-linearity can be seen even over a narrow bandwidth [Koh et al., 2018b, figure 3] and results in a distortion of the signal. In this scenario, since the cross-correlation gives a time delay, it can be considered as giving a linear estimate of the phase frequency gradient. However, the resolution of the cross-correlation is limited to the sampling time resolution. The value of the cross-correlation coefficient peak can be also understood as the coherence between s_1 and s_2 [c.f. Füllekrug et al., 2016, equation 2] so that the comparison of the similarity of two signals can be quantified.

Bandpass filtering can be applied to isolate narrow band transmissions, however, some proportion of wide band noise will be present in the transmission bandwidth. For example, lightning interference on filtered narrow band transmissions. Even in the absence of obvious wide band noise sources, there is always some variability in sub-ionospherically propagation radio transmissions that has been attributed to changes in the ionosphere [Koh et al., 2018b].

Chapter 3

Lower ionosphere effects on narrowband VLF transmission propagation: fast variabilities and frequency dependence

Commentary

Investigating the instantaneous phase and frequency of the complex analytic signal from a man-made narrowband VLF transmission that has been frequency shifted to its carrier frequency, it was noticed that the frequency of Minimum Shift Keying (MSK) modulated transmissions shifts between two values centred about zero. When viewed in the complex plane, the movement of the complex analytic signal vector would be clockwise or anti-clockwise reflecting a positive or negative instantaneous frequency. Using interferometric methods on a novel small array, [Füllekrug et al., 2015] found that the wavenumber of one such transmission exhibited a similar shift synchronous with the frequency shifts between positive and negative. Recognising that the frequency shift originates from the transmission, this paper proposes that the changing wavenumber is due to a surprising frequency dependence of the wave propagation even though the frequency shift of the transmission is only 100 Hz (<5% of the carrier frequency).

Further, using a 1 MHz sampling rate radio receiver and the complex analytic signal, a detailed analysis of the instantaneous phase and frequency shifting of

the MSK transmission was carried out. It was found that the exact modulation scheme used is Gaussian MSK (GMSK), a more frequency efficient variant of MSK. GMSK differs from MSK only around transitions between the positive and negative frequencies, so if the transitions are ignored they are effectively the same. Previous analysis of these transmissions uses a demodulation algorithm from communications engineering that produces outputs with time resolution limited by the signalling rate of the transmission (usually 5 ms) so that the transitions are not considered. A method is described in this paper where the GMSK transmitted signal is modelled using the demodulated received information. The modelled transmitted signal can be compared to the received signal so that the residual can be attributed to propagation effects from the ionosphere. This process can be thought of as an interferometric method with two stations, one is the received signal and the other is the modelled signal. A number of outputs can be obtained; (1) a 'full resolution' amplitude and phase disturbance signal that is computed for each sample of the received signal; (2) a 1 s distribution can be found from the full resolution signal from which the statistical mode and standard deviation can be determined and; (3) a propagation frequency response from the transfer function of the received and modelled signal.

Using both the small array dataset from a short period and a single station recording of night to day change, the original contributions of this paper are:

(1) A non-linear propagation frequency response is seen on a narrow band VLF transmission. Both amplitude and phase frequency response is seen to change with the night to day transition. Most existing measurements approximate the transmission to one frequency and so cannot observe frequency dependence. Frequency dependence has been reported but using only the two frequencies (ignoring the transitions) [Adams and Dowden, 1990] or only for phase [Gross et al., 2018].

(2) Fast variabilities are seen in the full resolution signal not associated with the transmission. These variabilities change with time and are attributed to ionospheric variability. The fast variabilities were highlighted in [Füllekrug et al., 2015] but not seen to change over a longer period. No other reported methods can observe this.

This declaration concerns the article entitled:									
Lower ionosphere effects on narrowband VLF transmission propagation: fast variabilities and frequency dependence									
Publication status (tick one)									
draft manuscript		**Submitted**		**In review**		**Accepted**	✓	**Published**	
Publication details (reference)	Kuang Liang Koh, Zhongjian Liu, and Martin Füllekrug. Lower ionosphere effects on narrowband VLF transmission propagation: Fast variabilities and frequency dependence. Radio Sci., 2018. doi: 10.1002/2017RS006456.								
Candidate's contribution to the paper (detailed, and also given as a percentage).	The candidate contributed to/ considerably contributed to/predominantly executed the… Formulation of ideas: 90% The use of the Hilbert transform to obtain instantaneous frequency and phase from the received data was developed with Z.L and M.F. M.F. provided direction on the application of the method. Design of methodology: 100% Experimental work: 80% The array data originated from a separate experiment conducted by M.F. and Andrew Mezentsev. Presentation of data in journal format: 100%								
Statement from Candidate	This paper reports on original research I conducted during the period of my Higher Degree by Research candidature.								
Signed					**Date**				

Lower ionosphere effects on narrowband VLF transmission propagation: fast variabilities and frequency dependence

Kuang Liang Koh[1], Zhongjian Liu[1], Martin Füllekrug[1]

[1]University of Bath, Centre for Space, Atmospheric and Oceanic Science, Department of Electronic and Electrical Engineering, Bath, UK.

Key Points:

- Non-linear frequency dependence in the sub-ionospheric wave propagation of a VLF transmission
- Wave propagation variabilities faster than 5 ms are shown on an equivalent single receiver recording

Corresponding author: Kuang Liang Koh, k.koh@bath.ac.uk

Abstract

The man-made narrowband VLF transmission from Rhauderfehn, Germany is studied using high accuracy, micro-second time resolution measurements in Bath, UK. The high time resolution enables a novel comparison of the measurements with a detailed simulation of the transmitted signal. It is found that the wave propagation frequency response exhibits non-linear amplitude and phase changes with frequency over the narrow transmission bandwidth during the time of the measurements (13 May 2011 15:00:03–15:00:09 UTC). The high time resolution also enables measurements of fast variabilities in the wave propagation <5 ms. The fast propagation variabilities are likely to originate from integrated ionospheric variability over the propagation path or fast ionospheric processes. The wave propagation frequency response measurement has potential benefits in the study of the lower ionosphere, in particular during highly variable perturbations such as those caused by lightning.

1 Introduction

The lower ionosphere D and lower E region from ~50-90 km altitude exhibits significant spatial and temporal variations driven by a number of phenomena such as lightning discharges, neutral atmosphere and solar variabilities, space weather etc. Such events are difficult to observe with sufficient coverage due to the altitude range which can only be reached from the ground by rockets but which is too low for satellites. Remote sensing methods can address this challenge and the propagation of VLF radio waves (3-30 kHz) in the Earth-ionosphere waveguide provide a convenient way to observe conductivity perturbations in the lower ionosphere [e.g. *Barr et al.*, 2000; *Rodger*, 2003; *Inan et al.*, 2010; *Silber and Price*, 2017, and references therein].

In particular, thunderstorms produce localised conductivity perturbations via a variety of mechanisms. Lightning-induced electron precipitation events have been identified from disturbances on man-made narrowband VLF transmissions [e.g. *Helliwell et al.*, 1973]. Another class of disturbances was identified with similar VLF signatures but without observable delay from the causative lightning discharge - suggesting more direct lightning-ionosphere coupling [e.g. *Armstrong*, 1983; *Inan et al.*, 1988]. These 'early' disturbances sometimes occur simultaneously with transient luminous events (TLEs) such as sprites and elves and it is discussed whether the two are causally linked [e.g. *Rodger*, 2003; *Inan et al.*, 2010; *Haldoupis et al.*, 2013]. Candidate mechanisms for these 'early' disturbances are, for example, quasi-electrostatic effects from lightning discharge induced charge moment changes, and

lightning electromagnetic pulse. Typically, it takes ~5-200 s for 'early' disturbances to recover to undisturbed levels, but 'early' disturbances with longer recoveries (LOREs) have recently been identified [*Cotts and Inan*, 2007; *Haldoupis et al.*, 2012] leading to various studies on potential mechanisms for persistent ionospheric perturbation [*Salut et al.*, 2012; *Haldoupis et al.*, 2013; *NaitAmor et al.*, 2013; *Kotovsky and Moore*, 2016; *Gordillo-Vázquez et al.*, 2016; *Kotovsky et al.*, 2016]. Additionally, thundercloud electrostatic fields have an effect on the lower ionospheric conductivity profile [*Pasko et al.*, 1998; *Lay et al.*, 2014; *Salem et al.*, 2016]. The monitoring of man-made narrowband VLF transmissions is thus relevant to understanding thunderstorm impact on the lower ionosphere and the different physical mechanisms. The complexity of the possible shape and uncertainty about the size and duration of the perturbations and their causative mechanisms drive the need for more detailed measurements and modelling. For example, holographic strip imaging of perturbations using a number of receivers arranged in a line perpendicular to the propagation path was attempted to determine the extent of lightning-ionospheric perturbations [*Chen et al.*, 1996; *Johnson et al.*, 1999; *Moore et al.*, 2003] and various studies have considered Gaussian [*Moore et al.*, 2003; *NaitAmor et al.*, 2017] and column [*Hardman et al.*, 1998; *Marshall et al.*, 2006] shapes.

Existing observations of VLF transmission disturbances are mostly single receiver measurements with ~20 ms resolution. The frequency modulation of the VLF transmissions mean that the transmission switches between two sideband frequencies around the carrier frequency (described further in section 3) - a characteristic that has been used to make dual frequency observations [*Dowden and Adams*, 1989]. However, most observations approximate the VLF transmissions to a monotone at the carrier frequency. Recently, high accuracy, micro-second time resolution small aperture array measurements reveal that the propagation of the VLF transmission signal exhibits variabilities on time scales $\ll$20 ms [*Füllekrug et al.*, 2015b], thus sparking the motivation to investigate the cause of the propagation variabilities. These propagation effects should be observable as VLF transmission disturbances on a single receiver. This work presents a method to derive the VLF transmission disturbances on short time scales which elucidates further details of the multipath propagation and its fast variabilities. The purpose is to push existing techniques for lower ionospheric observation by showing that more physical detail can be inferred from detailed measurement.

The method is described in section 3 and applied to an equivalent single receiver recording derived from the array data so that the propagation variabilities may be investigated

further. The method is shown to be able to extract the variabilities from the equivalent single receiver data in section 4 and that some of the variability is closely associated with the changing frequency content of the transmission. The array processing of multiple high bit-depth, high sampling rate recordings to observe the wavenumber vectors is computationally expensive and so is currently impractical for long term monitoring. Gathering such data is also logistically difficult; array baselines need to be in the kilometre range to make sensible observations of radio waves with wavelengths that are sensitive to lower ionospheric conductivities. Whilst these obstacles are not insurmountable, it is more convenient to use a single receiver. The data gathered with the array was during an arbitrary period when ionospheric conditions were stable, so it is unknown how the propagation variabilities will change with the ionosphere. Thus, analysis of single receiver data (a different dataset to the array) when the terminator is moving along the propagation path was performed with the method. The results are shown in section 5 and illustrate the effect of the diurnal change in the ionosphere on the frequency dependence of propagation.

2 Experimental data

In this study, we use a recording of the VLF transmission from Rhauderfehn, Germany at 23.4 kHz (denoted DHO), averaged from a 10 receiver array situated within a square kilometer area near Bath, UK [*Mezentsev and Füllekrug*, 2013]. The reason for using the array dataset is to investigate the propagation variabilities concluded from the array analysis by [*Füllekrug et al.*, 2015b]. This dataset covers a short arbitrary period when ionospheric conditions were stable.

Each receiver is a wideband vertical electric field sensor that samples every 1 μs, with an amplitude resolution of ~35 μV/m and timing accuracy of ~20 ns [*Füllekrug*, 2010]. The accuracy of the array measurements has been shown to be close to instrumental limits [*Füllekrug et al.*, 2014, section 6]. The time of the recording analysed in this study is a 6 s period from 15:00:03–15:00:09 UTC on 13 May 2011. The size of the array (~1 km^2, with the largest distance between a pair of receivers being ~1260 m) is unique in the study of subionospheric propagation - it is much smaller than either the distance from the transmitter (~700 km) or the wavelength (~13 km). This means the wavefield travelling over the array can be approximated with a plane wave. The recordings can be aligned in time by multiplying with a reference plane wave, $e^{i\boldsymbol{k}\boldsymbol{r}_l}$, where $\boldsymbol{k}$ is the wavenumber vector and $\boldsymbol{r}_l$ is the position vector of each receiver with index l in the array.

Additionally, each recording is frequency shifted so that the angular transmission carrier frequency ω_c is at baseband after multiplying with a phasor $e^{-i\omega_c}$ and subsequently a low-pass filter is applied to isolate the transmission of interest. This produces narrowband complex analytic signals, $y_l(t)$, of the baseband transmission from which the amplitude and phase can be computed for each individual sample. These signals are finally averaged across all receivers in the array.

$$y_r(t) = \frac{1}{L}\sum_{l=1}^{L} y_l(t) e^{i\boldsymbol{k}\boldsymbol{r}_l}. \tag{1}$$

The proximity between the receivers in the array (<1260 m) mean that the signal sampled by each receiver is from approximately the same propagation path. Thus, the result can be considered as a recording from an equivalent single receiver.

Man-made sources of interference present in the data (for e.g., the sources between ~20 to 250 kHz documented in [*Füllekrug et al.*, 2015a]) are already effectively removed by the narrowband filter applied. Natural sources of interference in the data are weak lightning signals from far away storms (>900 km away [*Füllekrug et al.*, 2016]). Most of the electromagnetic energy radiated by lightning is centered around 10 kHz. Additionally, higher frequencies from sferics attenuate faster with distance so that the far away sferics in the filtered data are of small amplitude. This noise is further reduced by the averaging process, although the effect is small - all the results obtained with the equivalent single receiver data are similar to results computed with only the data from one receiver in the array. This may not always be the case in general and there may be periods when there is strong sferic interference. The effect of strong sferic interference is considered in section 3.

The derivation of ionospheric perturbation signals from disturbances on VLF transmissions requires an understanding of the source field - the detailed model of the VLF transmission used in this work to extract the transmission disturbances is described in section 3. A key assumption of this method is that the transmission at source is exactly as described by the model. The assumption is largely valid as transmissions follow a known modulation scheme. In practice, VLF transmissions such as DHO are operated for broadcast communications purposes and only to the accuracy required by their specific purpose and thus have unknown imperfections.

Existing long term observations note that VLF transmissions have good amplitude and phase stability, although this is not always the case. There may be periods when there are random phase jumps in the transmission, or the transmission clock is not locked to a fre-

quency standard and the transmission experiences a frequency drift [*Thomson et al.*, 2011a]. For example, the frequency of DHO has been reported to vary by a small fraction (<100 μHz) of its published centre frequency of 23.4 kHz [*Thomson et al.*, 2017]. In this case, the phase disturbance calculated (see section 3) would ramp in time with a gradient equivalent to $\Delta\omega$, the angular frequency difference between the assumed centre frequency and the actual transmitted centre frequency. Over a 1 s processing period, its effect is <0.036°, i.e., around a magnitude smaller than the variabilities seen in the results and so is not significant in this work. There are also no amplitude or phase jumps in the data used.

3 Measurement of VLF transmission disturbances

A modulation scheme common amongst VLF transmissions is Gaussian Minimum Shift Keying (GMSK) - a spectrally efficient variant of Minimum Shift Keying (MSK). MSK transmissions can be described in complex notation as $Ae^{i\phi(t)}e^{i\omega_c t}$, a signal with time-varying phase $\phi(t)$ (which contains the message) but constant amplitude A. The amplitude of the received transmission is understood as an indicator of the ionospheric disturbance signal, assuming that the variations of the source amplitude of the transmitted signal are small.

The time-varying phase from the transmitted message has to be removed to get the phase disturbance. Specifically for MSK, the message $m(t)$ is encoded in $\phi(t)$ so that

$$\phi(t) = \frac{\omega_s}{4}\int_{-\infty}^{t} m(t)\,\mathrm{d}t, \tag{2}$$

where $m(t)$ is a sequence of symbols represented by either positive or negative unity values. The length of each symbol in the sequence is $T_s = 1/f_s$, where $f_s = \omega_s/2\pi$ is the symbol rate. The angular baseband frequency can be derived using

$$\omega(t) = \frac{\mathrm{d}}{\mathrm{d}t}\phi(t) = \frac{\omega_s}{4}m(t) \tag{3}$$

where ω can only be one of two values since m can only be either positive or negative unity, i.e.,

$$\omega = \begin{cases} +\frac{\omega_s}{4} & \text{when } m = 1 \\ -\frac{\omega_s}{4} & \text{when } m = -1 \end{cases} \tag{4}$$

Therefore, a MSK transmission can be considered to be a special case of frequency shift keying where the message is transmitted by the pattern of switching between two specific sideband frequencies, $\pm\frac{\omega_s}{4}$, spaced $\frac{\omega_s}{2}$ apart. The two sideband frequencies are symmetric around the carrier frequency so that at baseband they have opposite polarities. A Gaussian

filter is applied to smooth the symbol transitions to improve spectral efficiency. Specifically, equation 2 becomes

$$\phi(t) = \frac{\omega_s}{4} \int_{-\infty}^{t} m_g(t)\, \mathrm{d}t, \tag{5}$$

where $m_g(t)$ is the Gaussian filtered $m(t)$. This variant of MSK is known as GMSK.

The instantaneous frequency of the received signal, $f_i = \omega_i / 2\pi$, can be calculated from the received phase $\phi_r = \arg(y_r) = \arctan(\frac{\Im(y_r)}{\Re(y_r)})$, given $\omega_i = \frac{\mathrm{d}}{\mathrm{d}t}\phi_r(t)$. The symbol sequence $m(t)$ can be inferred from the polarity of ω_i as per equation 4, which is essentially a demodulation operation. Once the symbol sequence has been determined, it can be modulated using the GMSK scheme as per equation 5 to estimate the transmitted phase $\phi(t)$.

The phase of this estimated transmission for a 300 ms period (15:00:05.485–15:00:05.785 UTC) is shown in figure 1, left panel in solid blue and red lines. Its corresponding instantaneous frequency is shown in the right panel, also in solid blue and red lines. The blue and red colours represent the periods when a '+' or '-' symbol respectively is transmitted and the vertical grid lines delineate each symbol. During a '+' symbol, the phase increases by a rate determined by the positive sideband frequency. For DHO, $f_s = 200$ Hz, so the positive sideband frequency is 50 Hz as per equation 4 - this is shown in the instantaneous frequency in blue. During a '-' symbol, the phase decreases at an equal rate but of opposite polarity to that of a '+' symbol as per the negative sideband frequency (−50 Hz, shown in the instantaneous frequency in red). The phase and instantaneous frequency of the received transmission (shown in the dashed green lines on the same plots) are similar to those of the estimated transmission with small deviations which are more visible in instantaneous frequency (the phase of the estimated and received transmissions are shown with an arbitrary offset for clarity).

The received phase includes a time delay, τ_p, introduced by the propagation from transmitter to receiver. Consider a period $t_1 - \tau_p$ to t_1 when the transmission is transmitting a symbol m_1, than the transmission has a frequency ω_1 in this period. This signal propagates at a phase velocity which has a magnitude at some proportion of the speed of light, the exact value is dependent on parameters of the Earth-ionosphere waveguide at VLF, so that the absolute delay introduced by the propagation is unknown. The phase of the received transmission at t_1,

$$\phi_r(t_1) = \phi(t_1) - \omega_1 \tau_p = \phi(t_1 - \tau_p). \tag{6}$$

This propagation delay can be considered to be composed of a constant part that results from the average geometry of the Earth-ionosphere waveguide and a time variable part produced by changes in the ionospheric conductivity profile.

In practice, the absolute start phase of the transmission is also unknown (equivalent to the integration constant of equation 5) and the transmitted phase is calculated from the received signal which contains the unknown propagation delay τ_p. This estimated transmitted phase is thus $\phi_e = \phi(t_1) - \omega_1\tau_e - C$ where τ_e is approximately the propagation delay and C is the constant offset introduced by the unknown transmission start phase. The actual propagation delay can vary with both time and frequency, i.e. $\tau_p(t, \omega)$, whereas the delay in the estimated transmitted phase (τ_e) is taken to be a single time delay value that can be interpreted as the constant part of the propagation delay. This value (τ_e) is referred to thereafter as the delay estimate. The calculated phase disturbance is thus,

$$\phi_d = \phi_r - \phi_e = \omega_1(\tau_e - \tau_p) + C. \tag{7}$$

Hence, ϕ_d is a relative measure with offset $\omega_1\tau_e + C$.

The received amplitude and phase disturbance can be calculated per sample of the recording, resulting in a very high time resolution (1 μs) observation of ionospheric perturbations via the VLF transmission. This is shown in figure 2 for the same 300 ms period as in figure 1 and using the same format - solid blue and red colours represent the periods when a '+' or '-' symbol respectively is transmitted and the vertical grid lines delineate each symbol. During transitions between the two symbols, the instantaneous frequency is not constant - the samples around such transitions are plotted in grey dashed lines.

During periods when there is strong interference, certain symbols in $m(t)$ from the demodulation can be missed. In the case of a single missing symbol, ϕ_d will be offset by $\gg\frac{\pi}{2}$ after the missing symbol, which makes the detection of such errors relatively straightforward. For example, consider a symbol '+', using equation 2, the transmission phase at the beginning ($t = 0$) and end of the symbol ($t = T_s$) is $\phi(0) = 0$ and $\phi(T_s) = \frac{\pi}{2}$. If the symbol is demodulated as '-', $\phi(T_s) = -\frac{\pi}{2}$. The calculated phase disturbance at the start of the symbol is $\phi_d(0) = 0$ and at the end of the symbol is $\phi_d(T_s) = \pi$. Taking the Gaussian filter of GMSK into account, the offset will be slightly less than π but $\gg\frac{\pi}{2}$ as stated. Such offsets are monitored in the analysis and removed by flipping the polarity of the demodulated symbol at the offset. It follows that disturbances that produce phase offsets of $\geq\pi$ are indeterminate in this

analysis. However, phase changes $\geq\pi$ over time scales of one symbol period (5 ms for DHO) are very rare in the dataset analysed in this study.

In the case of interference lasting over consecutive symbols, the correct symbols cannot be determined. A step change of value π can still be avoided by making an approximation of the symbols, even though ϕ_d is ambiguous over the period of the interference. No such interference is present in the data we examine in this study.

4 Frequency dependence and ionospheric variability

It is important to distinguish the features of the received amplitude and phase disturbance that are VLF radio propagation effects as opposed to local noise or transmitter effects to determine the ionospheric electrical properties over the propagation path. There are two key propagation effects on the signal that have been identified from the array results of [*Füllekrug et al.*, 2015b]; (1) that there are "two distinct source locations in the wave number domain. The source location associated with a positive apparent frequency occurs at a smaller wave number such that it would appear at a larger elevation angle in the radio sky when compared to the source location associated with a negative apparent frequency" and (2) accounting for the distinct source locations, there are faster variabilities <5 ms in the wavenumber vectors.

As described in section 3 and shown in figure 2, right panel, the changing apparent frequency of the received transmission corresponds with the frequency modulation of the transmission. Therefore, the wavenumber vector differences with apparent frequency observed by [*Füllekrug et al.*, 2015b] appears to be a frequency dependence of the propagation. The propagation effect experienced by a signal is a function of the properties of the propagation path. Frequency dependent propagation paths mean that different frequency components of the transmission experience different propagation effects. This should be observed on a single receiver recording as a modulation of the frequency spectrum of the transmission by the wave propagation frequency response. Using the equivalent single receiver data produced from the array dataset, the received amplitude over a 300 ms period is seen to be different between the two sideband frequencies of the transmission as shown in figure 2, left panel, where the blue lines (when the '+' symbol or positive sideband frequency is being transmitted) are consistently higher than the red lines (when the '-' symbol or negative sideband frequency is being transmitted).

Further, the spectrum of the received signal can be compared to that of the transmission (estimated from the received transmission as per section 3) by taking their transfer function to achieve better frequency resolution of the wave propagation frequency response. The frequency spectrum of the received transmission can be described as $Y_r(\omega) = Y(\omega)h(\omega)$ in the frequency domain, where $Y(\omega)$ is the frequency spectrum of the transmission and $h(\omega)$ is the frequency response of the wave propagation. In practice, $h(\omega)$ also contains the relatively constant instrument response. Assuming the estimated transmission to be closely equivalent to the source transmission, then the wave propagation frequency response can be found by taking the transfer function, $h(\omega) \approx \frac{Y_r(\omega)}{Y_e(\omega)}$, where $Y_e(\omega)$ is the frequency spectrum of the estimated transmission and both $Y_r(\omega)$ and $Y_e(\omega)$ can be found by taking the Fourier transform of the received and estimated transmission respectively.

As the absolute transmission amplitude is unknown, a unity value is used for the estimated transmission amplitude, $y_e(t) = e^{i\phi_e(t)}e^{i\omega_c t}$, i.e. the transfer function calculation compares the received signal spectrum to the spectrum of an estimated transmission with unity amplitude. Therefore, the amplitude of the wave propagation frequency response can only be determined relatively with all frequency components scaled by the unknown transmission amplitude A.

The amplitude of the wave propagation response $|h(\omega)|$ calculated over the whole 6 s period of the data is shown in figure 3, left panel. At the positive sideband frequency (denoted by the blue vertical line), the amplitude is higher than at the negative sideband frequency (red vertical line) - consistent with the received amplitude in figure 2, left panel. The sudden changes in the amplitude response with frequency (for example, the prominent 'spike' at ~23.36 kHz) are likely to result from noise of unknown origin. However, the amplitude also exhibits a general non-linear trend over the bandwidth of the transmission. The non-linearity can be approximated to two discontinuous linear sections shown in the figure by the dashed magenta lines - the amplitude varies with a positive gradient up to around the centre frequency where the trend turns into a lower negative gradient.

The phase of the wave propagation response is $\arg(h(\omega)) = \Phi_r(\omega) - \Phi_e(\omega)$ where $\Phi_r(\omega)$ and $\Phi_e(\omega)$ are the received and estimated transmitted phase calculated for each frequency component respectively. When the transmission is at one of the sideband frequencies, ω_1, then $\Phi_r(\omega_1)$ and $\Phi_e(\omega_1)$ are equivalent to ϕ_r and ϕ_e from equation 7 and $\arg(h(\omega_1)) =$

$\omega_1(\tau_e - \tau_p) + C$, i.e., only a relative measurement is possible due to the unknown transmission start phase and propagation delay as discussed in section 3.

Previous observations at the two sideband frequencies [e.g. *Adams and Dowden*, 1990] posits that changes in the phase difference between each sideband frequency of the transmission is due to changes in group delay. In this work, any group delay effect results from a difference between the delay estimate τ_e and the actual propagation delay τ_p. For example, if $\arg(h(\omega))$ is calculated for a length of transmission containing multiple frequencies (i.e., when there are transitions between symbols) then the phase of the propagation response would vary with frequency with a constant gradient equal to $\tau_e - \tau_p$. This phase-frequency gradient produced by group delay is used in many applications to estimate signal arrival times, for example, [*Dowden et al.*, 2002] uses the group delay of sferics in a network of receivers to accurately compute lightning location. The value of τ_e is a single value for all frequencies chosen to be as close to τ_p as possible to minimise the phase-frequency gradient in the results.

The phase of the wave propagation response $\arg(h(\omega))$ calculated over the whole 6 s period of the data is shown in figure 3, right panel. As for the amplitude response, sudden changes in the phase cannot be interpreted as physical as they are likely to be due to noise of unknown origin. However, the phase also exhibits a general non-linear variation. The non-linearity can be approximated to three discontinuous linear sections shown in the figure by the dashed magenta lines - the phase increases up to a maximum at ~23.36 kHz, then it decreases to a minimum at ~24.44 kHz before increasing. This non-linear trend suggests that the propagation delay is frequency dependent, i.e. $\tau_p(\omega)$, even over the narrow 140 Hz bandwidth shown in the figure.

Figure 4 shows the statistical mode of received amplitude (in the left panel) and phase disturbance (in the right panel) every second over the entire 6 s period of the data. The distributions are broken down in time according to which sideband frequency is being transmitted and their statistical modes displayed in blue and red solid lines as per figure 2. The received amplitude and phase disturbance statistical modes for each sideband frequency are shown to be different in figure 4, again suggesting frequency dependence of the wave propagation.

This frequency dependence can originate from the transmitter similar to the stability issues discussed in section 2. For example, frequency dependence can arise from the transmitter antenna being a more effective radiator at one sideband frequency than the other. Such

imperfections in the transmission cannot be observed by existing methods unlike the stability issues discussed in section 2. In such scenarios where the imperfection is systematic, the frequency dependence seen should be constant, but the statistical modes for each sideband frequency vary independently in figure 4 over the 6 s period of the data. Moreover, the array analysis carried out previously on the same data by [*Füllekrug et al.*, 2015b] establishes that the wave propagation is dependent on the sideband frequency of the transmission. Therefore, it is likely that at least part of the observed frequency dependence is a result of wave propagation.

The 1 s time period for the distribution calculation of figure 4 is over several symbols ($\gg$5 ms) so that both sideband frequencies are transmitted in the period and enables the distribution for both sideband frequencies to be calculated for the same second. The relatively long 1 s period is chosen for convenience and shorter processing periods are possible. The samples around symbol transitions are removed from the analysis as the instantaneous transmission frequency during transitions is not constant (these are the samples shown in grey in figure 2). The statistical mode of the distribution is used instead of the mean as it is considered more robust to outlier values, for example, lightning interference. Although weak lightning signals from far away storms can be picked up by the array around the time of recording [*Füllekrug et al.*, 2016], the distributions of the received amplitude and phase disturbance are seen to be roughly normal in shape. An example of the distribution is shown in figure 5 for 1 s of data from 15:00:04 UTC. Since the distribution is roughly normal, the standard deviation σ can be computed from the probability density at the mode of the distribution, a, so

$$\sigma = \frac{1}{a\sqrt{2\pi}}.$$

The standard deviation of the received amplitude and phase disturbance distribution is a measure of their variability in the processing period. The shaded areas in figure 4 represent the standard deviation of each distribution around the statistical mode calculated for each second. The phase disturbance variability in the recording ranges from 0.43-0.80°, equivalent to a delay of 51-95 ns. Since the clock accuracy of the instrument is within 20 ns, ~70% of the variability cannot be attributed to instrumental noise. This is consistent with the array analysis results of [*Füllekrug et al.*, 2015b] which estimates a similar proportion of the wavenumber vector variability calculated from the received phase originates from wave propagation. Further, the recording is averaged over several receivers which reduces the contribution from uncorrelated sources (for e.g., the instrumental clock accuracy) so that the phase disturbance variability that cannot be attributed to instrumental noise is actually >70%. Given that wave

propagation can produce phase disturbance variability of such magnitude, the effects of wave propagation on VLF transmission phase will still be observable with a true single receiver recording under similar conditions. The received amplitude variability (figure 4, left panel shaded area) in the recording ranges from $11.7 - 15.7\,\mu\mathrm{Vm}^{-1}$ which is representative of the instrumental accuracy so is likely to be mostly instrumental.

Transmitter imperfections can also produce fast variabilities. For example, the unknown clock accuracy of the transmitter can produce fast variabilities in the transmitter phase. However, transmitter imperfections will not produce wavenumber scatter so the origin of the fast variability observed here is likely to be wave propagation.

5 Diurnal frequency dependence and fast variability

The sidebands of the DHO transmission are separated only by 100 Hz. Over such a narrow frequency separation, it is unknown how the frequency dependence will change with the lower ionosphere. The D region ionosphere exhibits a predictable, repeated change with the movement of the terminator in the diurnal cycle. Therefore, a separate observation is presented here of the same DHO transmission when the night to day terminator was travelling along the propagation path from 27th August 2016 03:30–07:00 UTC.

During this time, the receiver was operating in a monitoring mode when the data is split into roughly hourly files by automatically restarting the recording process every hour. The restart normally produces a small gap in the data of <30 s, for example 04:28:18–04:28:42 UTC and 06:28:18–06:28:42 UTC. One of the hourly restarts is during the longer ~12 minute gap between 05:20:05–05:32:37 UTC - the extended duration is a result of the automatic processing algorithm disregarding samples with amplitude below a set threshold as unreliable.

On the date of the recording, sunrise time at the DHO transmitter site is 04:31 UTC and 05:14 UTC at the receiver in Bath, UK. Between those times, the terminator was moving from the DHO transmitter site to the receiver. The receiver was located in the University of Bath, UK so that the propagation path from DHO to the receiver is almost the same as to the array.

Figure 6, top panels show the statistical modes of the received amplitudes (left) and ϕ_d (right) at each sideband frequency. The received amplitudes at each sideband is seen to vary by up to $0.5\,\mathrm{mVm}^{-1}$ to during night time conditions before the terminator reaches the DHO transmitter site at 04:31 UTC. After this time, there is a steep monotonic decrease starting

~04:30 UTC that is attributable to the crossing of the terminator. The received amplitudes then stabilises with a small steady increasing trend ~05:30 UTC. It is evident over this few hours that there is a general correlation between the received amplitudes at each sideband but there is a varying difference between them that can be up to 0.6 mVm^{-1} or ~20% of the average value of the received amplitudes. The inset figure in the top left panel shows the differences between the sidebands which are greater and vary more during night time conditions.

Interestingly, the start of the ϕ_d response to the crossing of the terminator appears to lead that of the received amplitude by ~30 minutes, starting around ~04:00 UTC. The phase disturbance ϕ_d increases steadily (faster in the first 15 minutes) until just past 05:00 UTC, again, before the stabilising of the received amplitude by ~30 minutes. Larger variations are also seen in ϕ_d during night time compared to day time conditions. The general correlation between the sideband frequencies is also seen in ϕ_d with the propagation delay (approximately proportional to the difference between the ϕ_d of each sideband frequency) varying more during night time.

The bottom panels of figure 6 show the standard deviations of the received amplitudes (left) and ϕ_d (right) which represent the fast variability of the signals. During night time conditions, the received amplitude variability is larger (~40–60 $\mu\mathrm{Vm}^{-1}$) but during day time conditions the variability is smaller so that the effect is likely to be instrumental in nature (<35 $\mu\mathrm{Vm}^{-1}$, the instrumental noise floor). It is possible that this change in variability is due to the attenuation of variability from the transmitter as the variability change appears to follow the change in received amplitude. However, the variability on both sideband frequencies are similar whilst there is a difference between the received amplitudes. The variability of ϕ_d does drop below 50 ns, very similar to the variability seen in the array dataset (day time). There is a period ~04:45–05:30 UTC where the variability shows an increase up to 250 ns before it decreases again. Again, the variability is seen to be similar between the sideband frequencies.

6 Discussion

The VLF transmission propagates in the Earth-ionosphere waveguide via different wave propagation modes which superpose so that the radio wave amplitude and phase varies spatially when observed on the ground, i.e. they form a modal interference pattern. When the waveguide changes, the radio propagation and hence the modal interference pattern is al-

tered correspondingly. Since the Earth's surface profile and electrical properties can be taken as constant in time, changes in the modal interference pattern are attributed to ionospheric perturbations. For example, measurement of nulls in the interference pattern of VLF transmissions has been used to infer a long term lowering in the altitude of the D region ionosphere linked to an increase in greenhouse gases [*Clilverd et al.*, 2017]. A radio receiver samples the modal interference pattern at a single point, however, the interference pattern can be influenced by ionospheric perturbations anywhere, with the largest influence coming from perturbations along and near the transmitter to receiver great circle path. Therefore, the remote sensing method using VLF wave propagation is effectively an integrated measurement along the transmitter to receiver great circle path. For a sideband frequency of the transmission, i.e. a single frequency component, the propagation variability inferred from the micro-second time resolution received transmission amplitude and phase disturbance may be due to the spatial inhomogeneity of the ionosphere over the path. For example, if the ionospheric variation in time at one point is different from that at another point, the integrated effect over the path are variabilities in the received amplitude and phase disturbance that can be faster than the ionospheric variations at each isolated point. The propagation variability can also be an effect of a fast varying ionosphere as suggested by [*Füllekrug et al.*, 2015b]. Further observations are needed to study the physical meaning of the propagation variabilities. In particular, it is unclear how these variabilities would change with changes in ionospheric forcing over a longer period of time.

From the measured radio signal, the profile of the lower ionospheric electrical properties can be found by solving the inverse radio propagation problem. The radio propagation modelling is usually performed with different electrical property profiles to find a solution that best fits the measured data. To make the process tractable, the lower ionosphere is commonly simplified to a laterally homogeneous, horizontally stratified structure where electron density and collision frequency increase exponentially with altitude z. With this simplification, the ionospheric profile can be described with only two Wait parameters of reference height h' and sharpness β [*Wait and Spies*, 1964]. This approach has been used to estimate stable D region ionospheric conditions using existing lower time-resolution, single frequency measurements of VLF transmissions [e.g. *Thomson*, 2010; *Thomson et al.*, 2011a,b, 2017]. Consider a Wait ionosphere in the absence of a geomagnetic field. The ionospheric plasma has a complex permittivity ϵ that is a function of its electron density, $N_e(z)$, collision fre-

quency $\nu(z)$ and the angular wave frequency ω,

$$\epsilon = 1 - \frac{N_e(z)e^2}{m_e\epsilon_0\omega^2(1 - i\nu(z)/\omega)}$$

[adapted from *Budden*, 1988, chapter 3]. Where e and m_e is the electric charge and mass of an electron and ϵ_0 is the free space permittivity. It follows that the reflection coefficient for each propagation mode and hence the modal interference pattern is dependent on frequency.

Theory and empirical evidence show that over large frequency ranges, the propagation frequency dependence is non-linear [e.g. *Chapman and Macario*, 1956; *Dowden et al.*, 2002]. However, the DHO transmission has a very narrow bandwidth - the separation between the two sideband frequencies is only 100 Hz. This may be representative of a more complex ionospheric profile - for example, rocket measurements reveal a vertical ionospheric profile [*Friedrich and Torkar*, 2001, and references therein] with much more detail than a Wait ionospheric profile and the lateral homogeneity assumption may not always be valid. The ionospheric profile changes depending on the various different forcing effects, for example, the modulation of solar radiation by time producing diurnal changes in the ionospheric profile. This has a significant effect on the frequency dependence of propagation as shown using the single receiver dataset presented in section 5. Ionospheric profiles different to that during the recordings presented here will likely produce different wave propagation responses.

The multi-frequency measurement motivates more detailed propagation modelling in the determination of ionospheric profiles. This can potentially improve resolution of finer features or provide higher certainty or accuracy in the inversion. Such improvements are particularly useful in observing complex perturbations such as those produced by lightning in thunderstorms. Another approach to obtain multi-frequency measurements is to use averaged broadband sferics [*Cummer et al.*, 1998; *Lay and Shao*, 2011], which allow measurements over much larger frequency bandwidths than VLF transmissions. However, the source signal and location of VLF transmissions are more certain than those of sferics. Moreover, the multi-frequency transmission disturbance analysis can achieve better time resolution (1 s) and is able to provide continuous phase measurements when compared to the intermittent lightning.

7 Summary

Observing disturbances on VLF transmissions is a commonly used method to probe conductivity perturbations of the lower ionosphere. Most existing analysis provide single frequency, ~20 ms time resolution observations of the disturbances. This work presents a method to make VLF transmission amplitude and phase disturbance measurements per sample from a 1 μs time resolution record.

The fast measurement is able to resolve the frequency modulation of the VLF transmission and hence observe frequency dependent propagation effects. The multi-frequency measurement can potentially improve reconstructions of the lower ionospheric profile, especially in the study of complex perturbations such as those caused by lightning. Fast variability of the propagation at each sideband frequency of the transmission (<5 ms) can also be observed with the method which may be due to ionospheric variability over the propagation path or fast processes in the ionosphere.

Acknowledgments

The work of K.K. is sponsored by the Engineering and Physical Sciences Research Council (EPSRC) under DTA contract EB-EE1151. The work of Z.L. is sponsored by the University of Bath, UK MetOffice (EA-EE1077) and the China Scholarship Council (CSC) (File 201408060073). The work of M.F. is sponsored by the Natural Environment Research Council (NERC) under grants NE/L012669/1 and NE/H024921/1. This work was partly inspired by the SAINT project of the European Commission (H2020-MSCA-ITN-2016, 722337). The data used for this publication is available from https://doi.org/10.15125/BATH-00464. K.K. wrote the paper and performed the data analysis. Z.L. and M.F. advised on the use of the Hilbert transform calculations to obtain instantaneous frequency and phase from the received data. M.F. supervised the work of K.K. and provided the equivalent single receiver data used in this work. Thanks also go to Andrew Mezentsev who had a hand in collecting the array data.

References

Adams, C. D. D., and R. L. Dowden (1990), VLF group delay of lightning-induced electron precipitation echoes from measurement of phase and amplitude perturbations at two frequencies, *Journal of Geophysical Research: Space Physics*, *95*(A3), 2457–2462,

511 doi:10.1029/JA095iA03p02457.

512 Armstrong, W. C. (1983), Recent advances from studies of the Trimpi effect, *Antarctic jour-*
513 *nal of the United States*, *18*(5), 281–283.

514 Barr, R., D. Llanwyn Jones, and C. J. Rodger (2000), ELF and VLF radio waves, *Journal of*
515 *Atmospheric and Solar-Terrestrial Physics*, *62*(17-18), 1689–1718, doi:10.1016/S1364-
516 6826(00)00121-8.

517 Budden, K. G. (1988), *The Propagation of Radio Waves: the theory of radio waves of low*
518 *power in the ionosphere and magnetosphere*, First paperback edition (with corrections),
519 Cambridge University Press, University Press, Cambridge, UK.

520 Chapman, F. W., and R. C. V. Macario (1956), Propagation of Audio-Frequency Radio
521 Waves to Great Distances, *Nature*, *177*(4516), 930–933, doi:10.1038/177930a0.

522 Chen, J.-t., U. S. Inan, and T. F. Bell (1996), VLF strip holographie imaging of
523 lightning-associated ionospheric disturbances, *Radio Science*, *31*(2), 335–348,
524 doi:10.1029/95RS02079.

525 Clilverd, M. A., R. Duthie, C. J. Rodger, R. L. Hardman and K. H. Yearby (2017), Long-term
526 climate change in the D-region, *Scientific Reports*, *7*(1), 16683, doi:10.1038/s41598-017-
527 16891-4.

528 Cotts, B. R. T., and U. S. Inan (2007), VLF observation of long ionospheric recovery events,
529 *Geophysical Research Letters*, *34*(14), L14,809, doi:10.1029/2007GL030094.

530 Cummer, S. A., U. S. Inan, and T. F. Bell (1998), Ionospheric D region remote sensing using
531 VLF radio atmospherics, *Radio Science*, *33*(6), 1781–1792, doi:10.1029/98RS02381.

532 Dowden, R. L., and C. D. D. Adams (1989), Modal effects on amplitude perturba-
533 tions on subionospheric signals (Trimpis) deduced from two-frequency measure-
534 ments, *Journal of Geophysical Research: Space Physics*, *94*(A2), 1515–1519,
535 doi:10.1029/JA094iA02p01515.

536 Dowden, R. L., J. B. Brundell, and C. J. Rodger (2002), VLF lightning location by time of
537 group arrival (TOGA) at multiple sites, *Journal of Atmospheric and Solar-Terrestrial*
538 *Physics*, *64*(7), 817–830, doi:10.1016/S1364-6826(02)00085-8.

539 Friedrich, M., and K. M. Torkar (2001), FIRI: A semiempirical model of the lower iono-
540 sphere, *Journal of Geophysical Research: Space Physics*, *106*(A10), 21,409–21,418,
541 doi:10.1029/2001JA900070.

542 Füllekrug, M. (2010), Wideband digital low-frequency radio receiver, *Measurement Science*
543 *and Technology*, *21*(1), 015,901, doi:10.1088/0957-0233/21/1/015901.

Füllekrug, M., A. Mezentsev, R. Watson, S. Gaffet, I. Astin, and A. Evans (2014), Array analysis of electromagnetic radiation from radio transmitters for submarine communication, *Geophysical Research Letters*, *41*(24), 9143–9149, doi:10.1002/2014GL062126.

Füllekrug, M., A. Mezentsev, R. Watson, S. Gaffet, I. Astin, N. Smith, and A. Evans (2015a), Map of low-frequency electromagnetic noise in the sky, *Geophysical Research Letters*, *42*(11), 4648–4653, doi:10.1002/2015GL064142.

Füllekrug, M., N. Smith, A. Mezentsev, R. Watson, I. Astin, S. Gaffet, A. Evans, and M. Rycroft (2015b), Multipath propagation of low-frequency radio waves inferred from high-resolution array analysis, *Radio Science*, *50*(11), 1141–1149, doi:10.1002/2015RS005781.

Füllekrug, M., Z. Liu, K. Koh, A. Mezentsev, S. Pedeboy, S. Soula, S. Enno, J. Sugier, and M. Rycroft (2016), Mapping lightning in the sky with a mini array, *Geophysical Research Letters*, *43*(19), 10448–10454, doi:10.1002/2016GL070737.

Gordillo-Vázquez, F. J., A. Luque, and C. Haldoupis (2016), Upper *D* region chemical kinetic modeling of LORE relaxation times: KINETIC MODEL OF LORE RELAXATION TIMES, *Journal of Geophysical Research: Space Physics*, *121*(4), 3525–3544, doi:10.1002/2015JA021408.

Haldoupis, C., M. Cohen, B. Cotts, E. Arnone, and U. Inan (2012), Long-lasting D-region ionospheric modifications, caused by intense lightning in association with elve and sprite pairs, *Geophysical Research Letters*, *39*(16), L16,801, doi:10.1029/2012GL052765.

Haldoupis, C., M. Cohen, E. Arnone, B. Cotts, and S. Dietrich (2013), The VLF fingerprint of elves: Step-like and long-recovery early VLF perturbations caused by powerful ±CG lightning EM pulses, *Journal of Geophysical Research: Space Physics*, *118*(8), 5392–5402, doi:10.1002/jgra.50489.

Hardman, S. F., C. J. Rodger, R. L. Dowden, and J. B. Brundell (1998), Measurements of the VLF scattering pattern of the structured plasma of red sprites, *IEEE Antennas and Propagation Magazine*, *40*(2), 29–38, doi:10.1109/74.683540.

Helliwell, R. A., J. P. Katsufrakis, and M. L. Trimpi (1973), Whistler-induced amplitude perturbation in VLF propagation, *Journal of Geophysical Research*, *78*(22), 4679–4688, doi:10.1029/JA078i022p04679.

Inan, U. S., D. C., Shafer, W. Y., Yip, and R. E., Orville (1988), Subionospheric VLF signatures of nighttime D region perturbations in the vicinity of lightning discharges, *Journal of Geophysical Research: Space Physics*, *93*(A10), 11455–11472,

577 doi:10.1029/JA093iA10p11455.

578 Inan, U. S., S. A. Cummer, and R. A. Marshall (2010), A survey of ELF and VLF research
579 on lightning-ionosphere interactions and causative discharges, *Journal of Geophysical*
580 *Research: Space Physics*, *115*(A6), A00E36, doi:10.1029/2009JA014775.

581 Johnson, M. P., U. S. Inan, S. J. Lev-Tov, and T. F. Bell (1999), Scattering pattern of
582 lightning-induced ionospheric disturbances associated with early/fast VLF events, *Geo-*
583 *physical Research Letters*, *26*(15), 2363–2366, doi:10.1029/1999GL900521.

584 Kotovsky, D. A., and R. C. Moore (2016), Photochemical response of the nighttime meso-
585 sphere to electric field heating—Recovery of electron density enhancements, *Geophysical*
586 *Research Letters*, *43*(3), 952–960, doi:10.1002/2015GL067014.

587 Kotovsky, D. A., R. C. Moore, Y. Zhu, M. D. Tran, V. A. Rakov, J. T. Pilkey, J. A. Caicedo,
588 B. Hare, D. M. Jordan, and M. A. Uman (2016), Initial breakdown and fast leaders in
589 lightning discharges producing long-lasting disturbances of the lower ionosphere, *Journal*
590 *of Geophysical Research: Space Physics*, *121*(6), 5794–5804, doi:10.1002/2015JA022266.

591 Lay, E. H., and X.-M. Shao (2011), High temporal and spatial-resolution detection of D-layer
592 fluctuations by using time-domain lightning waveforms, *Journal of Geophysical Research:*
593 *Space Physics*, *116*(A1), A01,317, doi:10.1029/2010JA016018.

594 Lay, E. H., X.-M. Shao, and A. R. Jacobson (2014), D region electron profiles observed with
595 substantial spatial and temporal change near thunderstorms, *Journal of Geophysical Re-*
596 *search: Space Physics*, *119*(6), 4916–4928, doi:10.1002/2013JA019430.

597 Marshall, R. A., U. S. Inan, and W. A. Lyons (2006), On the association of early/fast very
598 low frequency perturbations with sprites and rare examples of VLF backscatter, *Journal of*
599 *Geophysical Research: Atmospheres*, *111*(D19), D19,108, doi:10.1029/2006JD007219.

600 Mezentsev, A., and M. Füllekrug (2013), Mapping the radio sky with an interferometric net-
601 work of low-frequency radio receivers, *Journal of Geophysical Research: Atmospheres*,
602 *118*(15), 8390–8398, doi:10.1002/jgrd.50671.

603 Moore, R. C., C. P. Barrington-Leigh, U. S. Inan, and T. F. Bell (2003), Early/fast VLF
604 events produced by electron density changes associated with sprite halos, *Journal of Geo-*
605 *physical Research: Space Physics*, *108*(A10), doi:10.1029/2002JA009816.

606 NaitAmor, S., M. B. Cohen, B. R. T. Cotts, H. Ghalila, M. A. AlAbdoadaim, and K. Graf
607 (2013), Characteristics of long recovery early VLF events observed by the North African
608 AWESOME Network, *Journal of Geophysical Research: Space Physics*, *118*(8), 5215–
609 5222, doi:10.1002/jgra.50448.

NaitAmor, S., H. Ghalila, and M. B. Cohen (2017), TLEs and early VLF events: Simulating the important impact of transmitter-disturbance-receiver geometry, *Journal of Geophysical Research: Space Physics*, *122*(1), 792–801, doi:10.1002/2016JA022791.

Pasko, V. P., U. S. Inan, and T. F. Bell (1998), Ionospheric effects due to electrostatic thundercloud fields, *Journal of Atmospheric and Solar-Terrestrial Physics*, *60*(7–9), 863–870, doi:10.1016/S1364-6826(98)00022-4.

Rodger, C. J. (2003), Subionospheric VLF perturbations associated with lightning discharges, *Journal of Atmospheric and Solar-Terrestrial Physics*, *65*(5), 591–606, doi:10.1016/S1364-6826(02)00325-5.

Salem, M. A., N. Liu, and H. K. Rassoul (2016), Modification of the lower ionospheric conductivity by thunderstorm electrostatic fields, *Geophysical Research Letters*, *43*(1), 5–12, doi:10.1002/2015GL066933.

Salut, M. M., M. Abdullah, K. L. Graf, M. B. Cohen, B. R. T. Cotts, and S. Kumar (2012), Long recovery VLF perturbations associated with lightning discharges, *Journal of Geophysical Research: Space Physics*, *117*(A8), doi:10.1029/2012JA017567.

Silber, I., and C. Price (2017), On the Use of VLF Narrowband Measurements to Study the Lower Ionosphere and the Mesosphere–Lower Thermosphere, *Surveys in Geophysics*, *38*(2), 407–441, doi:10.1007/s10712-016-9396-9.

Thomson, N. R. (2010), Daytime tropical D region parameters from short path VLF phase and amplitude, *Journal of Geophysical Research: Space Physics*, *115*(A9), A09,313, doi:10.1029/2010JA015355.

Thomson, N. R., M. A. Clilverd, and C. J. Rodger (2011a), Daytime midlatitude D region parameters at solar minimum from short-path VLF phase and amplitude, *Journal of Geophysical Research: Space Physics*, *116*(A3), A03,310, doi:10.1029/2010JA016248.

Thomson, N. R., C. J. Rodger, and M. A. Clilverd (2011b), Daytime D region parameters from long-path VLF phase and amplitude, *Journal of Geophysical Research: Space Physics*, *116*(A11), A11,305, doi:10.1029/2011JA016910.

Thomson, N. R., M. A. Clilverd, and C. J. Rodger (2017), Midlatitude ionospheric D region: Height, sharpness, and solar zenith angle, *Journal of Geophysical Research: Space Physics*, *122*(8), 2017JA024,455, doi:10.1002/2017JA024455.

Wait, J. R., and K. P. Spies (1964), Characteristics of the earth-ionosphere waveguide for VLF radio waves, *NBS Technical Note 300*.

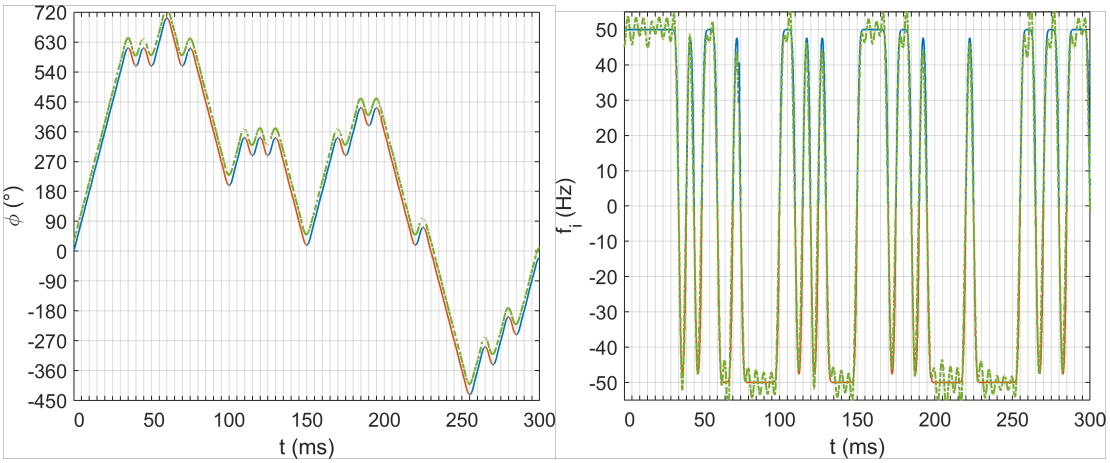

Figure 1. Received and estimated GMSK VLF transmission for a 300 ms period (15:00:05.485–15:00:05.785 UTC on 13 May 2011). (Left) Phase of the estimated transmission during positive (blue lines) and negative (red lines) symbols. The received transmission phase (dashed green line) is shown slightly offset for clarity. (Right) Instantaneous frequency of the estimated transmission containing the message encoded in the positive (blue lines) and negative (red lines) sideband frequencies. The message is estimated from the received transmission instantaneous frequency (dashed green line). The vertical grid lines separate each symbol of period 5 ms. The frequency separation between the sideband frequencies can be seen to be $f_s/2 = 100$ Hz. The maximum phase difference between the start of one symbol and the next is $\sim\pm 90°$ or $\pm\pi/2$.

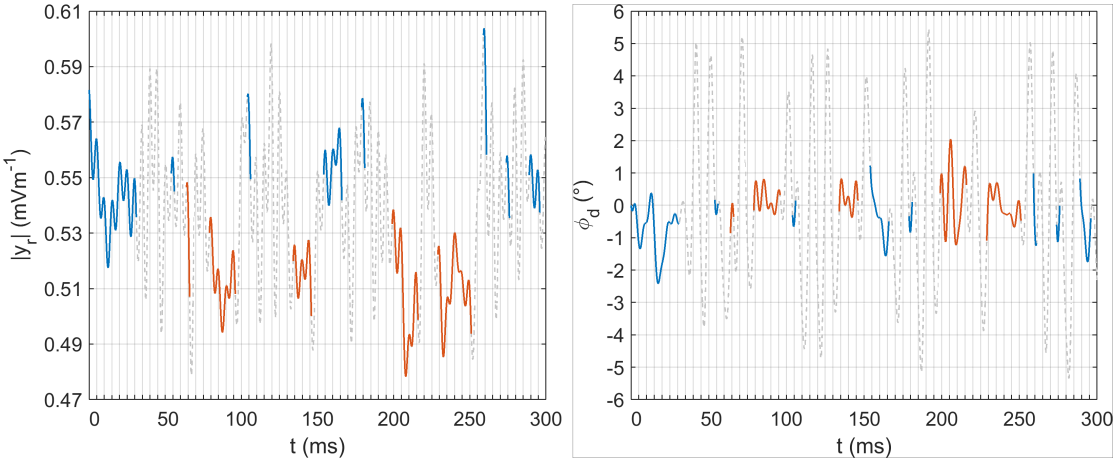

Figure 2. Micro-second time resolution signal of the DHO transmission received amplitude and phase disturbance during the same period as figure 1. (Left) Received amplitude and (Right) Phase disturbance during the positive (blue lines) and negative (red lines) symbols and the transitions between them (dashed grey lines) when the instantaneous frequency is not constant. The vertical grid lines separate each symbol of period 5 ms. The received amplitude and phase disturbance exhibit a frequency dependence (compare blue to red line) that is more pronounced in the amplitude than in the phase. They also exhibit fast temporal variabilities <5 ms.

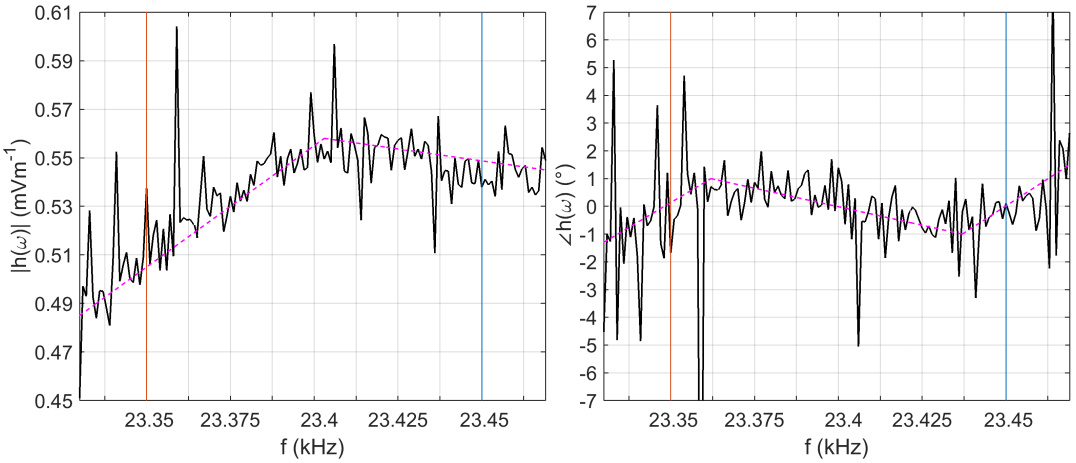

Figure 3. Frequency response of the DHO transmission attributed to the wave propagation in the Earth-ionosphere waveguide calculated for 15:00:03–15:00:09 UTC on 13 May 2011. (Left) Amplitude; (Right) Phase. The blue/red line indicates the nominal positive/negative sideband frequency respectively. The response exhibits a non-linear trend with frequency in amplitude and phase which can be both approximated by discontinuous linear sections (dashed magenta lines). Superimposed on these trends are irregular changes of the response which are attributed to random noise of unknown origin.

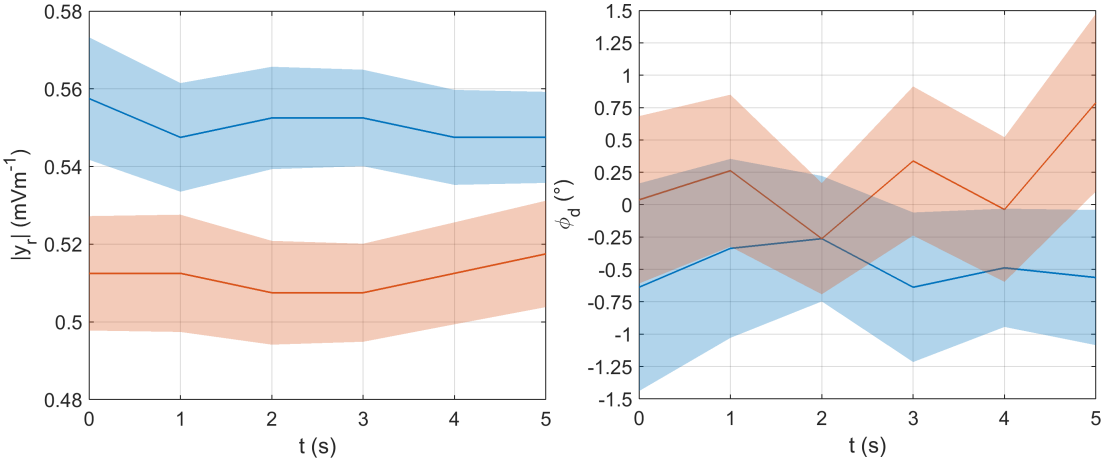

Figure 4. Statistical mode of received amplitude and phase disturbance distributions and their standard deviations over the same 6 s period of data as figure 3. (Left) Received amplitude; (Right) Phase disturbance. Each data point is computed from the samples in the following second; for example, the data point at t=0 s represents the samples from 15:00:03–15:00:04 UTC and the data point at t=5 s represents the samples from 15:00:08–15:00:09 UTC. The blue/red line denotes the positive/negative sideband frequency respectively. The 1σ standard deviation is shown as the shaded areas - this is a measure of the fast variabilities <5 ms (see section 4). A large proportion of the fast phase disturbance variability likely results from ionospheric variability over the propagation path or fast ionospheric processes. The statistical mode of the distributions changes independently of sideband frequency suggesting that the propagation frequency dependence varies over time.

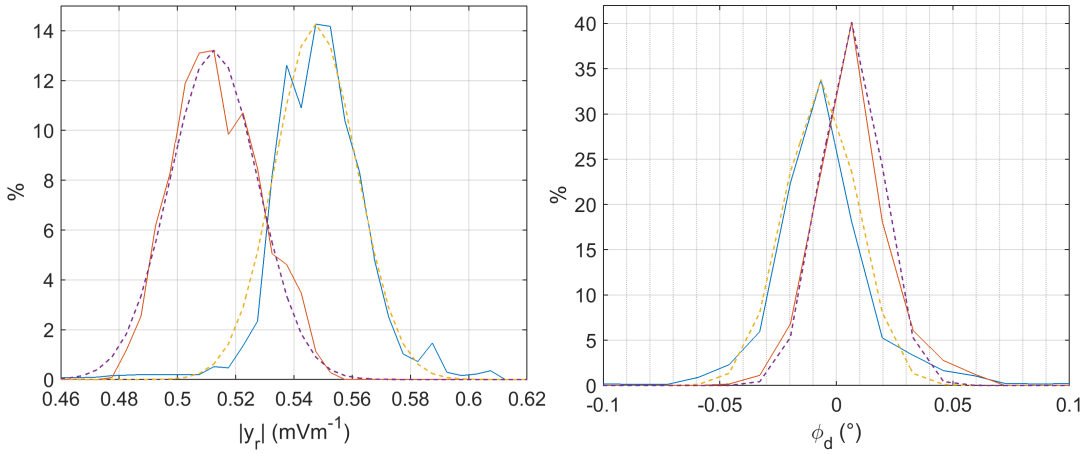

Figure 5. Distribution of the received amplitude and phase disturbance over a 1 s period of data from 15:00:04 UTC on 13 May 2011. (Left) Received amplitude; (Right) Phase disturbance. The blue/red line denotes the positive/negative sideband frequency respectively. The yellow and purple dashed lines are the fitted normal distribution shapes. All distributions are seen to agree roughly with a normal shape.

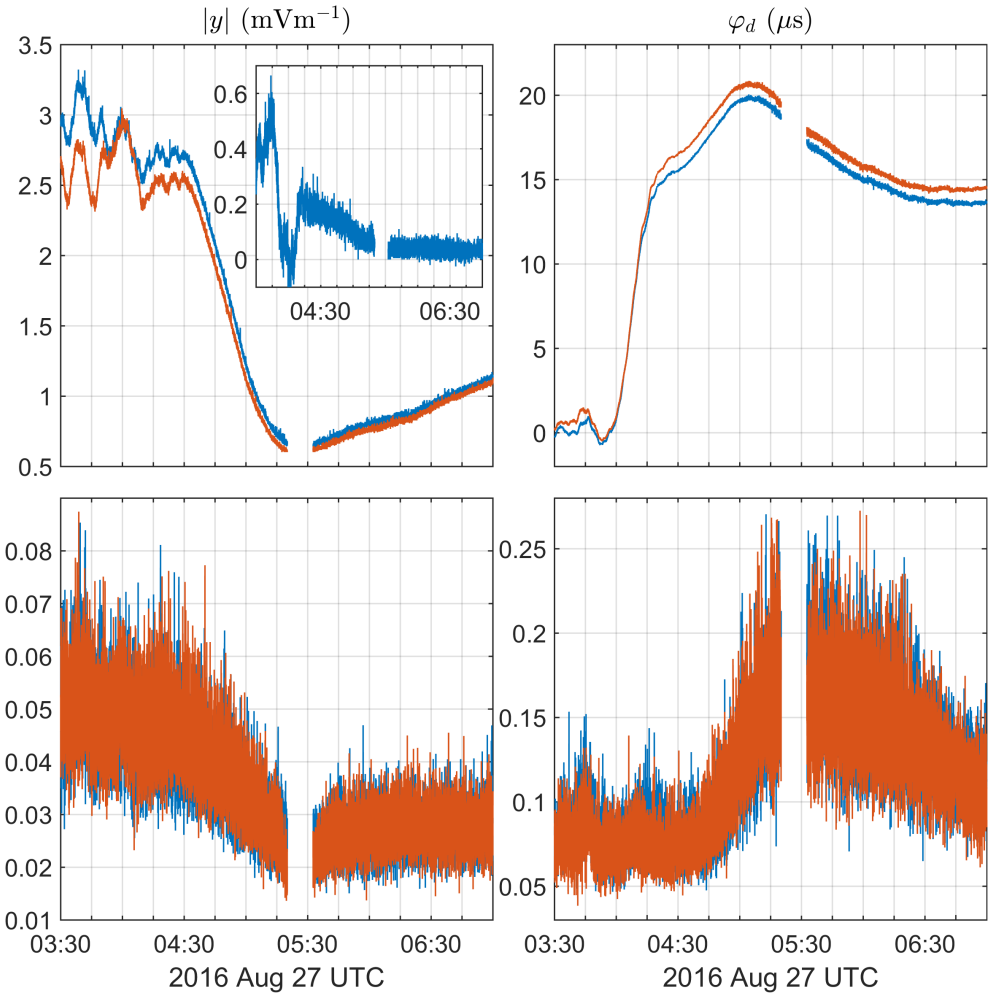

Figure 6. Statistical mode of received amplitude and phase disturbance distributions and their standard deviations for separate single receiver data from 27th August 2016 03:30–07:00 UTC. (Top left) Received amplitude, inset shows the difference between the received amplitudes of each sideband frequency; (Top right) Phase disturbance. (Bottom left) Standard deviation of received amplitude; (Bottom right) Standard deviation of phase disturbance. The blue/red line denotes the positive/negative sideband frequency received amplitude. Night time conditions on the propagation path are before 04:31 UTC (sunrise time at DHO transmitter site). Day time conditions are after 05:14 UTC (sunrise time at the receiver in Bath, UK). The ~10 minute gap around 05:30 UTC is due to the recording process being restarted (see section 5). There is a general correlation between the received amplitudes at each sideband but there is a varying difference between them. The differences between the sidebands are greater and vary more during night time conditions.

Chapter 4

Lower ionospheric conductivity modification during a convection surge

Commentary

The method developed in the previous paper was applied to a full day of data using multiple transmissions at different frequencies. Further, the transmitter sites for three of the transmissions covering the frequency range 19.53–60 kHz are near each other so that their propagation paths to the remote receiver are essentially the same. The aim of the experiment is to study the frequency dependence of ionospheric perturbations over the same path. A disturbance was observed in the day time associated with the initial stages of a thunderstorm that would grow and several hours later, produce further disturbances after sunset. As the mechanism for the day time disturbance is likely to be different from the night time disturbances, it is investigated separately in this paper.

During the observation, the small developing thunderstorm passed near ($\sim$50 km) the receiver which coincided with a sub-ionospheric radio disturbance observed on all the transmissions analysed. The disturbance exhibits a rise time 20–60 s and recovery of $>$200 s. The responses on all the transmissions had the same shape but the disturbance magnitude appears to decrease with transmission frequency for the transmissions on the same path. The rise and recovery times of the disturbance is not characteristic of previously reported thunderstorm and lightning related

ionospheric perturbations. However, data from a lightning location network and a nearby quasi-electrostatic sensor showed a pronounced increased in weak intra-cloud lightning just prior ($<$180 s) to the onset of the disturbance. It is proposed that this disturbance is caused by thunderstorm charging producing a change in the electric field - a phenomenon that has never previously been reported but could be commonplace, even during day time ionospheric conditions.

This declaration concerns the article entitled:									
Lower ionospheric conductivity modification during a convection surge									
Publication status (tick one)									
draft manuscript	✓	**Submitted**		**In review**		**Accepted**		**Published**	
Publication details (reference)	Kuang Liang Koh, Simon Ghilian, Zhongjian Liu, Alec Bennett and Martin Füllekrug. Lower ionospheric conductivity modification during a convection surge. 2018.								
Candidate's contribution to the paper (detailed, and also given as a percentage).	The candidate contributed to/ considerably contributed to/predominantly executed the… Formulation of ideas: 90% Discussion of ideas with M.F. and A.B. Design of methodology: 100% Experimental work: 80% Z.J. assisted with the collection of the radio data BTD-300 data provided by A.B. Lightning location data provided by Meteorage and compiled by S.G. Presentation of data in journal format: 90% S.G. provided the plots of the Meteorage data								
Statement from Candidate	This paper reports on original research I conducted during the period of my Higher Degree by Research candidature.								
Signed					**Date**				

Lower ionospheric conductivity modification during a convection surge

Kuang Koh, S. Ghilain, Z. Liu, A. Bennett, M. Füllekrug

key point #1: A day time ionospheric perturbation was observed with 20–60 s rise time and >200 s recovery

key point #2: The perturbation coincides with sudden convection intensification near the receiver

key point #3: Electrostatic field from thunderstorm electrification is proposed as the disturbance mechanism

Abstract

A day time perturbation in the lower ionosphere was observed using sub-ionospheric radio remote sensing. The disturbance event exhibited a 20-60 s rise time with a gradual recovery of >200 s. The intra-cloud lightning activity of a thunderstorm 50 km south of the radio receiver was seen to increase in coincidence with the event. Lightning has previously been observed to produce such disturbance events, however, with rise times <3 s; a characteristic closely linked to the physical mechanisms for lightning induced ionospheric perturbations. Therefore, the observed event is unlikely to be caused by lightning, yet appears associated with the thunderstorm.

It is proposed that this event is produced by a pronounced increase in convection strength that produced a significant change in the electrification of the thunderstorm. This change in electrification can be observed in the increase in the intra-cloud lightning activity of the thunderstorm.

1 Introduction

The electrical activity of thunderstorms has been observed to influence the conductivity of the ionosphere via a number of different mechanisms [Rodger, 2003, Neubert et al., 2008, Inan et al., 2010, Shao et al., 2013]. Lightning discharges enable the most direct mechanisms as they produce strong ElectroMagnetic Pulses (EMP) and Quasi-Electrostatic (QE) fields above the thunderstorm. These can produce heating and ionisation effects in the lower ionosphere thereby altering the conductivity profile [Inan et al., 1991, Taranenko et al., 1993, Pasko et al., 1995]. In addition to conductivity changes, luminousity can also be produced given sufficiently strong fields from intense discharges. A variety of Transient Luminous Events (TLEs) are possible that are associated these mechanisms; EMP produces elves and QE produces sprites and sprite halos [Pasko et al., 2012, Liu et al., 2015]. Less directly, whistler mode waves launched by lightning discharges can interact with radiation belt electrons causing them to precipitate into the lower ionosphere [Voss et al., 1984, Helliwell et al., 1973, Inan et al., 2007, Gemelos et al., 2009]. It is also possible for the electrostatic field of the thunderstorm itself to influence lower ionospheric conductivity by heating [Inan et al., 1996, Pasko et al., 1998].

These conductivity changes occur at mesospheric D region altitudes ($\sim$50-100 km) which make it difficult to study via direct or satellite measurements. The sensitivity of sub-ionospheric radio propagation to ionospheric changes along the propagation path thus makes it a popular technique for D region observation. Radio receivers are used to monitor either man-made transmissions or lightning electromagnetic radiation from afar and deviations on the received signal from a background state are interpreted as conductivity changes in the ionosphere [e.g. Cummer et al., 1998, Shao et al., 2013, Thomson et al., 2017, Clilverd et al., 2017]. Lightning related ionospheric perturbations have been observed using sub-ionospheric radio remote sensing and were referred to as 'Trimpi' disturbances in the initial stages. Subsequently, many categorisations of Trimpis were proposed based on the features of the disturbance and the physical mechanism implied. There are two broad categories, Lightning-induced Electron Precipitation (LEP) and Early events. LEP events exhibit onset delay times up to $\sim$1 s (dependent on the geomagnetic latitude) associated with the propagation time of the whistler mode waves and electron precipitation. In contrast, the 'Early' moniker refers to

the <100 ms delay time from the causative lightning to the disturbance onset for Early events which precludes the LEP mechanism for Early disturbances. Additionally, the rise times of Early events are also usually faster (<20 ms) than LEP events. The lack of delay and fast rise time suggests that the disturbances are a result of the direct mechanisms of lightning EMP and QE fields thus encouraging attempts at further categorisation based on affliations with TLEs, for example 'VLF sprites' and 'VLF elves' [Dowden et al., 1996].

It is possible to infer the exact mechanism of Early events by looking for coincidence with either elves, sprites or sprite halos [e.g. Mika and Haldoupis, 2008]. However, Early events can occur without any TLEs [e.g. Marshall et al., 2006] or with both elves and sprites [e.g. Takahashi et al., 2003]. It is plausible that weaker EMP or QE fields can produce Early events with no TLEs - Early events associated with weak discharges <50 kA have been observed [e.g. Inan et al., 1995]. Similarly, lightning discharges produce EMP, QE fields and electrostatic field changes so that some combination of mechanisms may have an effect at the same time. Early events with exceptionally long recovery durations have been observed and named LOng Recovery Early (LORE) events [Cotts and Inan, 2007, Haldoupis et al., 2012]. These events were initially linked to a combination of elves and sprite mechanisms, however, no satisfactory mechanism has yet been proposed. Effects of sucessive lightning discharges can also accumulate to produce a disturbance. Early events with relatively slow (up to 3 s) rise times have been observed and the slow rise times attributed to the build up time of successive lightning EMP conductivity modifications [Haldoupis et al., 2006, Marshall and Inan, 2010]. These are referred to as Early/slow events.

This contribution presents a novel observation of a day time sub-ionospheric radio disturbance related to a thunderstorm that is difficult to explain with either the EMP or QE mechanism. A variation on the electrostatic thunderstorm field mechanism driven by convection rather than lightning is proposed.

2 Sub-ionospheric radio observations

Vertical electric field measurements were taken in Bath, UK on the 27th August 2016 with a single wideband (4 Hz–400 kHz) receiver [Füllekrug, 2010]. The receiver samples at 1 MHz frequency with an amplitude resolution of 35 μV and

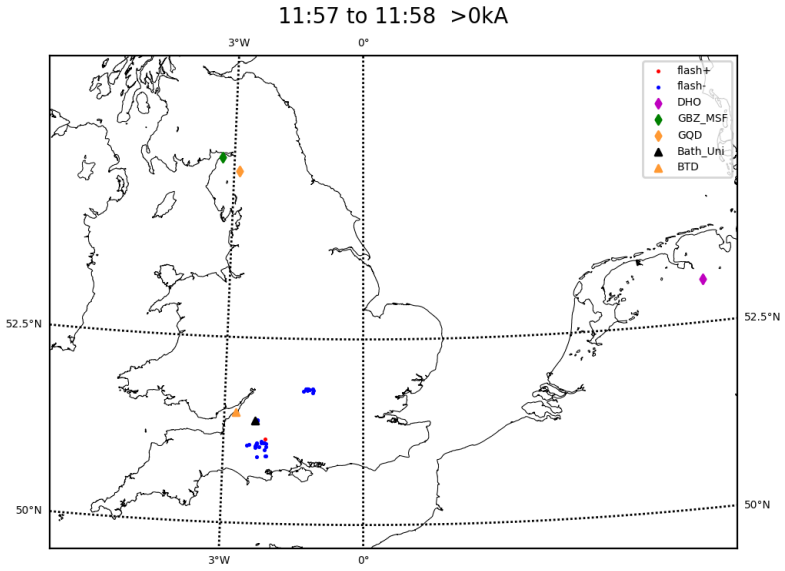

Fig. 1: Map of transmitters, thunderstorm and instruments. The locations of the wideband radio receiver in Bath, UK and the BTD-300 in Portishead are marked with black and yellow triangles respectively. The transmitter sites are marked by different coloured diamonds, GBZ/MSF in green, GQD in yellow and DHO in purple. Lightning locations are shown as dots with blue and red distinguishing positive from negative polarity lightning.

timing accuracy of 20 ns. Four separate radio transmissions were simultaneously monitored using the same receiver. These transmissions are referred to with call-signs GBZ, MSF, GQD and DHO . The GBZ broadcast is transmitted from the same station as the MSF timing signal in Anthorn, UK (54.912°N, -3.279°E) which is ∼398 km from Bath on a north-south (351.2°) great circle path. GQD is transmitted from nearby Skelton, UK (54.732°N, -2.883°E, only ∼32.5 km away from the GBZ radio station), ∼375 km from Bath on almost the same path (354.5°) as for GBZ and MSF. DHO is transmitted from Rhauderfehn, Germany (53.079°N, 7.615°E), ∼704.5 km from the receiver in Bath on an east-west (70.5°) great circle path. These locations are shown in figure 1. These transmissions operate at different frequencies with narrow bandwidths; GBZ at 19.58 kHz, MSF at 60 kHz, GQD at 22.1 kHz and DHO at 23.4 kHz.

3 Measuring lower ionospheric perturbation using sub-ionospheric radio transmissions

The modulation of information on each transmission has to be removed to observe perturbations in the lower ionosphere. The methodology used is the same as that used by [Koh et al., 2018]. A general description of the method is as follows. The real-valued time series data is first converted to a complex baseband time series using the Hilbert transform. This is done by frequency shifting and filtering the data to remove negative frequencies and isolate the frequencies of interest [Liu et al., 2016, section 3.1]. This time series can be represented by $y_c(t) = A(t)e^{i\varphi(t)}$ where $A(t)$ is the amplitude and $\varphi(t)$ is the phase of the signal. These can be calculated for each sample in $y_c(t)$ by taking the modulus $A(t) = |y_c(t)|$ and argument $\varphi(t) = \arctan(\frac{\Im[y_c(t)]}{\Re[y_c(t)]})$. By taking the phase differential, the instantaneous frequency can also be calculated $\omega_i(t) = \frac{\mathrm{d}}{\mathrm{d}t}\varphi(t)$. Secondly, the received complex time series is demodulated to obtain the message symbol sequence. A simulated transmission is produced using this symbol sequence and the deviation of the received transmission from the simulated transmission is taken as the ionospheric signal amplitude $|y_i|$ and phase φ_i.

The modulation of GQD, GBZ and DHO are based on Minimum Shift Keying (MSK). This modulation scheme can be considered as a special case of binary Frequency Shift Keying, i.e., the transmission switches between two sideband frequencies to convey information. For MSK transmissions, the sidebands are spaced symmetrically around the centre frequency. This enables demodulation of the MSK signal using the polarity of the instantaneous frequency - see [Koh et al., 2018, section 3] for an extended description.

Since the ionospheric signal is based upon the simulated transmission, the assumption is that the transmission is stable and follows its modulation scheme perfectly. This is not always valid; instances of phase jumps and frequency offset have been reported [Gross et al., 2018, Thomson et al., 2017]. A phase ramp in the disturbance signal of DHO is observed in this data (not shown) that is symptomatic of it being transmitted at a frequency offset from its published centre frequency. The phase ramp disappears when the centre frequency value is offset by 61.73 μHz, which is the same offset determined by [Thomson et al., 2017] for the DHO transmission in 2015. This offset centre frequency is used throughout

the analysis here. All other phase jumps and ramps in the data are attributed to ionospheric effects as described in the following section 4.

The MSF transmission is a timing signal service provided by the National Physical Laboratory (NPL, the UK national measurement institute). The timing information is transmitted using On-Off Modulation, otherwise the signal is a continuous sinusoid at the carrier frequency of 60 kHz. The frequency stability of the transmission is published as being within 2 parts in 10^{12} of the carrier frequency so it can be used as a frequency standard. It can thus be described as $y_{OOM} = A(t)e^{i\varphi}e^{i\omega_c t}$. After shifting to baseband, the phase of MSF should be constant, $y_{OOM}e^{-i\omega_c t} = A(t)e^{i\varphi}$. Figure 2 shows a short example of the received MSF transmission amplitude (top) and phase (bottom) during a period of stable, low noise conditions (27th August 2016, 10:29:00 UTC to10:29:02.6 UTC). The amplitude modulation is seen in the first half of each second and the phase of MSF is effectively noise during the 'off' symbols (denoted using dashed lines). The 'off' samples are removed from the analysis. The received 'on' amplitude over this short period appears to increase from an 'off' to 'on' symbol transition to the following 'on' to 'off' transition in a non-deterministic way. This is most obvious when the 'on' period is smallest at the start second of every minute when MSF is 'off' for 0.5 s, then 'on' for 0.5 s (see arrows in top panel). This effect is likely to originate from the transmitter and cannot be said to be an ionospheric signal. In the longer term, it is assumed here that MSF transmitted power is constant and the received amplitude during MSF 'on' symbols over periods >1 s is taken as the ionospheric signal amplitude $|y_i|$. The received phase of MSF is shown to be approximately constant (after removing 'off' samples) as specified and no corrections were reported in the MSF bulletins published by NPL (www.npl.co.uk/science-technology/time-frequency/products-and-services/time/msf-bulletins) over the period of all data presented in this work.

The ionospheric signal can be calculated for each sample of the recording so that over 1 s, a good estimate of the disturbance signal distribution can be obtained. In each 1 s distribution, samples that are considered to be not representative of the ionospheric signal are removed. For example, when the transmission amplitude is low, the received signal is dominated by unknown sources. Further, lightning electromagnetic radiation can swamp the transmission signal - this is the most common source of wideband impulsive noise in the radio data. Light-

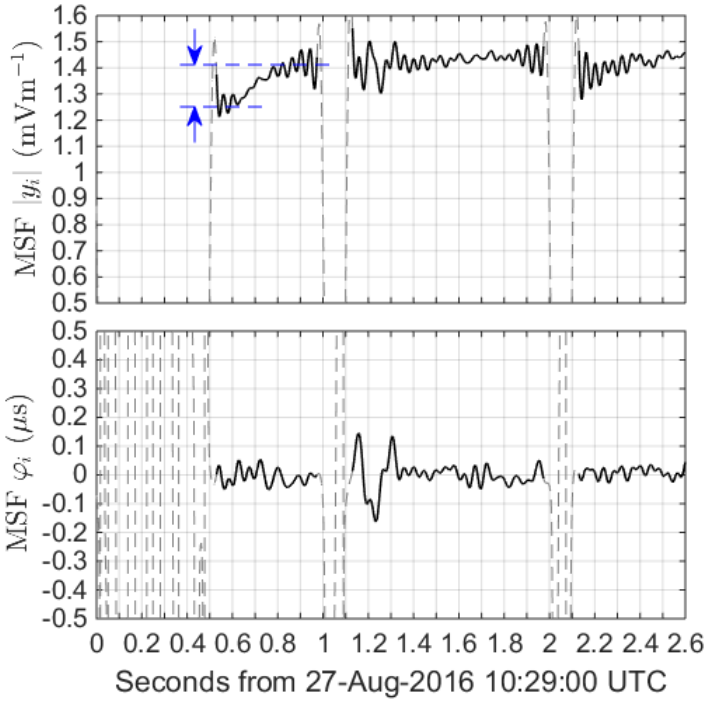

Fig. 2: Example of received MSF transmission amplitude (left) and phase (right) on 27th August 2016, 10:29:00–02.6 UTC. Solid lines show the signal when the 'on' symbol is transmitted and dashed lines show the signal when the 'off' symbol is transmitted. The blue arrows illustrate the difference in amplitude after a transition between the symbols. The amplitude modulation is seen in the first half of each second and the phase of MSF is effectively noise during the 'off' symbols. The 'off' samples are removed from the analysis.

ning interference is identified from the 5-15 kHz frequency band of the wideband radio data. Narrow band interference like other transmissions or low frequency powerline harmonics are already effectively removed by the filtering applied.

The frequency dependent propagation of the sidebands [Koh et al., 2018] is considered by distinguishing between samples when different sidebands are transmitted on each MSK transmission. Thus, for each MSK transmission, there is a distribution per second for each sideband. The samples that occur during the transitions between the sidebands are removed from the distributions as there is a rate of change component in the instantaneous frequency. Wideband random noise and signals from fast ($\ll$1 s) variations in the ionosphere [Füllekrug et al., 2015] are reduced by taking the statistical mode of each 1 s distribution. The data from seconds when the number of valid samples in the distribution is $< 10^5$ are considered unreliable in this study.

4 Lower ionospheric observation

The ionospheric signal log amplitude $\log_{10}|y_i|$ and phase φ_i for the four transmissions are shown in figure 3 (left and right panels respectively) over 24 hours from 27th August 2016 00:28 UTC to 28th August 2016 00:28 UTC which illustrates their response to the diurnal cycle. The MSK modulated GBZ, GQD and DHO transmissions have 2 sideband frequencies each; the higher frequency sideband is shown in blue and the lower frequency sideband is shown in red. GBZ and DHO both operate with a 100 Hz separation between their sideband frequencies while GQD uses a 50 Hz separation. The ionospheric signal shown for each transmission thus represent the frequencies shown in table 1. D region conductivity is dominated by the effect of solar radiation during day time conditions so that conductivity is higher and the D region extends to lower altitudes. At night, the absence of solar radiation means conductivity is reduced and D region altitude is higher. The solar influence during day time results in stable ionospheric conditions such that there is little variation in the signal. The slow change in the ionospheric signal throughout the day is likely to be due to a changing solar zenith angle. Under night time conditions, the ionospheric signal exhibits larger and faster variation. There is a sharp inflexion in the signals of all transmissions during the transitions that is attributable to the crossing of the terminator.

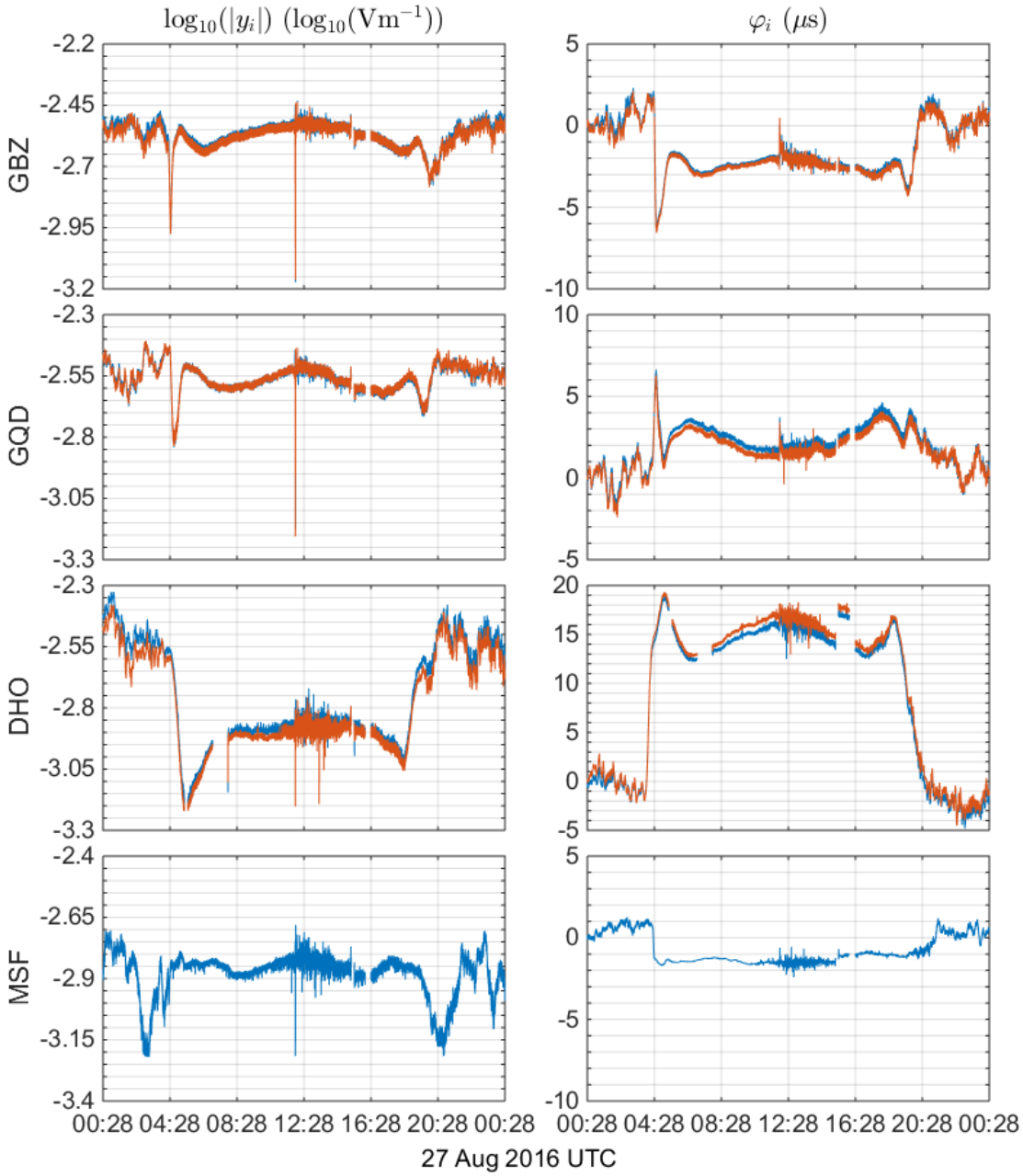

Fig. 3: Observation of the ionospheric signal amplitude $|y_i|$ (left) and phase φ_i (right) over 24 hours from 27th August 2016 00:28 UTC to 28th August 2016 00:28 UTC. The ionospheric signals from transmissions GBZ, GQD, DHO, MSF are shown (top to bottom). The higher frequency sideband of each MSK modulated signal is shown in blue. The lower frequency sideband is shown in red. The diurnal responses of GBZ, GQD and MSF ionospheric signals are similar whilst DHO is more sensitive. The signals vary more during night time than day time conditions. Under day time conditions in the morning, no sudden changes are seen until the event at 11:57 UTC.

Transmission	H	L
GBZ	19630 Hz	19530 Hz
GQD	22125 Hz	22075 Hz
DHO	23450 Hz+61.73 μHz	23350 Hz+61.73 μHz
MSF	60000 Hz	-

Tab. 1: Frequencies of the monitored transmissions, the column headed 'H' reports the higher frequency sideband of MSK transmissions and the column headed 'L' reports the lower frequency sideband. The MSF transmission has only one frequency.

GBZ, GQD and MSF share a similar North-South oriented propagation path and hence their ionospheric signals are sensitive to the same propagation path. The amplitude and phase are relative to the transmitted power and start phase of each transmission respectively and so cannot be compared directly between the transmissions. However, it is possible to compare relative changes. Between day and night conditions, the amplitude gain ($<$1.26) and modulus phase change ($\sim$2 μs) are similar for these transmissions. Interestingly, MSF φ_i is more stable at night than GBZ and GQD. The DHO transmission is more sensitive with an amplitude gain of ~ 2 and phase change of $\sim -15\,\mu$s.

The ionospheric amplitude and phase signals of the four observed transmissions were stable in the day light hours prior to 11:57 UTC. The half hour period from 11:55–12:25 UTC is shown in detail in figure 4. The signal is stable until $\sim$11:57 UTC when a clear disturbance occurs on all frequencies. The general features of the disturbance appear to be similar across frequencies. The amplitude is seen to fluctuate at the start of the disturbance for $\sim$120 s (11:57–11:59 UTC, shaded in green in each panel of figure 4). It then starts to increase before stabilising above the pre-disturbance amplitude. This post-disturbance amplitude is about 1.0471 times the pre-disturbance amplitude at all frequencies. The phase exhibits a 20–60 s duration increase followed by a slowing decay. The decay rate is steady with small deviations (most obvious in the φ_i of GBZ and GQD in figure 4) in the first 180 s past the peak (3–6 minutes in the x axis). Afterwards, the decay stops before increasing slowly until 12:05:00 UTC (10 minutes in the x axis) when φ_i starts decreasing again. The maximum phase increase varies across frequencies from 1.7 μs (GBZ frequencies) to 0.3 μs (MSF). Additionally, the MSF ionospheric signal phase fluctuates below the pre-disturbance level before recov-

ering by 12:25 UTC. At all other frequencies, the ionospheric signal phase stays above the pre-disturbance level.

The exact features of the amplitude disturbance at the onset is hard to determine due to two factors: (1) the start of the disturbance coincides with an increase in interference that can be seen in the broadband vertical electric field signal from the radio receiver (not shown) that is likely to originate from nearby lightning discharges (described in section 5); (2) the amplitude drops below a threshold level when the transmission is determined as not transmitting - this is shown as a gap in the data. A second large gap in the data (12:02:36 to 12:04:43 UTC) followed by smaller gaps after are due to interference resembling a pulse train that can be seen in the broadband radio data (not shown). This interference is present ∼12:02:32 to 12:05:12 UTC and is of unknown origin.

5 Convection and lightning activity

All transmission propagation paths were in full daylight conditions during the disturbance, including the few hours before and after so that lower ionospheric conditions are stable. Around 1100 UTC, convection started on the southern coast of the UK (over Weymouth, Dorset). The thunderstorm developed and travelled northward so that by midday, the thunderstorm core was ∼50 km south of Bath, UK. Lightning location and peak current data was available from Météorage. Figure 1 indicates the reported lightning around Bath at 11:57–58 UTC (start time of the ionospheric perturbation signal). The concentration of lightning just south of Bath indicates the location of the thunderstorm. Figure 5 shows the time evolution of the lightning activity reported for the thunderstorm near Bath, UK from 11:45–12:15 UTC. There is little CG activity except for 1 significant CG after the event onset (11:59 UTC). The IC activity appears to increase from 11:57 UTC, peaking at 11:59 UTC before decreasing briefly back to the pre disturbance level. Subsequent IC activity is seen to grow almost constantly.

Measurements of the thunderstorm electrical activity were available from a quasi-electrostatic field sensor located at Portishead near Bristol (51.486°, -2.757°) called the BTD-300. It measures the vertical electric field from 1–50 Hz on three co-located antennas so that it is able to distinguish electric field changes due to nearby (<100 km) thunderstorm electrical activity from changes caused by local

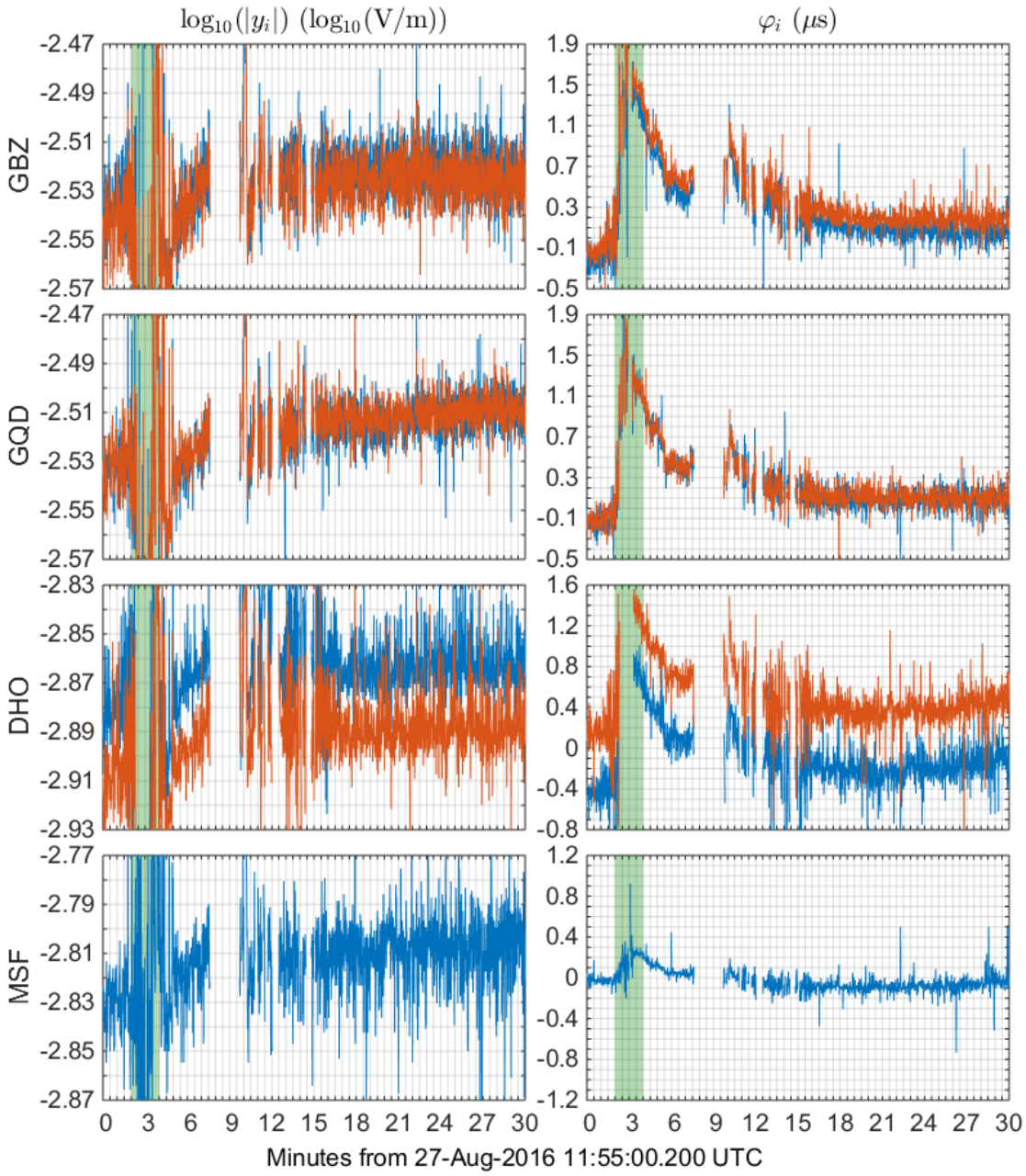

Fig. 4: Disturbance on the ionospheric signal amplitude (left) and phase (right) during the half hour from 27th August 2016, 11:55–12:25 UTC in the same format as for figure 3. The 120 s from the start of the disturbance at 11:57 UTC (2 minutes on the x axis) is shaded in green. The gaps in the data are when amplitude is low (just after the disturbance onset) or due to excessive interference (12:02:32–12:05:12 UTC). See section 4 for a detailed description.

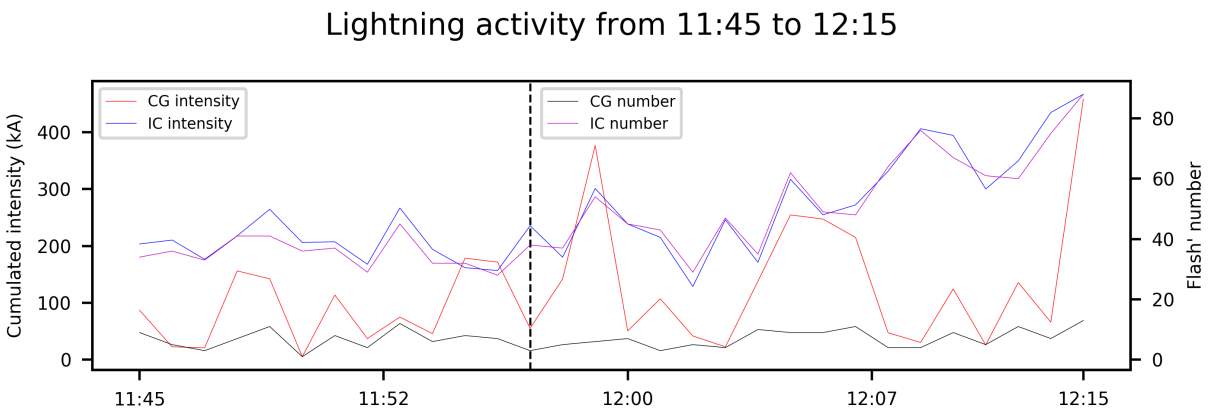

Fig. 5: Lightning activity around Bath, UK during the half hour from 27th August 2016, 11:45-12:15 UTC in one minute time resolution. The CG lightning number and cumulated intensity is shown in black and red lines. IC lightning is shown in purple and blue. IC lightning activity is seen to increase from the event onset time marked by the vertical dashed black line. There is a large CG after the event onset.

sources such as corona discharge, space charge variability and precipitation [Bennett, 2013]. The design was conceived to provide unambiguous reports of nearby lightning occurence with low false alarm rates for early warning purposes. Additionally, lightning range estimation is possible using the integrated voltage of a flash. The estimated lightning range during this time roughly agreed with the Météorage reported locations. Figure 6 shows the calibrated equivalent induced current on the main antenna of the BTD-300. During the half hour before the event, infrequent electrical activity was detected from the storm. However, $<$180 s before the beginning of the ionospheric perturbation, the received signal amplitudes on the BTD-300 suggests a pronounced increase in weak intra-cloud activity which is sometimes associated with a rapid increase in storm severity.

6 Discussion

Key features of the disturbance presented can be summarised as:

(1) No significant CG activity at the start or during the onset

(2) Rise time is 20–60 s

(3) Recovery time is $>$200 s

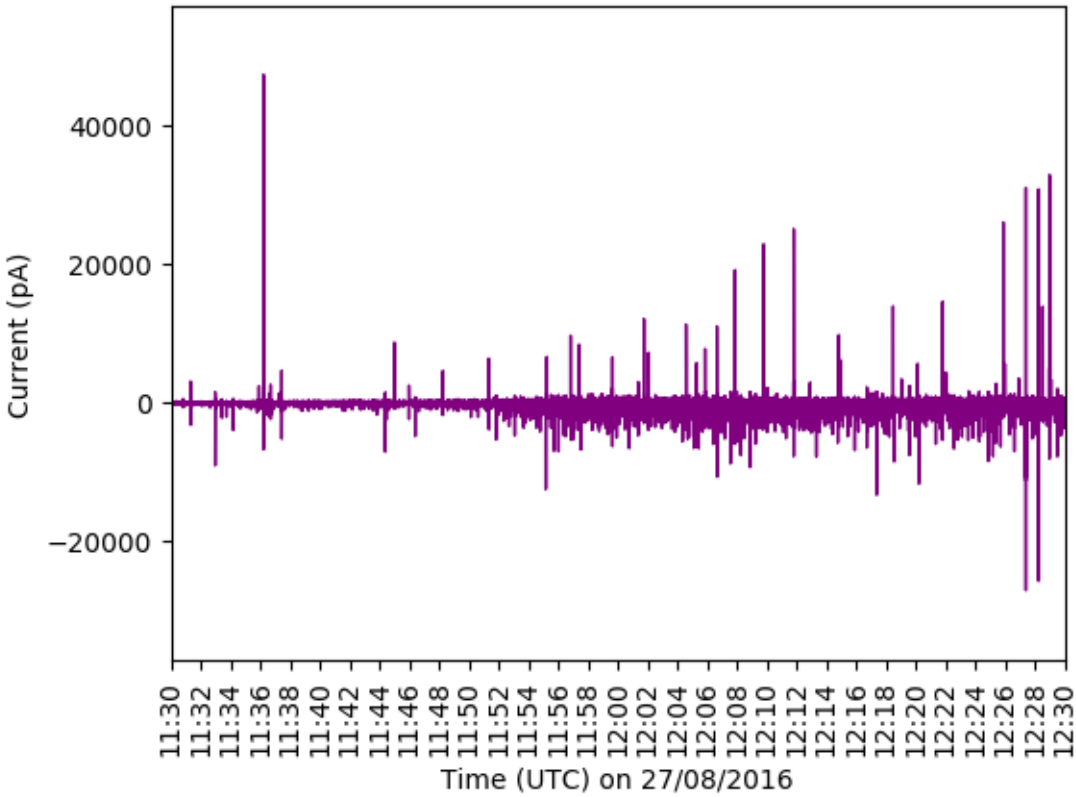

Fig. 6: Calibrated equivalent induced current on the main antenna of the BTD-300 during the hour from 27th August 2016, 11:30-12:30 UTC. The BTD-300 is designed to measure the vertical electric field from 1–50 Hz on three co-located antennas. The signal is seen to increase from around 11:54 UTC.

(4) Occurence during day time conditions

There are several possible causes for D region ionospheric perturbations such as that presented in this work. Events of solar origins such as solar flares or coronal mass ejections can produce D region modifications during the day. The geographical extent of such events cover the entire sun lit portion of the Earth. It is also possible for energetic particles from other extra terrestrial origins to penetrate to D region heights. However, observations of extra terrestrial radiation and particle fluxes were reported to be low. The planetary index of geomagnetic disturbances $K_p \leq 1$ (obtained from ftp.gfz-potsdam.de/pub/home/obs/kp-ap/) on 27th August 2016 and is $\leq 3+$ on the preceding 2 days. X-ray flux measured by geosynchronous satellites (GOES-13 and 15, obtained from satdat.ngdc.noaa.gov/sem/goes/data/plots/) is $<10^{-7}\,\mathrm{Wm}^2$ on 27th August 2016. Causes such as heating by high power radio waves and nuclear explosions are considered improbable.

Factors such as a glitches in either the receiver or transmitters are similarly improbable. The receiver is seen to operate throughout the rest of the day and temporary faults such as a loss of GPS lock or dropped measurement samples would produce a frequency independent delay. Transmission faults would be independent of each other. Therefore, the most likely source of the perturbation is the small thunderstorm described in section 5. Thunderstorm related D region perturbations are typically attributed to lightning activity (LEP and Early events). However, a few features of the observed disturbance stand out as being atypical of lightning-ionospheric perturbations.

One of the characteristics of LEP and Early events is a fast rise time which is believed to be a effect of the impulsive energy of lightning discharges. Of these disturbances, the slowest rise times are associated with less direct mechanisms such as for LEP or Early/Slow events. However, even these indirect mechanisms produce disturbances with rise times $<3\,\mathrm{s}$, much faster than the $>20\,\mathrm{s}$ rise time of the disturbance (taking into consideration uncertainty due to the fluctuation in the amplitude and gaps in the data).

Another atypical feature is the occurence of the observed disturbance in the day. The higher D region conductivity in the day time is not conducive for the theoretical mechanisms of lightning-ionospheric perturbation. Observations of such events are predominantly in the night time in agreement with theory, although there is

a rare report of day time occurrences [Kumar et al., 2008, figures 6 and 7]. The report consists of events with fast <2 s rise times and gradual recoveries of 5–20 s duration. The recovery times of disturbances are generally thought to be driven by the relaxation of the ionosphere to heating and ionisation which are faster at lower altitudes. Lower ionospheric conductivity has a profile that increases with altitude. In the day time, increased ionisation from solar radiation increases the overall D region conductivity so that VLF reflection height in the day is lower than at night. The higher D region conductivity restricts the penetration of strong electric fields to higher altitudes. Therefore, day time disturbances should have shorter durations than night time disturbances and the rare observations appear consistent with this assessment. In contrast, the observed disturbance appears to have a recovery duration of >200 s which is longer than common night time Early events. Such long duration disturbances are classed as LORE events as they do not fit the theoretical mechanisms for the recovery times of Early events.

Further, at the onset of the observed disturbance, there is no single high peak current discharge (>50 kA) reported or in the BTD-300 measurements. Charge moment changes of the discharges are also low. The key parameters determining likelihood and magnitude of disturbance by lightning are peak current for EMP and charge moment change. Therefore, the probability of lightning EMP or QE field mechanism being the cause of the disturbance is remote. Wideband interference is not expected to produce such a coherent signal and a fault in the radio receiver is not possible - the recording after the event resembles an undisturbed day time signal. Recent modelling studies [Salem et al., 2016] showed that thunderstorm electrostatic fields can produce significant conductivity changes in the night time D region by a combination of electron heating [Inan et al., 1996, Pasko et al., 1998] and modification of chemical kinetics. It is possible that day time D region conductivity can also be influenced by thunderstorm electrostatic fields.

The change in lightning activity before the observed disturbance onset implies a change in the thunderstorm electrification which could be an increase in charge or a reconfiguration of charge, or both, that is driven by convection. This should impart a change in the thunderstorm electrostatic field that is seen in the ionosphere above and near the electrification change. Surface measurements near thunderstorms [Jameson et al., 1996, Stolzenburg et al., 2015] show increases in the electrostatic field during the initial electrification of thunderstorms lasting

20–600 s. Using a statistical approach, [Zoghzoghy et al., 2013] showed thunderstorms can re-charge following a lightning flash in <30 s. Thus it is probable that the rise time of the observed disturbance is related to a period of intense 20–60 s electrification change in the thundercloud producing a corresponding conductivity change in the ionosphere above. The IC lightning activity of the thunderstorm is also seen to increase roughly corresponding with the event onset as evidenced by reports from Météorage (figure 5) and measurements from the BTD-300 (figure 6). The observed recovery of the disturbance signal could be an effect of the thunderstorm electrostatic field relaxing back to its original levels as convection abates. The staged decay rate can thus be explained as fluctuations in the convection strength as it decreases. Additionally, the disturbance does not recover to previous levels indicating that the general thunderstorm electrification remains changed from before the observed disturbance. Interestingly, the IC lightning activity shows a continuous growth after the disturbance peak.

Since the transmissions GBZ, GQD and MSF share roughly the same propagation path, the disturbance seen on their frequencies can be compared. In general, the observed disturbance has the same characteristics on all frequencies except that GBZ frequencies appear most sensitive to the ionospheric perturbation, followed by GQD then MSF. Sub-ionospheric radio propagation is frequency dependent and the reflection coefficients of modal propagation theory are a function of the electron density and collision frequencies [Wait and Spies, 1964, Budden, 1988, Barr et al., 2000, Marshall and Inan, 2010] which vary with altitude. The increasing conductivity of the ionosphere with height means that higher frequencies penetrate to higher altitudes. The larger response of GBZ and GQD frequencies compared to MSF frequencies suggests that the perturbation is larger at lower altitudes as GBZ and GQD transmits at lower ∼20 kHz compared to the 60 kHz MSF frequency . For example, the maximum phase change of GBZ and GQD frequencies is ∼1.7 μs and ∼1.5 μs respectively compared to 0.3 μs for MSF. The difference between GBZ and GQD is much smaller than that with MSF is because the frequency separation to MSF is much larger. Further, MSF phase is the only signal to return to pre-disturbance levels which is consistent with a perturbation caused by the thunderstorm electrostatic field as the field strength decreases with increasing altitude.

Thus, it is proposed that the electrostatic field of a thunderstorm can appreciably

modify the conductivity of the D region ionosphere so that the perturbation can be observed with sub-ionospheric radio even in the day time. This finding may be applicable in investigations of thunderstorm electrification to infer electrostatic fields above thunderstorms. It is also possible that the recoveries of some LORE events can be attributed to the thunderstorm electrostatic field. Modelling of the electrostatic mechanism using day time ionospheric conductivity profiles are needed to understand the specifics of the mechanism. The detailed measurement with multiple frequencies mean it may be possible to determine the altitude dependence of the perturbation.

7 Acknowledgements

The work of K.K. is sponsored by the Engineering and Physical Sciences Research Council 418 (EPSRC) under DTA contract EB-EE1151. The work of S.G. is sponsored by the SAINT project of the European Commission (H2020-MSCA-ITN-2016, 722337). The work of M.F. is sponsored by the Natural Environment Research Council (NERC) under grants NE/L012669/1 and NE/H024921/1. The data used for this publication is available from https://doi.org/10.15125/BATH-00515. K.K. authored the paper, compiled contributions from co-authors and performed the analysis of the radio data. S.G. collated and performed the analysis of the meteorological and lightning data. A.B. provided the electrostatic data and provided advice for the ideas in this paper. Z.L. assisted in the collection of the radio data. M.F. supervised the work of K.K. and S.G. Thanks also go to Météorage for providing the lightning data.

References

R. Barr, D. Llanwyn Jones, and C. J. Rodger. ELF and VLF radio waves. *Journal of Atmospheric and Solar-Terrestrial Physics*, 62(17–18):1689–1718, November 2000. ISSN 1364-6826. doi: 10.1016/S1364-6826(00)00121-8.

A. J. Bennett. Identification and ranging of lightning flashes using co-located antennas of different geometry. *Meas. Sci. Technol.*, 24(12):125801, 2013. ISSN 0957-0233. doi: 10.1088/0957-0233/24/12/125801.

K. G. Budden. *The Propagation of Radio Waves: The Theory of Radio Waves of Low Power in the Ionosphere and Magnetosphere*. Cambridge University Press, University Press, Cambridge, UK, first paperback edition (with corrections) edition, 1988. ISBN 0 521 36952 2.

Mark A. Clilverd, Roger Duthie, Craig J. Rodger, Rachael L. Hardman, and Keith H. Yearby. Long-term climate change in the D-region. *Scientific Reports*, 7(1):16683, November 2017. ISSN 2045-2322. doi: 10.1038/s41598-017-16891-4.

Benjamin R. T. Cotts and Umran S. Inan. VLF observation of long ionospheric recovery events. *Geophys. Res. Lett.*, 34(14):L14809, July 2007. ISSN 1944-8007. doi: 10.1029/2007GL030094.

S. A. Cummer, U. S. Inan, and T. F. Bell. Ionospheric D region remote sensing using VLF radio atmospherics. *Radio Sci.*, 33(6):1781–1792, November 1998. ISSN 1944-799X. doi: 10.1029/98RS02381.

R. L. Dowden, J. B. Brundell, and W. A. Lyons. Are VLF rapid onset, rapid decay perturbations produced by scattering off sprite plasma? *J. Geophys. Res.*, 101 (D14):19175–19183, August 1996. ISSN 2156-2202. doi: 10.1029/96JD01346.

M. Füllekrug. Wideband digital low-frequency radio receiver. *Meas. Sci. Technol.*, 21(1):015901, January 2010. ISSN 0957-0233. doi: 10.1088/0957-0233/21/1/015901.

Martin Füllekrug, Nathan Smith, Andrew Mezentsev, Robert Watson, Ivan Astin, Stéphane Gaffet, Adrian Evans, and Michael Rycroft. Multipath propagation of low-frequency radio waves inferred from high-resolution array analysis. *Radio Sci.*, 50(11):1141–1149, November 2015. ISSN 1944-799X. doi: 10.1002/2015RS005781.

E. S. Gemelos, Umran S. Inan, M. Walt, Michel Parrot, and Jean-André Sauvaud. Seasonal dependence of energetic electron precipitation: Evidence for a global role of lightning. *Geophysical Research Letters*, 36(21), November 2009. ISSN 0094-8276. doi: 10.1029/2009GL040396.

N. C. Gross, M. B. Cohen, R. K. Said, and M. Gołkowski. Polarization of Narrowband VLF Transmitter Signals as an Ionospheric Diagnostic. *J. Geo-*

phys. Res. Space Physics, 123(1):901–917, January 2018. ISSN 2169-9402. doi: 10.1002/2017JA024907.

C. Haldoupis, R. J. Steiner, Á. Mika, S. Shalimov, R. A. Marshall, U. S. Inan, T. Bösinger, and T. Neubert. "Early/slow" events: A new category of VLF perturbations observed in relation with sprites. *J. Geophys. Res. Space Physics*, 111(A11), November 2006. ISSN 2156-2202. doi: 10.1029/2006JA011960.

Christos Haldoupis, Morris Cohen, Benjamin Cotts, Enrico Arnone, and Umran Inan. Long-lasting D-region ionospheric modifications, caused by intense lightning in association with elve and sprite pairs. *Geophys. Res. Lett.*, 39(16): L16801, August 2012. ISSN 1944-8007. doi: 10.1029/2012GL052765.

R. A. Helliwell, J. P. Katsufrakis, and M. L. Trimpi. Whistler-induced amplitude perturbation in VLF propagation. *J. Geophys. Res.*, 78(22):4679–4688, August 1973. ISSN 2156-2202. doi: 10.1029/JA078i022p04679.

U. S. Inan, T. F. Bell, and J. V. Rodriguez. Heating and ionization of the lower ionosphere by lightning. *Geophys. Res. Lett.*, 18(4):705–708, April 1991. ISSN 1944-8007. doi: 10.1029/91GL00364.

U. S. Inan, T. F. Bell, V. P. Pasko, D. D. Sentman, E. M. Wescott, and W. A. Lyons. VLF signatures of ionospheric disturbances associated with sprites. *Geophys. Res. Lett.*, 22(24):3461–3464, December 1995. ISSN 1944-8007. doi: 10.1029/95GL03507.

U. S. Inan, D. Piddyachiy, W. B. Peter, J. A. Sauvaud, and M. Parrot. DEMETER satellite observations of lightning-induced electron precipitation. *Geophys. Res. Lett.*, 34(7):L07103, April 2007. ISSN 1944-8007. doi: 10.1029/2006GL029238.

U. S. Inan, S. A. Cummer, and R. A. Marshall. A survey of ELF and VLF research on lightning-ionosphere interactions and causative discharges. *J. Geophys. Res. Space Physics*, 115(A6):A00E36, June 2010. ISSN 2156-2202. doi: 10.1029/2009JA014775.

Umran S. Inan, Victor P. Pasko, and Timothy F. Bell. Sustained heating of the ionosphere above thunderstorms as evidenced in "early/fast" VLF events. *Geophys. Res. Lett.*, 23(10):1067–1070, May 1996. ISSN 1944-8007. doi: 10.1029/96GL01360.

A. R. Jameson, M. J. Murphy, and E. P. Krider. Multiple-Parameter Radar Observations of Isolated Florida Thunderstorms during the Onset of Electrification. *J. Appl. Meteor.*, 35(3):343–354, March 1996. ISSN 0894-8763. doi: 10.1175/1520-0450(1996)035<0343:MPROOI>2.0.CO;2.

Kuang Liang Koh, Zhongjian Liu, and Martin Füllekrug. Lower ionosphere effects on narrowband VLF transmission propagation: Fast variabilities and frequency dependence. *Radio Sci.*, 2018. doi: 10.1002/2017RS006456.

Sushil Kumar, Abhikesh Kumar, and Craig J. Rodger. Subionospheric early VLF perturbations observed at Suva: VLF detection of red sprites in the day? *J. Geophys. Res. Space Physics*, 113(A3):A03311, March 2008. ISSN 2156-2202. doi: 10.1029/2007JA012734.

Ningyu Liu, Matthew G. McHarg, and Hans C. Stenbaek-Nielsen. High-altitude electrical discharges associated with thunderstorms and lightning. *Journal of Atmospheric and Solar-Terrestrial Physics*, 136, Part A:98–118, December 2015. ISSN 1364-6826. doi: 10.1016/j.jastp.2015.05.013.

Zhongjian Liu, Kuang Liang Koh, Andrew Mezentsev, Sven-Erik Enno, Jacqueline Sugier, and Martin Füllekrug. Variable phase propagation velocity for long-range lightning location system. *Radio Sci.*, 51(11):1806–1815, November 2016. ISSN 1944-799X. doi: 10.1002/2016RS006058.

R. A. Marshall and U. S. Inan. Two-dimensional frequency domain modeling of lightning EMP-induced perturbations to VLF transmitter signals. *J. Geophys. Res.*, 115(A6):A00E29, June 2010. ISSN 2156-2202. doi: 10.1029/2009JA014761.

R. A. Marshall, U. S. Inan, and W. A. Lyons. On the association of early/fast very low frequency perturbations with sprites and rare examples of VLF backscatter. *J. Geophys. Res. Atmos.*, 111(D19):D19108, October 2006. ISSN 2156-2202. doi: 10.1029/2006JD007219.

Á Mika and C. Haldoupis. VLF Studies During TLE Occurrences in Europe: A Summary of New Findings. *Space Sci Rev*, 137(1-4):489–510, June 2008. ISSN 0038-6308, 1572-9672. doi: 10.1007/s11214-008-9382-8.

T. Neubert, M. Rycroft, T. Farges, E. Blanc, O. Chanrion, E. Arnone, A. Odzimek, N. Arnold, C.-F. Enell, E. Turunen, T. Bösinger, Á Mika, C. Haldoupis, R. J. Steiner, O. van der Velde, S. Soula, P. Berg, F. Boberg, P. Thejll, B. Christiansen, M. Ignaccolo, M. Füllekrug, P. T. Verronen, J. Montanya, and N. Crosby. Recent Results from Studies of Electric Discharges in the Mesosphere. *Surv Geophys*, 29(2):71–137, September 2008. ISSN 0169-3298, 1573-0956. doi: 10.1007/s10712-008-9043-1.

Victor P. Pasko, Umran S. Inan, Yuri N. Taranenko, and Timothy F. Bell. Heating, ionization and upward discharges in the mesosphere, due to intense quasi-electrostatic thundercloud fields. *Geophys. Res. Lett.*, 22(4):365–368, February 1995. ISSN 1944-8007. doi: 10.1029/95GL00008.

Victor P. Pasko, Umran S. Inan, and Timothy F. Bell. Ionospheric effects due to electrostatic thundercloud fields. *Journal of Atmospheric and Solar-Terrestrial Physics*, 60(7–9):863–870, May 1998. ISSN 1364-6826. doi: 10.1016/S1364-6826(98)00022-4.

Victor P. Pasko, Yoav Yair, and Cheng-Ling Kuo. Lightning Related Transient Luminous Events at High Altitude in the Earth's Atmosphere: Phenomenology, Mechanisms and Effects. *Space Sci Rev*, 168(1-4):475–516, June 2012. ISSN 0038-6308, 1572-9672. doi: 10.1007/s11214-011-9813-9.

Craig J Rodger. Subionospheric VLF perturbations associated with lightning discharges. *Journal of Atmospheric and Solar-Terrestrial Physics*, 65(5):591–606, March 2003. ISSN 1364-6826. doi: 10.1016/S1364-6826(02)00325-5.

Mohammad A. Salem, Ningyu Liu, and Hamid K. Rassoul. Modification of the lower ionospheric conductivity by thunderstorm electrostatic fields. *Geophys. Res. Lett.*, 43(1):5–12, January 2016. ISSN 1944-8007. doi: 10.1002/2015GL066933.

Xuan-Min Shao, Erin H. Lay, and Abram R. Jacobson. Reduction of electron density in the night-time lower ionosphere in response to a thunderstorm. *Nature Geosci*, 6(1):29–33, January 2013. ISSN 1752-0894. doi: 10.1038/ngeo1668.

Maribeth Stolzenburg, Thomas C. Marshall, and Paul R. Krehbiel. Initial electrification to the first lightning flash in New Mexico thunderstorms. *J. Geo-*

phys. Res. Atmos., 120(21):11253–11276, November 2015. ISSN 2169-8996. doi: 10.1002/2015JD023988.

Yukihiro Takahashi, Rina Miyasato, Toru Adachi, Kazuhiro Adachi, Masaaki Sera, Akihiro Uchida, and Hiroshi Fukunishi. Activities of sprites and elves in the winter season, Japan. *Journal of Atmospheric and Solar-Terrestrial Physics*, 65 (5):551–560, March 2003. ISSN 1364-6826. doi: 10.1016/S1364-6826(02)00330-9.

Y. N. Taranenko, U. S. Inan, and T. F. Bell. Interaction with the lower ionosphere of electromagnetic pulses from lightning: Heating, attachment, and ionization. *Geophys. Res. Lett.*, 20(15):1539–1542, August 1993. ISSN 1944-8007. doi: 10.1029/93GL01696.

Neil R. Thomson, Mark A. Clilverd, and Craig J. Rodger. Midlatitude ionospheric D region: Height, sharpness, and solar zenith angle. *J. Geophys. Res. Space Physics*, 122(8):8933–8946, August 2017. ISSN 2169-9402. doi: 10.1002/2017JA024455.

H. D. Voss, W. L. Imhof, M. Walt, J. Mobilia, E. E. Gaines, J. B. Reagan, U. S. Inan, R. A. Helliwell, D. L. Carpenter, J. P. Katsufrakis, and H. C. Chang. Lightning-induced electron precipitation. *Nature*, 312(5996):740–742, December 1984. doi: 10.1038/312740a0.

James R Wait and K. P Spies. *Characteristics of the Earth-Ionosphere Waveguide for VLF Radio Waves*, volume NBS Technical Note 300. U.S. Department of Commerce, National Bureau of Standards, Boulder, CO, 1964. OCLC: 7958918.

F. G. Zoghzoghy, M. B. Cohen, R. K. Said, and U. S. Inan. Statistical patterns in the location of natural lightning. *J. Geophys. Res. Atmos.*, 118(2):787–796, January 2013. ISSN 2169-8996. doi: 10.1002/jgrd.50107.

Chapter 5

Multi-frequency observations of Early sub-ionospheric radio disturbances caused by lightning

Commentary

This paper presents observations of 22 lightning ionospheric disturbance events which occur concurrently with a lightning discharge with rise times $<$500 ms gradual recoveries $>$10 s. Events with these characteristics are called Early events and thought to result from direct lightning ionospheric coupling mechanisms. However, the locations of the causative lightning are displaced from the disturbed propagation paths for most events such that forward scattering off a horizontal ionospheric perturbation structure is unlikely to be the disturbance mechanism. The causative lightning waveforms were studied and found to match sprite producing lightning - all causative lightning were identified to be positive cloud-to-ground lightning with continuing current component. It is thus most likely that the observations were of wide angle scattering off sprite plasma. Comparing the disturbance signatures on the transmissions propagating over the same path, a frequency dependence is seen - this demonstrates the importance of the transmitter frequency in detection of Early events. These are also the first observations of wide angle scattering off sprite plasma using multiple frequencies.

<table>
<tr><th colspan="10">This declaration concerns the article entitled:</th></tr>
<tr><td colspan="10">Multi-frequency observations of Early sub-ionospheric radio disturbances caused by lightning</td></tr>
<tr><td colspan="10">Publication status (tick one)</td></tr>
<tr><td>draft manuscript</td><td>✓</td><td>Submitted</td><td></td><td>In review</td><td></td><td>Accepted</td><td></td><td>Published</td><td></td></tr>
<tr><td>Publication details (reference)</td><td colspan="9">Kuang Liang Koh, Simon Ghilian, Adam Peverell, Zhongjian Liu, Alec Bennett and Martin Füllekrug. Multi-frequency observations of Early sub-ionospheric radio disturbances caused by lightning. 2018.</td></tr>
<tr><td>Candidate's contribution to the paper (detailed, and also given as a percentage).</td><td colspan="9">The candidate contributed to/ considerably contributed to/predominantly executed the…

Formulation of ideas:
90%
Discussion of ideas with M.F. and A.B.

Design of methodology:
100%

Experimental work:
80%
Z.J. assisted with the collection of the radio data
BTD-300 data provided by A.B.
Lightning location data provided by Meteorage and compiled by S.G.
A.P. examined the lightning waveforms from the radio data

Presentation of data in journal format:
90%
S.G. provided the plots of the Meteorage data</td></tr>
<tr><td>Statement from Candidate</td><td colspan="9">This paper reports on original research I conducted during the period of my Higher Degree by Research candidature.</td></tr>
<tr><td>Signed</td><td colspan="5"></td><td>Date</td><td colspan="3"></td></tr>
</table>

Multi-frequency observations of Early sub-ionospheric radio disturbances caused by lightning

Kuang Koh, S. Ghilain, A. Peverell,

Z. Liu, A. Bennett, M. Füllekrug

key point #1: 22 Early events were observed using high time resolution analysis together with their causative lightning

key point #2: Disturbances are found to be frequency selective

key point #3: Causative lightning suggests disturbances result from wide angle scattering

Abstract

Ionospheric perturbations caused by lightning are localised and can be detected as disturbances on sub-ionospheric radio transmissions. These transmissions typically utilise different parts of the frequency spectrum from 15–30 kHz and are geographically dispersed. Therefore, previous observations of lightning ionospheric perturbation on any one propagation path are usually at a single frequency. Using a unique geometry, lightning ionospheric disturbances events were observed on a propagation path with multiple frequencies in the range 19.53–60 kHz. These disturbance events were found to exhibit differences with frequency that are likely to be propagation related. This frequency dependence is important for the interpretation of sub-ionospheric radio detection of lightning ionospheric perturbations.

Causative lightning of the events are examined from broadband radio recordings and are seen to match sprite producing +CG flashes with the exception of one event which was coincident with a 20 ms sferic burst. Such sferic bursts have also previously been

associated with sprite production. The events observed are most probably a result of wide angle scattering off sprite plasma.

1 Introduction

Lightning is known to produce ionospheric conductivity perturbations which are detectable as disturbances in sub-ionospheric radio transmissions [Rodger, 2003, Mika and Haldoupis, 2008, Inan et al., 2010]. There is a broad class of such disturbances called Early events that are observed to occur almost simultaneously with the causative lightning. This 'early' nature of the disturbance is associated with more direct mechanisms by which lightning modifies ionospheric conductivity. One of the proposed mechanisms for lightning-ionospheric perturbations is through the interaction of lightning ElectroMagnetic Pulse (EMP) with ionospheric gases causing heating and ionisation [Inan et al., 1991, Taranenko et al., 1993]. A second mechanism is the heating and ionisation caused by strong transient Quasi Electrostatic (QE) fields that is produced above the thunderstorm after lightning has neutralised some of the thundercloud charge [Pasko et al., 1995, Pasko, 2010, Liu et al., 2015]. These perturbations can also produce optical phenomena such as ELVES from EMP [Fukunishi et al., 1996, van der Velde and Montanyà, 2016, Blaes et al., 2016], sprite halos and sprites from QE [Franz et al., 1990, Sentman et al., 1995, Frey et al., 2007, Soula et al., 2015] - collectively termed Transient Luminous Events (TLEs).

Early event disturbances are also characterised by rise and recovery times that are linked to the specific nature of the perturbation. Early/fast events have almost instantaneous rise times that is typically limited to the observation time resolution of $\sim$20 ms typically. This fast rise time is thought to arise from the direct nature of the lightning-ionospheric coupling. Subsequently, Early/slow events that have rise times 0.5–2.5 s were identified and attributed to cumulative effects of successive lightning discharges [Haldoupis et al., 2006, Marshall and Inan, 2010, Marshall et al., 2010]. Recovery times of Early events are observed to be $\sim$10–100 s [Sampath et al., 2000] consistent with the ionospheric response to heating and ionisation at the altitudes of the perturbation. However, LOng Recovery Early (LORE) events have been documented with $\gg$200 s recovery times [Cotts and Inan, 2007, Haldoupis et al., 2012].

Simultaneous optical and radio observations were used to study the link between Early events and TLEs. However, such studies produced conflicting results. Attributing Early events to the wide angle scattering off sprite plasma, an almost one-to-one correspondence between Early events and sprites was found by [Dowden et al., 1996b, Hardman et al., 1998]. The correspondence was also reported by [Haldoupis et al., 2004] but from only narrow angle forward scattering. Further observations found only 5% of sprites produced detectable backscatter [Mika et al., 2005].

Using a linear array of receivers (HAIL array), [Johnson et al., 1999] determined the scattering pattern of Early events to be narrow angle forward scattering. This result was later attributed to scattering off sprite halos [Barrington-Leigh et al., 2001, Moore et al., 2003]. Further, [Marshall et al., 2006] reported only 48% of sprites occurred with Early events and that 39% of Early events occurred with no sprite observation and concluded that only sprites with large horizontal extents are able to produce back scatter.

EMP produced ELVEs have also been observed with Early event disturbances [Mika et al., 2006] and was proposed to be the mechanism for LORE events [Haldoupis et al., 2013]. However, the conductivity perturbation from all but the strongest lightning EMP are thought to be small and not likely to produce the observed disturbances [Marshall and Inan, 2010, Kotovsky and Moore, 2017], although cumulative effects from successive lightning EMP may be able to [Marshall et al., 2010, Marshall and Inan, 2010].

The inconsistencies in the observations may be due to a multitude of background conditions like the causative lightning character or location, thunderstorm charge structure or the ambient ionospheric conductivity profile. Sensor geometry may also account for some of the inconsistencies in the observations [c.f. NaitAmor et al., 2017]. Particularly, the observed transmission disturbances was shown to be strongly dependent on the transmission frequency [Marshall and Inan, 2010]. This work presents an observation of 22 Early events from two thunderstorms on the evening of 27th August 2016. A novel sensor geometry (section 2) was used in combination with a high time and frequency resolution analysis method (section 3) so that several frequencies in the range 19.53–60 kHz was sampled on one North-South propagation path. Another propagation path was monitored using two closely separated frequencies ∼23.35 kHz and 23.45 kHz. This set up allows an

investigation of disturbances on separate frequency signals over the same path. The observed early events, the thunderstorm conditions and causative lightning characteristics are presented in sections 4, 5 and 6. Details of two events are shown as example in section 7. The results presented show the frequency dependence of early event disturbances.

2 Experimental data

Vertical electric field measurements were taken in Bath, UK over a full day from 27th August 2016 00:28:43 UTC to 28th August 2016 00:28:18 UTC with a single wideband (4 Hz–400 kHz) receiver. The receiver samples at 1 MHz frequency with an amplitude resolution of 35 μV and timing accuracy of 20 ns [Füllekrug, 2010]. The radio recordings were used to observe lower ionospheric perturbation signals from 4 different sub-ionospheric radio transmissions with callsigns GBZ, GQD, DHO and MSF. The GBZ broadcast is transmitted from the same station as the MSF timing signal in Anthorn, UK on a North-South path. GQD is transmitted from nearby Skelton, UK so that it can be considered as having the same path as GBZ and MSF. DHO is transmitted from Rhauderfehn, Germany on an East-West path. These transmissions operate at different frequencies with narrow bandwidths from 19.53–60 kHz [Koh et al., 2018b, table 1]. The causative lightning waveforms of the disturbance events is also identified from the radio data.

Measurements from an quasi-electrostatic field sensor (BTD-300) located in Portishead is also available. The BTD-300 measures the vertical electric field from 1–50 Hz on three co-located antennas so that it is able to distinguish electric field changes due to nearby thunderstorm electrical activity from changes caused by local sources such as corona discharge, space charge variability and precipitation [Bennett, 2013]. Lightning electrostatic field changes normally have an inverse cube relationship with distance so that the sensor should be insensitive to signals from lightning >100 km away. The BTD-300 is synchronised to GPS once per day so that the crystal oscillator time drift is limited to about 2 s over a day. The locations of the radio receiver, BTD-300 and transmitter sites are marked on figure 1 as triangles and diamonds (see figure legend).

Cloud top temperatures are available from the Meteosat satellite allowing the

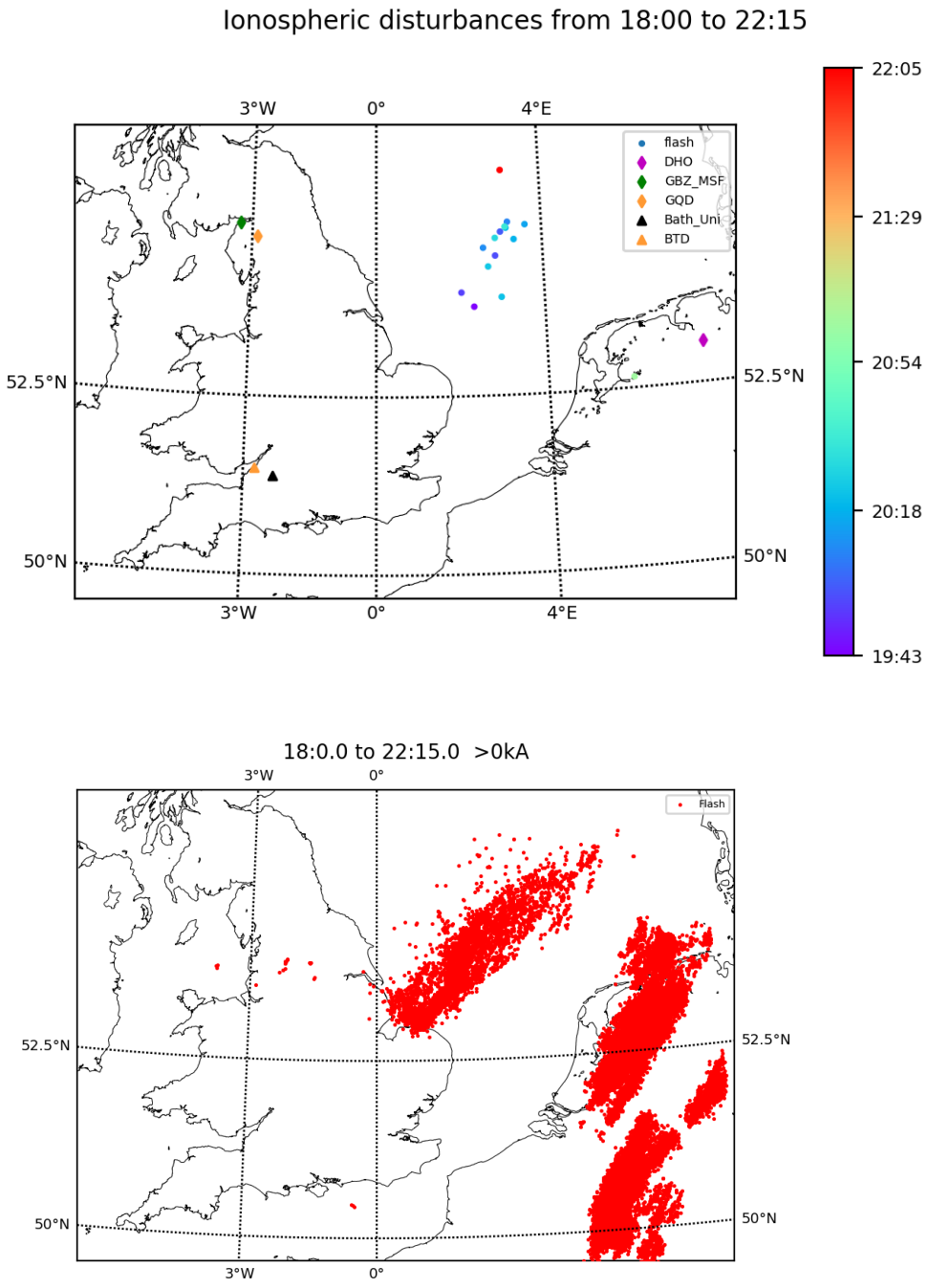

Fig. 1: Map of experimental set up and thunderstorm. (Top) Experimental set up and causative lightning locations of Early events. The location of the wideband radio receiver in Bath, UK and the BTD-300 in Portishead are marked with black and yellow triangles respectively. The transmitter sites are marked by different coloured diamonds, GBZ/MSF in green, GQD in yellow and DHO in purple. The causative locations are shown by dots with colours that correspond to the time of occurrence (Bottom) Lightning locations provided by Météorage from 18:00 UTC until 23:59 UTC. The track of the both thunderstorms can be seen moving in a north east direction.

thunderstorms in the area to be tracked through the satellite images. Lightning location and intensity (peak current) data is available from Météorage. Each discharge is also categorised by polarity (+ or -) and Cloud to Ground (CG) or Intra-Cloud (IC) in the data.

3 Ionospheric signals using sub-ionospheric radio

The modulation of information on each transmission has to be removed to observe perturbations in the lower ionosphere. The methodology used is the same as that used by [Koh et al., 2018a]. A general description of the method is as follows. The real-valued time series data is first converted to a complex baseband time series using the Hilbert transform. This is done by frequency shifting and filtering the data to remove negative frequencies and isolate the frequencies of interest [Liu et al., 2016, section 3.1]. This time series can be represented by $y_c(t) = A(t)e^{i\varphi(t)}$ where $A(t)$ is the amplitude and $\varphi(t)$ is the phase of the signal. These can be calculated for each sample in $y_c(t)$ by taking the modulus $A(t) = |y_c(t)|$ and argument $\varphi(t) = \arctan(\frac{\Im[y_c(t)]}{\Re[y_c(t)]})$. Secondly, the received complex time series is demodulated to obtain the message symbol sequence. A simulated transmission is produced using this symbol sequence and the deviation of the received transmission from the simulated transmission is taken as the ionospheric signal amplitude $|y_i|$ and phase φ_i.

Since the ionospheric signal is based upon the simulated transmission, the assumption is that the transmission is stable and follows its modulation scheme perfectly. This is not always valid and instances of phase jumps and frequency offset have been reported [Gross et al., 2018, Thomson et al., 2017]. A phase ramp in the disturbance signal of DHO is observed in this data (not shown) that is symptomatic of it being transmitted at a frequency offset from its published centre frequency. An offset of 61.73 μHz is used here for the centre frequency of DHO to remove the phase ramp - this is the same offset used by [Thomson et al., 2017] for DHO. All other phase jumps and ramps in the data are attributed to ionospheric effects, i.e. the events described in the following section 4.

The MSK modulated GBZ, GQD and DHO transmissions have higher and lower sideband frequencies each that is centred symmetrically about the centre frequency. Both frequencies are monitored separately in this study to account for

the frequency dependent propagation of the sidebands. The MSF transmission is a timing signal service using On-Off Modulation (OOM). The time information is encoded in the amplitude modulation in the first half of each second and the phase of MSF is effectively noise during the 'off' symbols (which are removed from the analysis). The 'off' to 'on' transitions exhibits some amplitude inconsistency over short periods <1 s [Koh et al., 2018b] so the MSF amplitude is not used in this study.

4 Early events

A total of 22 separate disturbance events were identified in the ionospheric signals with 10 of the events occurring on multiple transmissions. All events occurred after sunset over the propagation path, in twilight or night time conditions with the first clearly discernible event at 19:40:04.670 UTC. This event is presented as an example with disturbances on multiple transmissions and both propagation paths in section 7.1 and is representative of most of the 22 events. The events are detected using the 1 s statistical modes of the ionospheric signals so that natural variability and interference is reduced. This should allow smaller magnitude events to be unambiguously found but also precludes effects with durations <1 s, for example, Rapid Onset Rapid Decay events [Dowden et al., 1994, 1996a]. The onset time of each event is pinpointed from the μs resolution ionospheric signal calculated from each sample of the radio data. The causative lightning of each event is identified from the broadband radio data by finding the lightning waveform nearest the onset time. All event onsets are found to be coincident with lightning thus classifying the disturbances as Early events. Since both ionospheric signals and causative lightning are found from the same radio data, there can be no error in the coincidence. Table 1 summarises the characteristics of each event numbered #1–22. The event time is given by the UTC of the causative lightning (column headed 'UTC'). The change in log amplitude ($\delta \log_{10} |y_i|$) and phase ($\delta\varphi_i$) from pre-event to its peak level is determined from the 1 s statistical modes to mitigate interference from the causative lightning. The log amplitude changes are range from -0.04–0.03 $\log_{10}(\mathrm{Vm}^{-1})$ and the phase changes range from -0.4–1.9 μs.

It is possible to compare the disturbance on the ionospheric signal between each sideband frequency of an MSK transmission directly to show changes in the fre-

#	UTC	+CG	dNS	dEW	B	GBZ H(L)			GQD H(L)			DHO H(L)			MSF
						A	$\delta\varphi_i$	$\delta\tau_e$	A	$\delta\varphi_i$	$\delta\tau_e$	A	$\delta\varphi_i$	$\delta\tau_e$	$\delta\varphi_i$
01	19:40:04.670	161.19	330	170	Y	-	-	-	(-1)	-	-40	-	0.2(0.25)	-	-0.1
02	19:43:54.361	176.52	360	150	-	-	-	-	-	-	-	-	0.3(0.3)	-	-
03	19:54:21.596	-	-	-	a	-	-	-	1(1)	(0.1)	50	1(1)	(0.2)	30	-
04	19:55:33:399	81.38	330	180	Y	-	-	-	-	-0.2(-0.2)	-	-	-	-	-0.2
05	19:57:38.124	97.87	390	220	Y	-	-	-	-	-	-	-	0.4(0.4)	-	-
06	20:00:30.700	158.53	400	260	a	-	-	-	-	-	-	(-1)	0.3(0.3)	-	-
07	20:08:54.641	35.36	410	270	-	-	-	-	-	-	-	-	0.5(0.5)	-	-
08	20:10:56.325	44.4	370	240	-	-3	(-0.4)	-100	1(1)	-	-	-	-0.4(-0.4)	-	-
09	20:15:32.567	66.58	440	260	Y	-	-	-	-	-	-	(-2)	-	-	-
10	20:18:25.048	121.45	420	240	-	-	-	-	-	-	-	-2(-2)	(-0.3)	-	-
11	20:20:48.558	126.17	410	260	-	-	0.2(-0.1)	-60	-	-0.1(-0.1)	-	-	-0.2(-0.2)	-	-
12	20:22:34.188	456.29	390	160	-	-	-	-	-	-	-	(-1)	1.5(1.9)	80	-
13	20:24:20.854	122.73	370	210	a	-	0.3(0.2)	20	-	-	-	-	-	-	-
14	20:29:53.148	68.99	390	250	Y	-	-	-20	-	-	-20	-1(-1)	-	-	-
15	20:35:57.891	146.16	410	260	Y	-	-	-	-	-	-	-3(-4)	0.5(0.3)	-20	-
16	20:43:30.980	100.52	600	20	a	-	-	20	-	-	-20	-	0.3(0.3)	-	-
17	21:03:13.184	198.33	590	20	Y	-	-	-	-	-	-	-1(-2)	-	-	-
18	21:04:00.186	-	600	$<$10	a	-	-	-	-	-	-	-4(-4)	0.2(0.1)	-	-
19	21:25:41.964	-	420	260	a	-	-	20	-	-	-	3(3)	-0.3	30	-0.2
20	21:53:42.335	169.62	490	240	-	-	-	-	-	0.2(0.1)	-30	2(2)	(0.3)	40	-
21	22:05:23.509	116.24	410	380	-	-	-	-	-	-	-20	2(2)	-0.3	50	-
22	22:44:19.804	-	-	-	-	-	-	-	-	-	-	2(2)	(0.3)	60	-

Tab. 1: Summary of observed Early events. The time of the causative lightning is given in the 'UTC' column. The '+CG' column gives the peak current in kA. Causative distances in kilometres to the North-South and DHO paths are shown in the 'dNS', and 'dEW' columns. Coincidence with the BTD-300 is shown in the 'B' column where 'Y' denotes and unambiguous match and 'a' is an ambiguous match (see section 6). The changes in log amplitude $100\delta \log_{10} |y_i|$ (presented with the 100 times factor for brevity) in $100\log_{10} \mathrm{Vm}^{-1}$, $\delta\varphi_i$ in μs and delay $\delta\tau_e$ also in μs are also shown for each transmission in the 'A', '$\delta\varphi_i$' and '$\delta\tau_e$' columns.

quency response of the propagation due to the ionospheric perturbation. Several events display a dissimilarity between the disturbance on each sideband. $\delta \log_{10} |y_i|$ and $\delta\varphi_i$ are determined for each sideband of a MSK modulated transmission separately. The values quoted in outside brackets in table 1 are for the higher sideband frequency and the values in brackets are for the lower sideband frequency.

The phase frequency response is a group delay $\tau(\omega) = \frac{\mathrm{d}}{\mathrm{d}\omega}\varphi$ which has been shown to be sensitive to diurnal ionospheric changes [Koh et al., 2018a, section 5] A linear approximation of $\tau(\omega)$ can be calculated from the difference between the phase disturbance at each sideband. However, there can be a non-linear frequency dependence even over the narrow bandwidth of the transmission [Koh et al., 2018a, figure 3]. Therefore, the linear approximation of the group delay is computed using the cross correlation of the simulated and received transmissions every 1 s. This is equivalent to a linear fit of the phase frequency response using all the frequency components of the transmission as opposed to only the 2 sideband frequencies. The cross correlation operation uses all samples, including the transitions between the symbols. This delay estimate is referred to as τ_e; the change in τ_e from pre-event to peak level $\delta\tau_e$ is shown in table 1 for each MSK modulated transmission. A number of disturbances are only detectable in the τ_e signal; For example, $\delta\tau_e$ on GBZ and GQD produced by event #16 are shown in figure 2 but there is no clear $\delta\varphi_i$ at the event onset. The disturbances on τ_e is seen to have fast rise time ($<$1 s, the time resolution of the τ_e measurement) and a gradual recovery that is $\sim$30 s on both GBZ and GQD. The fast rise and gradual recovery characteristics are representative of the τ_e disturbances for the other events, i.e. they have similar characteristics to disturbances in $|y_i|$ or φ_i.

5 Thunderstorms

The early events were produced by lightning origination from two big thunderstorms that developed over Northern Europe on 27th August 2016. Around 11 UTC, convection started on the southern coast of the UK (over Weymouth, Dorset) to produce the first thunderstorm. The thunderstorm grew and moved Northward so that by 18 UTC, the thunderstorm was an electrically active MCS $<$100 km (at its nearest point) East of the North-South propagation path of GBZ, GQD and MSF and North of the DHO propagation path. After sunset over the

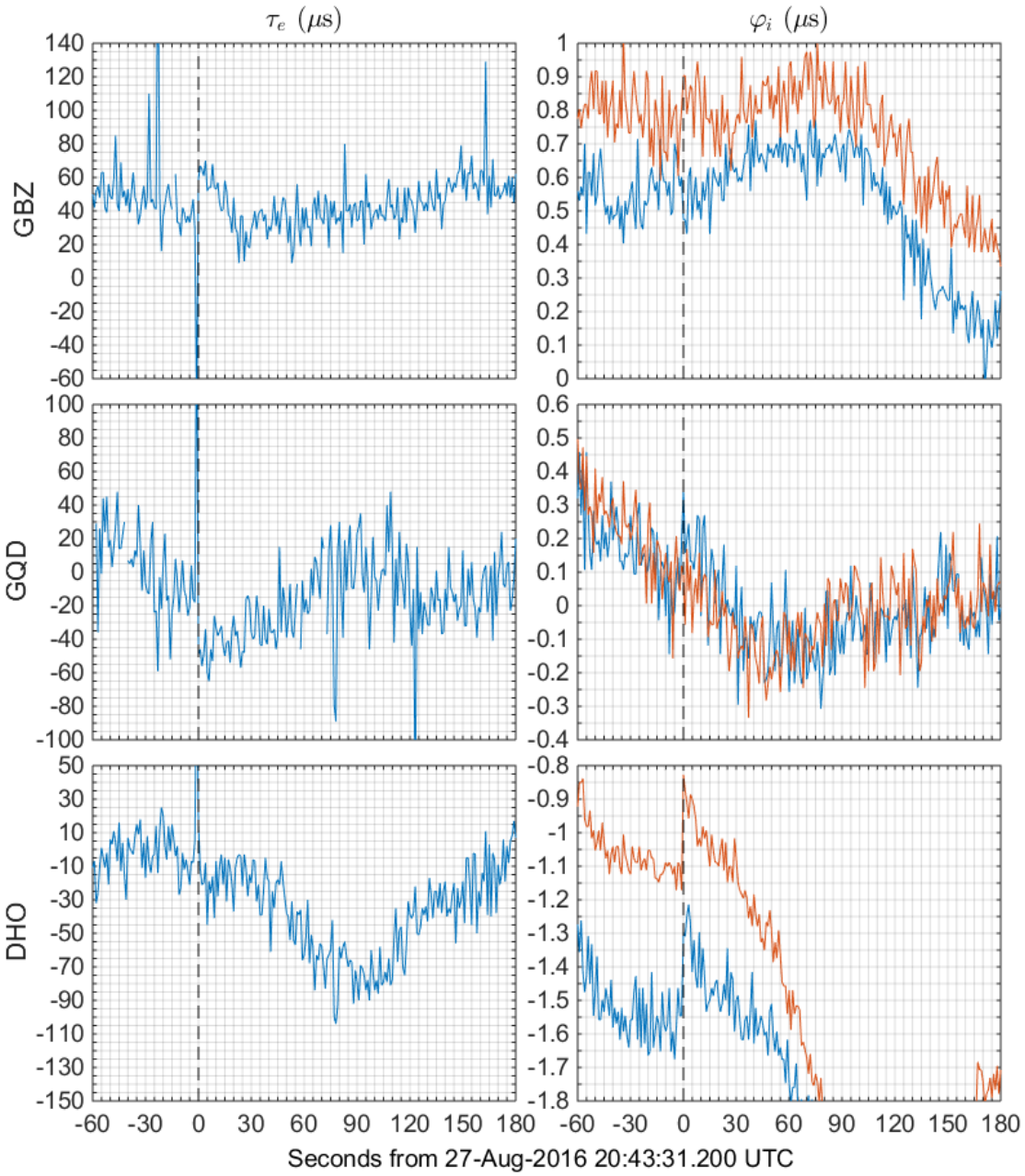

Fig. 2: Event #16 (left) delay τ_e and (right) phase ϕ_i signal for MSK modulated transmissions GBZ, GQD and DHO. The disturbances on GBZ and GQD are only seen in τ_e.

NS path (19:16 UTC), the MCS had moved East and almost completely offshore ≥200 km away from the North-South propagation path but remains about the same distance from the DHO propagation path. The second thunderstorm started over the Netherlands ∼17:45 UTC and was intensifying over the night. This thunderstorm is ≥500 km from the North-South propagation path but <100 km from the DHO propagation path throughout. The track of the two thunderstorms after 18 UTC can be seen from figure 1 bottom panel which shows all the lightning located in the area from 18–22:15 UTC.

The lightning activity for the first thunderstorm between 18–22:15 UTC is presented in figure 3, top panel. The number of lightning discharges and the sum of their peak currents every minute is decreasing throughout this period. The changes in the cloud area of this thunderstorm is shown in the next panel of figure 3. The cloud areas and heights were determined from the satellite cloud top temperature data which is sampled at 15 minute intervals. The cloud area above 11 km is seen to be also decreasing throughout this period indicating that the thunderstorm is in the decay stage. Increases in the areas of lower cloud tops can be attributed to the collapse of areas with higher cloud tops to the lower altitude. At around 19 UTC the integrated peak current is seen to increase by a larger amount than the number of discharges so that the average peak current of each flash must be higher. The disturbances occur after and are shown in green dots on both panels. The second thunderstorm is presented in the same format in the bottom two panels and is seen to be growing in this period as evidenced by the increasing lightning activity and area of cloud with top heights above 11 km.

6 Causative lightning

The location of each event causative lightning is found from its time coincidence (<5 ms) with Météorage reported lightning locations. Not all event causative lightning were located in this way. Causative lightning that were located are shown in figure 1. The distance from causative lightning location to the North-South and DHO propagation paths are indicated in the columns headed ‘dNS’ and ‘dEW’ of table 1 respectively. The distances to the North -South path range from 600 km (event #16) to 330 km (events #1 and 4). For the DHO path, the longest distance is 380 km (event #21) and the shortest is almost on the path (event

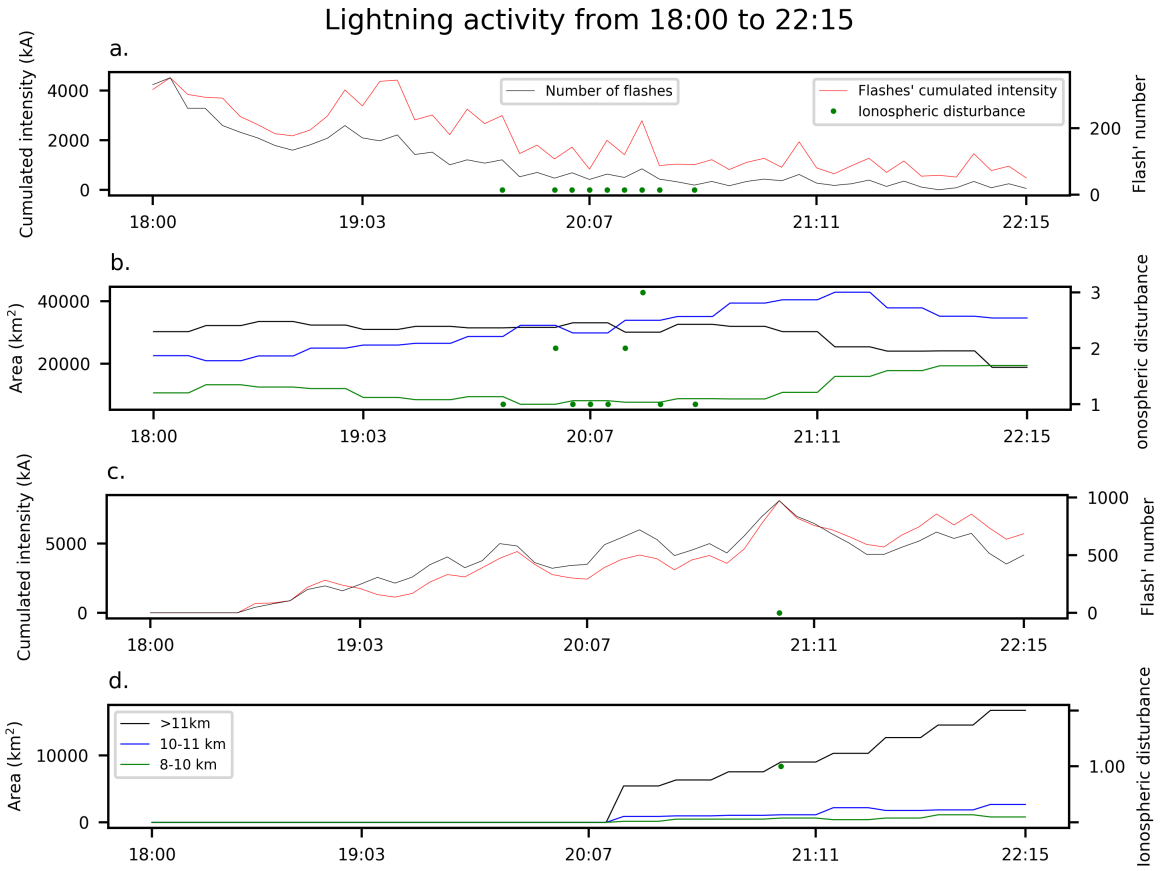

Fig. 3: Thunderstorm development and lightning activity on 27th August 2016 18–22:15 UTC. (Top) Total lightning number and cumulated intensity every 15 minutes and (second from top) cloud areas distinguished by cloud top height every 15 minutes for the first thunderstorm and (bottom two panels) the same for the second thunderstorm. The first thunderstorm was dissipating (decreasing lightning activity and cloud area) at the start of the Early events whilst the second thunderstorm was intensifying (increasing lightning activity and cloud area). The proportion of cumulated peak current to number of flashes is seen to increase in the first thunderstorm at around 19 UTC.

#18). For all the detected events where the causative lightning was <400 km from the North-South path, $\frac{5}{8}$ are observable on at least one North-South path transmission. For causative lightning 400–500 km away, the proportion observable on the North-South path reduces to $\frac{4}{9}$ and for lightning that is farther away, the proportion is $\frac{1}{3}$.

Lightning discharge type (CG or IC) and polarity is also reported. For events with no coincident reported lightning, the determination of lightning type and polarity is still possible from the broadband radio waveforms. The broadband causative lightning waveforms were examined in three separate frequency bands - ELF (4 Hz–2 kHz), VLF (5–15 kHz) and LF (275–400 kHz) - by bandpass filtering. The causative lightning waveforms of all events except event #3 are +CG discharges with a continuing current component. Figure 4 shows a representative +CG waveform from event #1. Event #3 is presented in subsection 7.2.

The event with the largest magnitude disturbance (event #12 $\delta\varphi_i$ on DHO) also has the causative lightning with the highest reported peak current (456.29 kA). The slow continuing current component of this lightning seen from the radio receiver signal also has the longest duration of the causative lightning for all events. The lowest reported +CG peak current that produced any disturbance is 35.36 kA (event #7).

Additionally, 152 lightning flashes were observed by the BTD-300 sensor during this period even though the lightning located by Météorage in this period is >200 km away from the sensor situated in Portishead, suggesting that there were a number of exceptional lightning discharges. These discharges could have produced a sheet of enhanced conductivity above the thunderstorm that enabled the quasi-electrostatic signal to be detected from a longer range than expected [Bennett and Harrison, 2013, Bennett, 2014]. Of these, 7 were unambiguously coincident with early event causative lightning - these events are marked with a 'Y' in the column headed 'BTD' in table 1. Some of the BTD-300 signals were coincident with the events, but multiple flashes in the 1 s period before and after the event time and the time drift of the BTD-300 meant that the signal could not be identified unambiguously - these events are marked with 'a'. The largest reported peak current lightning of event #12 was not coincident with BTD-300 signals.

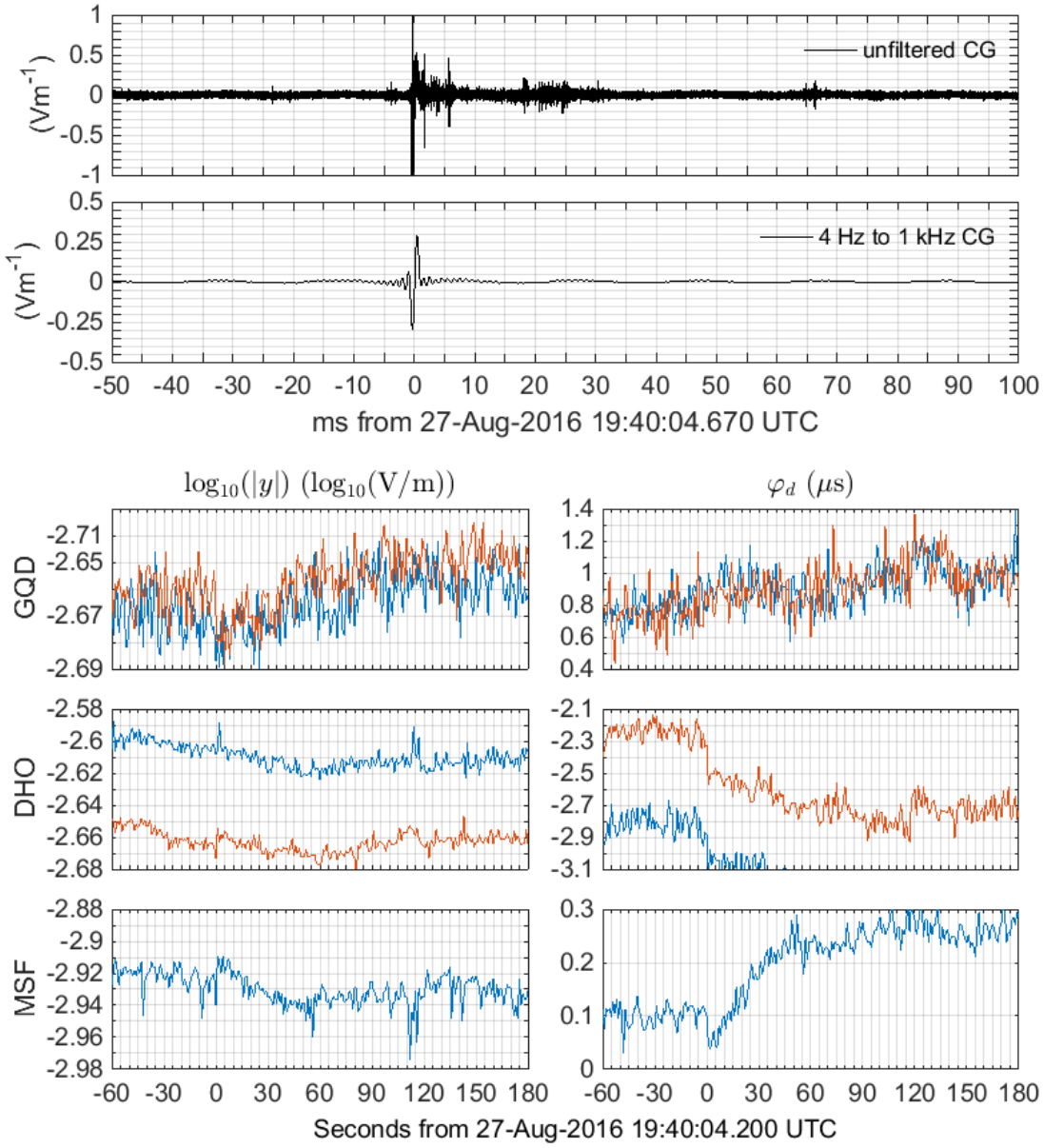

Fig. 4: Event #1 lightning and ionospheric signals. (Top) unfiltered and (second from top) 4 Hz to 1 kHz +CG waveform. The bottom panels show the (left) log amplitude and (right) phase change from GQD, DHO and MSF. The disturbance on DHO φ_i is seen to be a different shape to that for GQD and MSF. There was no disturbance seen on GBZ.

7 Example events

7.1 Event #01, 19:40:04.670 UTC

The causative lightning for this event was located over the North Sea (53.794°, 2.090°, location marked on figure 1) approximately 170 km from the DHO path and 330 km from the North-South path at the nearest points. The lightning waveform has a particularly strong ELF component as shown in the second panel from top of figure 4 - this is a feature of the causative lightning waveforms of all events except event #3.

There were disturbances on GQD, DHO and MSF for this event; these disturbances are shown in the bottom three rows in figure 4. The disturbance is clearest on the DHO lower sideband phase (red line), but can also be seen in other ionospheric signals, for example GQD amplitude and MSF phase. Features of the disturbance on DHO most closely match those of LORE events; no apparent recovery is seen, but the total length of the recovery is obfuscated by the phase disturbance of event #2 170 s later (not shown). The same event produced a very different disturbance signature on the separate North-South path. A drop in the GQD amplitude is followed by a recovery lasting ∼60 s before the signal stabilises at a post-event amplitude higher than pre-event. A similar signature is seen in the MSF phase; there is a phase decrease at the event onset which is followed by a ∼60 s recovery to a post-event phase that is higher than pre-event. No disturbance is seen on the GBZ ionospheric signal for this event.

There is some subjectivity in the estimation of the recovery times as the slow fluctuations in the ionospheric signals during night time conditions mean that it is difficult to estimate an ambient level, especially for longer recovery durations. Therefore, no attempt has been made to quantify the recovery times of these events. However, only disturbances that are clearly >10 s in duration have been identified as an event.

7.2 Event #03, 19:54:21.596 UTC

Figure 5 shows the signal from the radio receiver which is a 20 ms sferic burst with small ELF component. This causative lightning was not located although

discharges <1 s before and after were reported in the second thunderstorm over Netherlands on the DHO path, including a +CG 238 ms after with peak current of 50.51 kA. However, there is no way to be certain that these CG are related to the disturbance.

The rise time of the disturbance onset for this event is ∼300 ms, determined from the μs time resolution ionospheric signal disturbances on DHO and GQD amplitude and phase. This is shown in figure 5 with pre and post-event levels annotated. In this event, the onset rise is similar on the disturbances produced. It is not easy to clearly identify details of the disturbance onset from this signal due to (1) interference from the causative lightning at the onset of the event; (2) noise and variability of the ionosphere and; (3) the intermittent nature of the ionospheric signals due to the modulation of the transmissions. For example, when MSF is modulated 'off', its ionospheric signal cannot be determined. Similarly, for MSK modulated transmissions (GBZ, GQD and DHO), the transmitted signal switches between the higher and lower sidebands so that when one is transmitting, the other is effectively off. Thus, no attempt is made here to quantify the disturbance rise times for all events. However, the onset rise of this event is certainly not <20 ms and therefore cannot be categorised as Early/fast. In comparison with the other events in the data analysed, the rise time is not unusual. A number of events also produced disturbances with rise times that were hundreds of milliseconds long, although there were no clear Early/slow events with >500 ms rise times.

8 Discussion

The salient points from the observations can be summarised as:

(1) none of the events produced a disturbance on all the North-South path transmissions simultaneously. Further, the disturbance on an MSK modulated transmission may not be the same on its sidebands;

(2) the disturbances on the North-South path transmissions are caused by lightning discharges displaced from the propagation path by 330–600 km and for any one of the observed events, the located causative lightning is nearer to the DHO path (<380 km) than the North-South path; the likelihood of a transmission not being disturbed (given that there is a disturbance on another transmission) in-

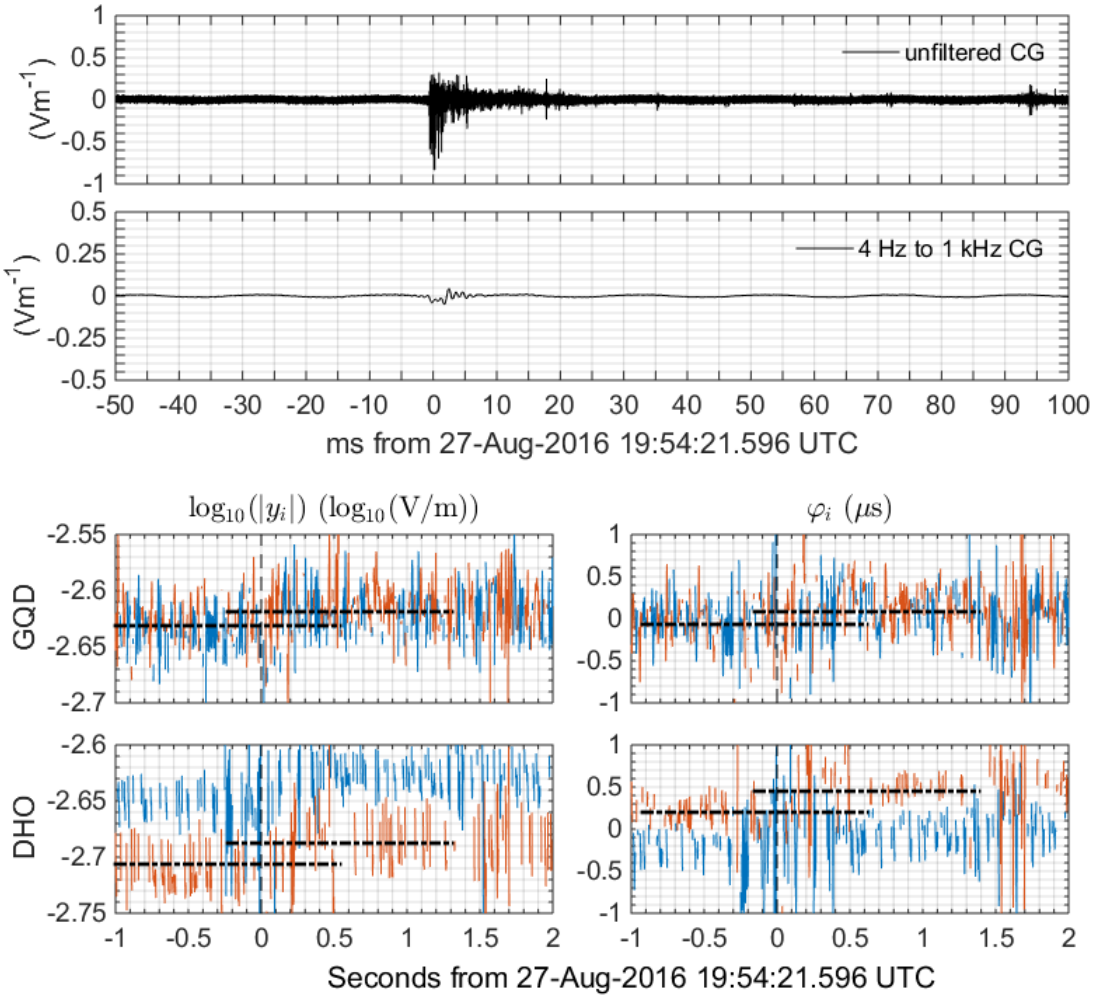

Fig. 5: Event #3 lightning and ionospheric signals. (Top) unfiltered and (second from top) 4 Hz to 1 kHz lightning waveform. The bottom panels show the high time resolution (left) log amplitude and (right) phase change from GQD and DHO. Approximate pre and post disturbance signal levels are shown in the thick broken lines.

creases with displacement distance of the causative lightning from the propagation path;

(3) except for an unidentified sferic burst, all identified causative lightning are +CG with peak currents 35.36–456.29 kA and continuing current;

(4) most of the causative lightning discharges occurred over the North Sea in the stratiform region of a decaying MCS;

The observation of point (1) shows that lightning ionospheric perturbations are frequency dependent in agreement with the modelling of [Marshall and Inan, 2010]. Disturbances can exhibit differences between even the smallest frequency separation between the ionospheric signals; for example, disturbances on GQD for events #1, 3 and 20 exhibit differences between the sidebands which are only 50 Hz apart. Without considering the specific physical mechanism for the ionospheric perturbation, from the detected events, the transmissions on the North-South path have a larger likelihood of being disturbed with decreasing displacement distance from causative lightning to propagation path. The implication is that disturbance frequency selectivity is stronger with increasing distance from the centre of the conductivity perturbation. This is probably a significant factor for DHO being disturbed by the majority of the events as the causative lightning of all the observed events are nearer to the DHO propagation path. Events #4 and #13 stand out as disturbing the North-South path transmissions but not DHO. DHO is also more sensitive to ionospheric changes as evidenced by the diurnal response [Koh et al., 2018b, figure 3] - accounting for the generally larger disturbances seen on DHO. The sensitivity of the propagation path to ionospheric changes can also determine the detectable threshold of disturbances resulting in more or less detections. The frequency selectivity and propagation path sensitivity highlight the importance of sensor geometry since the modal interference pattern formed on the ground by sub-ionospheric propagation is frequency dependent. This may have an impact on a number of investigations. For example, when considering the correspondence of early events with TLEs [Haldoupis et al., 2004, Marshall et al., 2006], perturbation imaging [Johnson et al., 1999] or constraining the conductivity of sprite plasma.

Considering simple geometries for lightning and thunderstorm charge structure, the ionospheric perturbation caused by lightning must be roughly centred above the causative discharge according to the proposed mechanisms of either EMP or

QE fields. Hence, the perturbations observed on the North-South path is either from the wide angle scattering of the transmissions off a low aspect ratio perturbation of high conductivity (i.e. sprite body) as proposed by [Dowden et al., 1996b] and termed 'VLF sprites' or; from forward scattering off a horizontally extensive conductivity perturbation. These can be produced by either the QE mechanism, for example, sprite halos [e.g., Inan et al., 1996, Moore et al., 2003] or lightning EMP [Inan et al., 1991, Taranenko et al., 1993, Mika et al., 2006]. Halos should not disturb propagation paths >150 km displaced from the causative lightning [Johnson et al., 1999, Moore et al., 2003]. Lightning EMP can produce thin (∼10 km) but horizontally extensive (up to 400 km radius) ionospheric perturbations [Barrington-Leigh et al., 2001, Marshall, 2012]. The displacement distances of causative lightning from the North-South path thus limits the probable mechanisms to lightning EMP and wide angle scattering off a sprite body.

For a thin horizontal perturbation patch, the sub-ionospheric propagation of a radio wave will not be disturbed if the bulk of its energy is reflected below the conductivity perturbation. This reflection of a radio wave in the ionosphere is dependent on the ionospheric conductivity and the radio wave frequency. For the D region ionosphere, the conductivity profile generally increases with height so that higher frequency radio waves are reflected at higher altitudes. Conversely, the perturbation will be transparent to the radio wave if the wave frequency is high relative to the electron density and collision frequency of the perturbed region. The MSF transmission has a frequency of 60 kHz compared to the 19.58 kHz and 22.1 kHz carrier frequencies of GBZ and GQD. Lightning EMP produce weak conductivity perturbations [Marshall, 2012, Kotovsky and Moore, 2017] at the edge of the night time reflection heights of ∼20 kHz transmissions so that frequency selective disturbances due to the perturbation altitude profile could be plausible. The height of optical emissions from EMP heating and ionisation of the ionosphere (ELVEs) have also been observed to range from 82–94 km including variations of up to 2 km on single nights [van der Velde and Montanyà, 2016]. Further, the distances of the causative lightning from the North-South propagation path means that the conductivity perturbation over the path is likely to be much weaker than nearer the causative lightning location. A corollary of the altitude dependence is that disturbances on higher frequencies should be longer in duration than on lower frequencies because the ionisation and temperature relaxation times of the

ionosphere increase with altitude but this is not seen clearly in the observations. Moreover, the reflection height variation with frequency is expected to be small, $<$2 km from 20–40 kHz [Marshall and Inan, 2010, section 3.3]. If the disturbances are due to lightning EMP, than the observations would mean the horizontal extent of such perturbations are larger than expected, especially as most of the causative lightning peak currents are not exceptional ($<$200 kA).

For wide angle scattering off a sprite body, the scattered wave forms an interference pattern on the ground that varies with azimuth angle and radial distance from the sprite that is dependent on the frequency of the incident wave [Rodger et al., 1997, Rodger and Nunn, 1999, Rodger et al., 1999]. Therefore, for given locations of transmitter, sprite and receiver such as with the North-South path transmissions, the disturbance would vary with frequency. The recovery should follow a logarithmic function [Dowden and Rodger, 1997]. For event #1 shown in figure 4, the disturbances on GQD amplitude and MSF phase does indeed exhibit roughly logarithmic recoveries if an extrapolation of the ambient ionospheric signal is made, however, this process is not neccesarily an objective measure (see subsection 7.1).

Causative lightning of the observed early events are found to be almost exclusively +CG in the stratiform region of a decaying MCS (first thunderstorm of the day) with the exception of the sferic burst producing event #3 (subsection 7.2). They also have significant ELF emissions associated with continuing current and charge moment change. These characteristics match those of sprite producing lightning [Soula et al., 2015]. These lightning were found from sub-ionospheric radio remote sensing independently of optical observations (which are unavailable), suggesting a strong relationship between the physical mechanisms. The sferic burst identified from event #3 is also linked to the production of sprites. These complex discharges were previously identified by [Johnson and Inan, 2000] from sub-ionospheric radio disturbances and subsequently observed to be linked to optical sprites [Ohkubo et al., 2005, van der Velde et al., 2006]. Three events (#16, 17, 18) were located in the second, intensifying thunderstorm in a 20 minute period. The short time window suggests conditions conducive to the production of ionospheric perturbations in a decaying MCS can exist briefly in an intensifying thunderstorm; a specific charge structure influencing the ionospheric conductivity profile above for example.

Lightning discharges that produce ELVEs from EMP exhibits correlation with peak current and rise times; above 50 kA, the probability of elves being detected from the flash increases sharply and at 100 kA the probability is >80% [Blaes et al., 2016]. They are also triggered by both +CG and -CG [Barrington-Leigh and Inan, 1999] such that it is probable that all high peak current CG produce EMP capable of modifying ionospheric conductivity. This is in contrast with the relatively even spread of the peak currents of lightning associated with the observed early events. Given that the second thunderstorm moved across the DHO path, the most likely scenario is that many elves were produced from this thunderstorm but not detected as radio disturbances. It is possible that there is a secondary condition necessary for lightning EMP to produce ionospheric perturbations that are detectable on sub-ionospheric radio, the ionospheric conductivity profile for example. The first thunderstorm is probably too far displaced from both propagation paths.

Further, 152 ionospheric perturbations of large horizontal extent were inferred from quasi-electrostatic measurements (BTD-300). These overlap a proportion of the identified causative lightning ($\frac{7}{22} \times 100\% \approx 32\%$), however, the quasi-electrostatically detected flashes show bias towards -CG. These events have been associated previously with halos [Bennett and Harrison, 2013, Bennett, 2014] and the statistical spread of lightning polarity concurs with that for halo production [Bering et al., 2004, Frey et al., 2007, Williams et al., 2012]. This points to a scenario where many halos were produced but also not detected as sub-ionospheric radio disturbances.

Therefore, the disturbances observed in this work are likely to be from sprite events via scattering off sprite plasma. Forward scattering from lightning ionospheric perturbations directly on the propagation path may yield different results for the frequency dependence and is yet to be investigated. The three events that were located <20 km from the DHO propagation could be from particularly strong halo conductivity perturbation since the perturbation is not distant from the propagation path and there were coincident quasi-electrostatic signals.

9 Summary

Observations of sub-ionospheric radio were made using a single wideband radio receiver along two different propagation paths; a North-South propagation path

375–398 km in length and an East-West path 704 km in length. The transmissions monitored were GBZ, GQD and MSF on the North-South path and DHO on the East-West path. The transmissions operate at a range of frequencies from 19.53–60 kHz. This is the first study using multiple frequencies on the same propagation path.

22 early events were identified from the radio data. The disturbances seen on the North-South path were not reciprocated across the transmissions on the path showing the frequency selectivity of ionospheric perturbations. Most of the events were detected on the DHO transmission as the causative lightning is much closer to this propagation path and the propagation is more sensitive to ionospheric changes. The frequency selectivity disturbances highlight the importance of transmission frequency in the detection of Early events.

Examination of the causative lightning reveal that they are similar to sprite producing lightning - they are predominantly +CG with strong ELF component occurring over the stratiform region of a decaying MCS. The lightning produced by the nearby thunderstorms (inferred from lightning location network reports and quasi-electrostatic measurements) should produce many more events from EMP and halo mechanisms. Thus, it is suggested that the propagation paths monitored are insensitive to conductivity perturbations from EMP and halo and instead, the disturbances seen are a result of sprites, potentially via wide angle scattering off sprite plasma.

10 Acknowledgements

The work of K.K. is sponsored by the Engineering and Physical Sciences Research Council 418 (EPSRC) under DTA contract EB-EE1151. The work of S.G. and A.P. is sponsored by the SAINT project of the European Commission (H2020-MSCA-ITN-2016, 722337). The work of M.F. is sponsored by the Natural Environment Research Council (NERC) under grants NE/L012669/1 and NE/H024921/1. The data used for this publication is available from https://doi.org/10.15125/BATH-00515. K.K. authored the paper, compiled contributions from co-authors, collected the radio data and performed the analysis of the transmissions. S.G. collated and performed the analysis of the meteorological and lightning

data. A.P. performed the analysis of the lightning from the radio data. A.B. provided the BTD-300 data and provided advice for the ideas in this paper. Z.L. assisted in the collection of the radio data. M.F. supervised the work of K.K., S.G. and A.P. Thanks also go to Météorage for providing the lightning data.

References

C. P. Barrington-Leigh and U. S. Inan. Elves triggered by positive and negative lightning discharges. *Geophys. Res. Lett.*, 26(6):683–686, March 1999. ISSN 1944-8007. doi: 10.1029/1999GL900059.

Christopher P. Barrington-Leigh, Umran S. Inan, and Mark Stanley. Identification of sprites and elves with intensified video and broadband array photometry. *J. Geophys. Res. Space Physics*, 106(A2):1741–1750, February 2001. ISSN 2156-2202. doi: 10.1029/2000JA000073.

A. J. Bennett. Identification and ranging of lightning flashes using co-located antennas of different geometry. *Meas. Sci. Technol.*, 24(12):125801, 2013. ISSN 0957-0233. doi: 10.1088/0957-0233/24/12/125801.

A. J. Bennett. Modification of lightning quasi-electrostatic signal by mesospheric halo generation. *Journal of Atmospheric and Solar-Terrestrial Physics*, 113: 39–43, June 2014. ISSN 1364-6826. doi: 10.1016/j.jastp.2014.03.010.

A. J. Bennett and R. G. Harrison. Lightning-Induced Extensive Charge Sheets Provide Long Range Electrostatic Thunderstorm Detection. *Phys. Rev. Lett.*, 111(4):045003, July 2013. doi: 10.1103/PhysRevLett.111.045003.

III Bering, E. A., L. Bhusal, J. R. Benbrook, J. A. Garrett, A. P. Jackson, E. M. Wescott, D. R. Moudry, D. D. Sentman, H. C. Stenbaek-Nielsen, and W. A. Lyons. The results from the 1999 sprites balloon campaign. *Advances in Space Research*, 34(8):1782–1791, January 2004. ISSN 0273-1177. doi: 10.1016/j.asr.2003.05.043.

P. R. Blaes, Robert A. Marshall, and Umran S. Inan. Global occurrence rate of elves and ionospheric heating due to cloud-to-ground lightning. *J. Geophys. Res. Space Physics*, 121(1):699–712, February 2016. ISSN 2169-9380. doi: 10.1002/2015JA021916.

Benjamin R. T. Cotts and Umran S. Inan. VLF observation of long ionospheric recovery events. *Geophys. Res. Lett.*, 34(14):L14809, July 2007. ISSN 1944-8007. doi: 10.1029/2007GL030094.

R. L. Dowden, C. D. D. Adams, J. B. Brundell, and P. E. Dowden. Rapid onset, rapid decay (RORD), phase and amplitude perturbations of VLF subionospheric transmissions. *Journal of Atmospheric and Terrestrial Physics*, 56(11):1513–1527, September 1994. ISSN 0021-9169. doi: 10.1016/0021-9169(94)90118-X.

R. L. Dowden, J. B. Brundell, and W. A. Lyons. Are VLF rapid onset, rapid decay perturbations produced by scattering off sprite plasma? *J. Geophys. Res.*, 101 (D14):19175–19183, August 1996a. ISSN 2156-2202. doi: 10.1029/96JD01346.

R. L. Dowden, J. B. Brundell, W. A. Lyons, and T. Nelson. Detection and location of red sprites by VLF scattering of subionospheric transmissions. *Geophys. Res. Lett.*, 23(14):1737–1740, July 1996b. ISSN 1944-8007. doi: 10.1029/96GL01697.

Richard L. Dowden and Craig J. Rodger. Decay of a vertical plasma column: A model to explain VLF sprites. *Geophys. Res. Lett.*, 24(22):2765–2768, November 1997. ISSN 1944-8007. doi: 10.1029/97GL02822.

R. C. Franz, R. J. Nemzek, and J. R. Winckler. Television Image of a Large Upward Electrical Discharge Above a Thunderstorm System. *Science*, 249 (4964):48–51, June 1990. ISSN 0036-8075, 1095-9203. doi: 10.1126/science.249.4964.48.

H. U. Frey, S. B. Mende, S. A. Cummer, J. Li, T. Adachi, H. Fukunishi, Y. Takahashi, A. B. Chen, R.-R. Hsu, H.-T. Su, and Y.-S. Chang. Halos generated by negative cloud-to-ground lightning. *Geophys. Res. Lett.*, 34(18), September 2007. ISSN 1944-8007. doi: 10.1029/2007GL030908.

H. Fukunishi, Y. Takahashi, M. Kubota, K. Sakanoi, U. S. Inan, and W. A. Lyons. Elves: Lightning-induced transient luminous events in the lower ionosphere. *Geophys. Res. Lett.*, 23(16):2157–2160, August 1996. ISSN 1944-8007. doi: 10.1029/96GL01979.

M. Füllekrug. Wideband digital low-frequency radio receiver. *Meas. Sci. Technol.*, 21(1):015901, January 2010. ISSN 0957-0233. doi: 10.1088/0957-0233/21/1/015901.

N. C. Gross, M. B. Cohen, R. K. Said, and M. Gołkowski. Polarization of Narrowband VLF Transmitter Signals as an Ionospheric Diagnostic. *J. Geophys. Res. Space Physics*, 123(1):901–917, January 2018. ISSN 2169-9402. doi: 10.1002/2017JA024907.

C. Haldoupis, T. Neubert, U. S. Inan, A. Mika, T. H. Allin, and R. A. Marshall. Subionospheric early VLF signal perturbations observed in one-to-one association with sprites. *J. Geophys. Res.*, 109(A10):A10303, October 2004. ISSN 2156-2202. doi: 10.1029/2004JA010651.

C. Haldoupis, R. J. Steiner, Á. Mika, S. Shalimov, R. A. Marshall, U. S. Inan, T. Bösinger, and T. Neubert. "Early/slow" events: A new category of VLF perturbations observed in relation with sprites. *J. Geophys. Res. Space Physics*, 111(A11), November 2006. ISSN 2156-2202. doi: 10.1029/2006JA011960.

Christos Haldoupis, Morris Cohen, Benjamin Cotts, Enrico Arnone, and Umran Inan. Long-lasting D-region ionospheric modifications, caused by intense lightning in association with elve and sprite pairs. *Geophys. Res. Lett.*, 39(16): L16801, August 2012. ISSN 1944-8007. doi: 10.1029/2012GL052765.

Christos Haldoupis, Morris Cohen, Enrico Arnone, Benjamin Cotts, and Stefano Dietrich. The VLF fingerprint of elves: Step-like and long-recovery early VLF perturbations caused by powerful ±CG lightning EM pulses. *J. Geophys. Res. Space Physics*, 118(8):5392–5402, August 2013. ISSN 2169-9402. doi: 10.1002/jgra.50489.

S. F. Hardman, C. J. Rodger, R. L. Dowden, and J. B. Brundell. Measurements of the VLF scattering pattern of the structured plasma of red sprites. *IEEE Antennas and Propagation Magazine*, 40(2):29–38, April 1998. ISSN 1045-9243. doi: 10.1109/74.683540.

U. S. Inan, T. F. Bell, and J. V. Rodriguez. Heating and ionization of the lower ionosphere by lightning. *Geophys. Res. Lett.*, 18(4):705–708, April 1991. ISSN 1944-8007. doi: 10.1029/91GL00364.

U. S. Inan, A. Slingeland, V. P. Pasko, and J. V. Rodriguez. VLF and LF signatures of mesospheric/lower ionospheric response to lightning discharges. *J. Geophys. Res. Space Physics*, 101(A3):5219–5238, March 1996. ISSN 2156-2202. doi: 10.1029/95JA03514.

U. S. Inan, S. A. Cummer, and R. A. Marshall. A survey of ELF and VLF research on lightning-ionosphere interactions and causative discharges. *J. Geophys. Res. Space Physics*, 115(A6):A00E36, June 2010. ISSN 2156-2202. doi: 10.1029/2009JA014775.

M. P. Johnson and U. S. Inan. Sferic clusters associated with early/Fast VLF events. *Geophys. Res. Lett.*, 27(9):1391–1394, May 2000. ISSN 1944-8007. doi: 10.1029/1999GL010757.

M. P. Johnson, U. S. Inan, S. J. Lev-Tov, and T. F. Bell. Scattering pattern of lightning-induced ionospheric disturbances associated with early/fast VLF events. *Geophys. Res. Lett.*, 26(15):2363–2366, August 1999. ISSN 1944-8007. doi: 10.1029/1999GL900521.

Kuang Liang Koh, Zhongjian Liu, and Martin Füllekrug. Lower ionosphere effects on narrowband VLF transmission propagation: Fast variabilities and frequency dependence. *Radio Sci.*, 2018a. doi: 10.1002/2017RS006456.

Kuang Liang Koh, Zhongjian Liu, Simon Ghilian, Alec Bennett, and Martin Füllekrug. Lower ionospheric conductivity modification during a convection surge. 2018b.

D. A. Kotovsky and R. C. Moore. Modeling long recovery early events (LOREs) produced by lightning-induced ionization of the nighttime upper mesosphere. *J. Geophys. Res. Space Physics*, 122(7):7761–7780, July 2017. ISSN 2169-9402. doi: 10.1002/2017JA023996.

Ningyu Liu, Matthew G. McHarg, and Hans C. Stenbaek-Nielsen. High-altitude electrical discharges associated with thunderstorms and lightning. *Journal of Atmospheric and Solar-Terrestrial Physics*, 136, Part A:98–118, December 2015. ISSN 1364-6826. doi: 10.1016/j.jastp.2015.05.013.

Zhongjian Liu, Kuang Liang Koh, Andrew Mezentsev, Sven-Erik Enno, Jacqueline Sugier, and Martin Füllekrug. Variable phase propagation velocity for long-range lightning location system. *Radio Sci.*, 51(11):1806–1815, November 2016. ISSN 1944-799X. doi: 10.1002/2016RS006058.

R. A. Marshall. An improved model of the lightning electromagnetic field interaction with the D-region ionosphere. *J. Geophys. Res. Space Physics*, 117(A3): A03316, March 2012. ISSN 2156-2202. doi: 10.1029/2011JA017408.

R. A. Marshall and U. S. Inan. Two-dimensional frequency domain modeling of lightning EMP-induced perturbations to VLF transmitter signals. *J. Geophys. Res.*, 115(A6):A00E29, June 2010. ISSN 2156-2202. doi: 10.1029/2009JA014761.

R. A. Marshall, U. S. Inan, and W. A. Lyons. On the association of early/fast very low frequency perturbations with sprites and rare examples of VLF backscatter. *J. Geophys. Res. Atmos.*, 111(D19):D19108, October 2006. ISSN 2156-2202. doi: 10.1029/2006JD007219.

R. A. Marshall, U. S. Inan, and V. S. Glukhov. Elves and associated electron density changes due to cloud-to-ground and in-cloud lightning discharges. *J. Geophys. Res. Space Physics*, 115(A4):A00E17, April 2010. ISSN 2156-2202. doi: 10.1029/2009JA014469.

Á Mika and C. Haldoupis. VLF Studies During TLE Occurrences in Europe: A Summary of New Findings. *Space Sci Rev*, 137(1-4):489–510, June 2008. ISSN 0038-6308, 1572-9672. doi: 10.1007/s11214-008-9382-8.

Á. Mika, C. Haldoupis, R. A. Marshall, T. Neubert, and U. S. Inan. Subionospheric VLF signatures and their association with sprites observed during EuroSprite-2003. *Journal of Atmospheric and Solar-Terrestrial Physics*, 67(16): 1580–1597, November 2005. ISSN 1364-6826. doi: 10.1016/j.jastp.2005.08.011.

Á. Mika, C. Haldoupis, T. Neubert, H. T. Su, R. R. Hsu, R. J. Steiner, and R. A. Marshall. Early VLF perturbations observed in association with elves. *Ann. Geophys.*, 24(8):2179–2189, September 2006. ISSN 1432-0576. doi: 10.5194/angeo-24-2179-2006.

Robert C. Moore, Christopher P. Barrington-Leigh, Umran S. Inan, and Timothy F. Bell. Early/fast VLF events produced by electron density changes associated with sprite halos. *J. Geophys. Res. Space Physics*, 108(A10), October 2003. ISSN 2156-2202. doi: 10.1029/2002JA009816.

S. NaitAmor, H. Ghalila, and M. B. Cohen. TLEs and early VLF events: Simulating the important impact of transmitter-disturbance-receiver geometry. *J. Geophys. Res. Space Physics*, 122(1):792–801, January 2017. ISSN 2169-9402. doi: 10.1002/2016JA022791.

A. Ohkubo, H. Fukunishi, Y. Takahashi, and T. Adachi. VLF/ELF sferic evidence for in-cloud discharge activity producing sprites. *Geophys. Res. Lett.*, 32(4): L04812, February 2005. ISSN 1944-8007. doi: 10.1029/2004GL021943.

Victor P. Pasko. Recent advances in theory of transient luminous events. *J. Geophys. Res. Space Physics*, 115(A6):A00E35, June 2010. ISSN 2156-2202. doi: 10.1029/2009JA014860.

Victor P. Pasko, Umran S. Inan, Yuri N. Taranenko, and Timothy F. Bell. Heating, ionization and upward discharges in the mesosphere, due to intense quasi-electrostatic thundercloud fields. *Geophys. Res. Lett.*, 22(4):365–368, February 1995. ISSN 1944-8007. doi: 10.1029/95GL00008.

Craig J Rodger. Subionospheric VLF perturbations associated with lightning discharges. *Journal of Atmospheric and Solar-Terrestrial Physics*, 65(5):591–606, March 2003. ISSN 1364-6826. doi: 10.1016/S1364-6826(02)00325-5.

Craig J. Rodger and David Nunn. VLF scattering from red sprites: Application of numerical modeling. *Radio Sci.*, 34(4):923–932, July 1999. ISSN 1944-799X. doi: 10.1029/1999RS900040.

Craig J. Rodger, James R. Wait, and Richard L Dowden. Electromagnetic scattering from a group of thin conducting cylinders. *Radio Science*, 32(3):907–912, May 1997. ISSN 0048-6604. doi: 10.1029/97RS00056.

Craig J. Rodger, Neil R. Thomson, and James R. Wait. VLF scattering from red sprites: Vertical columns of ionization in the Earth-ionosphere waveguide. *Radio Sci.*, 34(4):913–921, July 1999. ISSN 1944-799X. doi: 10.1029/1999RS900051.

H. T. Sampath, U. S. Inan, and M. P. Johnson. Recovery signatures and occurrence properties of lightning-associated subionospheric VLF perturbations. *J. Geophys. Res. Space Physics*, 105(A1):183–191, January 2000. ISSN 2156-2202. doi: 10.1029/1999JA900329.

D. D. Sentman, E. M. Wescott, D. L. Osborne, D. L. Hampton, and M. J. Heavner. Preliminary results from the Sprites94 Aircraft Campaign: 1. Red sprites. *Geophys. Res. Lett.*, 22(10):1205–1208, May 1995. ISSN 1944-8007. doi: 10.1029/95GL00583.

S. Soula, E. Defer, M. Füllekrug, O. van der Velde, J. Montanya, O. Bousquet, J. Mlynarczyk, S. Coquillat, J.-P. Pinty, W. Rison, P.r. Krehbiel, R. Thomas, and S. Pedeboy. Time and space correlation between sprites and their parent lightning flashes for a thunderstorm observed during the HyMeX campaign. *J. Geophys. Res. Atmos.*, 120(22):11552–11574, November 2015. ISSN 2169-8996. doi: 10.1002/2015JD023894.

Y. N. Taranenko, U. S. Inan, and T. F. Bell. Interaction with the lower ionosphere of electromagnetic pulses from lightning: Heating, attachment, and ionization. *Geophys. Res. Lett.*, 20(15):1539–1542, August 1993. ISSN 1944-8007. doi: 10.1029/93GL01696.

Neil R. Thomson, Mark A. Clilverd, and Craig J. Rodger. Midlatitude ionospheric D region: Height, sharpness, and solar zenith angle. *J. Geophys. Res. Space Physics*, 122(8):8933–8946, August 2017. ISSN 2169-9402. doi: 10.1002/2017JA024455.

Oscar A. van der Velde and Joan Montanyà. Statistics and variability of the altitude of elves. *Geophys. Res. Lett.*, 43(10):5467–5474, May 2016. ISSN 1944-8007. doi: 10.1002/2016GL068719.

Oscar A. van der Velde, Ágnes Mika, Serge Soula, Christos Haldoupis, Torsten Neubert, and Umran S. Inan. Observations of the relationship between sprite morphology and in-cloud lightning processes. *J. Geophys. Res.*, 111(D15): D15203, August 2006. ISSN 2156-2202. doi: 10.1029/2005JD006879.

Earle R. Williams, Cheng-Ling Kuo, József Bór, Gabriella Sátori, R. Newsome, Toru Adachi, Robert Boldi, Alfred B. Chen, E. Downes, Rue-Ron Hsu, Wal-

ter A. Lyons, M. M. F. Saba, Michael J Taylor, and Han-Tzong Su. Resolution of the sprite polarity paradox: The role of halos. *Radio Sci.*, 47(2), March 2012. ISSN 0048-6604. doi: 10.1029/2011RS004794.

Chapter 6

Concluding remarks

This PhD introduces a new signal processing technique that when allows a number of new insights about the lower ionosphere when applied to sub-ionospheric radio. The resolution provided by the new technique over narrow bandwidths such as those of man-made transmissions show a surprising non-linear frequency response. This frequency response changes with the diurnal cycle and also with fast disturbances such as those related to lightning. The technique reveals that short term $<$ 1s variability of the ionosphere is observable in sub-ionospheric radio and that this variability changes with time.

Experiments conducted to study lightning ionospheric perturbations in detail have provided new insights. A thunderstorm related disturbance that is not characteristic of typical lightning ionospheric perturbations was observed with multiple transmissions covering a frequency range 19.53–60 kHz. The features of this disturbance may be a result of the thunderstorm electrostatic field. More typical lightning ionospheric perturbations were also observed with these transmissions. The conditions in which these disturbances occurred are consistent with wide angle scattering off sprite plasma, a phenomenon that has received much attention previously due to conflicting observations.

The technique can be applied to further work in support of the imminent space missions of ASIM and TARANIS to study upper atmospheric lightning. The D region is also affected by many other sources of extraterrestrial origin, this technique can be applied in the study of these effects too. Generally, more observations are required, specifically with regards to the thunderstorm electrostatic field mech-

anism for ionospheric perturbation. Even though the experimental results are promising, modelling work would provide further physical insight, for example, to constrain sprite plasma conductivities needed for the wide angle scattering mechanism.

There are also still some basic questions about the technique that need investigation, particularly regarding transmitter effects. The technique effectively makes an educated guess of the transmitted signal to obtain a differential measurement with the received signal that is said to be from the ionosphere. In practice, some proportion of the signal may come from transmitter imperfections. This is important to quantify particularly to interpret the <1 s variabilities. Here, differential measurements with a receiver near the transmitter and a receiver at a remote site would help. Additionally, longer term comparisons with small array measurements can provide more insight into the radio propagation.

Bibliography

C. D. D. Adams and R. L. Dowden. VLF group delay of lightning-induced electron precipitation echoes from measurement of phase and amplitude perturbations at two frequencies. *J. Geophys. Res.*, 95(A3):2457–2462, March 1990. ISSN 2156-2202. doi: 10.1029/JA095iA03p02457.

W. C. Armstrong. Recent advances from studies of the Trimpi effect. *Antarctic journal of the United States*, 18(5):281–283, 1983.

Richard Barr. VLF wave generation using VLF heating and the cubic nonlinearity of the ionosphere. *Geophys. Res. Lett.*, 23(16):2165–2168, August 1996. ISSN 0094-8276. doi: 10.1029/96GL02024.

E. Blanc, F. Lefeuvre, R. Roussel-Dupré, and J. A. Sauvaud. TARANIS: A microsatellite project dedicated to the study of impulsive transfers of energy between the Earth atmosphere, the ionosphere, and the magnetosphere. *Advances in Space Research*, 40(8):1268–1275, January 2007. ISSN 0273-1177. doi: 10.1016/j.asr.2007.06.037.

F. Bourriez, J.-A. Sauvaud, J.-L. Pinçon, J.-J. Berthelier, and M. Parrot. A statistical study over Europe of the relative locations of lightning and associated energetic burst of electrons from the radiation belt. *Ann. Geophys.*, 34(1):157–164, February 2016. ISSN 1432-0576. doi: 10.5194/angeo-34-157-2016.

R. N. Bracewell. Numerical Transforms. *Science*, 248(4956):697–704, November 1990. ISSN 0036-8075, 1095-9203. doi: 10.1126/science.248.4956.697.

K. G. Budden. *The Propagation of Radio Waves: The Theory of Radio Waves of Low Power in the Ionosphere and Magnetosphere*. Cambridge University Press, University Press, Cambridge, UK, first paperback edition (with corrections) edition, 1988. ISBN 0 521 36952 2.

Ashot Chilingarian, Suren Chilingaryan, Tigran Karapetyan, Lev Kozliner, Yeghia Khanikyants, Gagik Hovsepyan, David Pokhsraryan, and Suren Soghomonyan. On the initiation of lightning in thunderclouds. *Scientific Reports*, 7(1):1371, May 2017. ISSN 2045-2322. doi: 10.1038/s41598-017-01288-0.

Mark A. Clilverd, Roger Duthie, Craig J. Rodger, Rachael L. Hardman, and Keith H. Yearby. Long-term climate change in the D-region. *Scientific Reports*, 7(1):16683, November 2017. ISSN 2045-2322. doi: 10.1038/s41598-017-16891-4.

S. A. Cummer, U. S. Inan, and T. F. Bell. Ionospheric D region remote sensing using VLF radio atmospherics. *Radio Sci.*, 33(6):1781–1792, November 1998. ISSN 1944-799X. doi: 10.1029/98RS02381.

R. L Dowden and C. D. D Adams. Ionospheric heating by VLF transmitters? *Journal of Atmospheric and Terrestrial Physics*, 54(7):1051–1059, July 1992. ISSN 0021-9169. doi: 10.1016/0021-9169(92)90071-R.

Joseph R. Dwyer and Martin A. Uman. The physics of lightning. *Physics Reports*, 534(4):147–241, January 2014. ISSN 0370-1573. doi: 10.1016/j.physrep.2013.09.004.

A. J. Elliot, H. E. Hughes, T. C. Hughes, T. E. Locker, R. Brown, C. Sarran, Y. Clewlow, V. Murray, A. Bone, M. Catchpole, B. McCloskey, and G. E. Smith. The impact of thunderstorm asthma on emergency department attendances across London during July 2013. *Emerg Med J*, 31(8):675–678, August 2014. ISSN 1472-0213. doi: 10.1136/emermed-2013-203122.

Thomas Farges, Elisabeth Blanc, and Michel Tanguy. Experimental evidence of D region heating by lightning-induced electromagnetic pulses on MF radio links. *J. Geophys. Res.*, 112(A10):A10302, October 2007. ISSN 2156-2202. doi: 10.1029/2007JA012285.

Declan L. Finney, Ruth M. Doherty, Oliver Wild, David S. Stevenson, Ian A. MacKenzie, and Alan M. Blyth. A projected decrease in lightning under climate change. *Nature Climate Change*, page 1, February 2018. ISSN 1758-6798. doi: 10.1038/s41558-018-0072-6.

G. J. Fishman, P. N. Bhat, R. Mallozzi, J. M. Horack, T. Koshut, C. Kouveliotou, G. N. Pendleton, C. A. Meegan, R. B. Wilson, W. S. Paciesas, S. J. Goodman,

and H. J. Christian. Discovery of Intense Gamma-Ray Flashes of Atmospheric Origin. *Science*, 264(5163):1313–1316, May 1994. ISSN 0036-8075, 1095-9203. doi: 10.1126/science.264.5163.1313.

R. C. Franz, R. J. Nemzek, and J. R. Winckler. Television Image of a Large Upward Electrical Discharge Above a Thunderstorm System. *Science*, 249(4964): 48–51, June 1990. ISSN 0036-8075, 1095-9203. doi: 10.1126/science.249.4964.48.

H. Fukunishi, Y. Takahashi, M. Kubota, K. Sakanoi, U. S. Inan, and W. A. Lyons. Elves: Lightning-induced transient luminous events in the lower ionosphere. *Geophys. Res. Lett.*, 23(16):2157–2160, August 1996. ISSN 1944-8007. doi: 10.1029/96GL01979.

Martin Füllekrug, Andrew Mezentsev, Robert Watson, Stéphane Gaffet, Ivan Astin, and Adrian Evans. Array analysis of electromagnetic radiation from radio transmitters for submarine communication. *Geophys. Res. Lett.*, 41(24): 9143–9149, 2014. ISSN 1944-8007. doi: 10.1002/2014GL062126.

Martin Füllekrug, Nathan Smith, Andrew Mezentsev, Robert Watson, Ivan Astin, Stéphane Gaffet, Adrian Evans, and Michael Rycroft. Multipath propagation of low-frequency radio waves inferred from high-resolution array analysis. *Radio Sci.*, 50(11):1141–1149, November 2015. ISSN 1944-799X. doi: 10.1002/2015RS005781.

Martin Füllekrug, Zhongjian Liu, Kuang Koh, Andrew Mezentsev, Stéphane Pedeboy, Serge Soula, Sven-Erik Enno, Jacqueline Sugier, and Michael J. Rycroft. Mapping lightning in the sky with a mini array. *Geophys. Res. Lett.*, 43(19): 10448–10454, October 2016. ISSN 1944-8007. doi: 10.1002/2016GL070737.

E. S. Gemelos, Umran S. Inan, M. Walt, Michel Parrot, and Jean-André Sauvaud. Seasonal dependence of energetic electron precipitation: Evidence for a global role of lightning. *Geophysical Research Letters*, 36(21), November 2009. ISSN 0094-8276. doi: 10.1029/2009GL040396.

E. A. Gerken, U. S. Inan, and C. P. Barrington-Leigh. Telescopic imaging of sprites. *Geophys. Res. Lett.*, 27(17):2637–2640, September 2000. ISSN 1944-8007. doi: 10.1029/2000GL000035.

N. C. Gross, M. B. Cohen, R. K. Said, and M. Gołkowski. Polarization of Narrowband VLF Transmitter Signals as an Ionospheric Diagnostic. *J. Geophys. Res. Space Physics*, 123(1):901–917, January 2018. ISSN 2169-9402. doi: 10.1002/2017JA024907.

A. V. Gurevich, G. M. Milikh, and R. Roussel-Dupre. Runaway electron mechanism of air breakdown and preconditioning during a thunderstorm. *Physics Letters A*, 165(5–6):463–468, June 1992. ISSN 0375-9601. doi: 10.1016/0375-9601(92)90348-P.

C. Haldoupis, R. J. Steiner, Á. Mika, S. Shalimov, R. A. Marshall, U. S. Inan, T. Bösinger, and T. Neubert. "Early/slow" events: A new category of VLF perturbations observed in relation with sprites. *J. Geophys. Res. Space Physics*, 111(A11), November 2006. ISSN 2156-2202. doi: 10.1029/2006JA011960.

Christos Haldoupis, Morris Cohen, Enrico Arnone, Benjamin Cotts, and Stefano Dietrich. The VLF fingerprint of elves: Step-like and long-recovery early VLF perturbations caused by powerful ±CG lightning EM pulses. *J. Geophys. Res. Space Physics*, 118(8):5392–5402, August 2013. ISSN 2169-9402. doi: 10.1002/jgra.50489.

Marc A. Higginson-Rollins and Morris B. Cohen. Exploiting LF/MF signals of opportunity for lower ionospheric remote sensing. *Geophys. Res. Lett.*, 44(16): 8665–8671, August 2017. ISSN 1944-8007. doi: 10.1002/2017GL074236.

U. S. Inan, D. C. Shafer, W. Y. Yip, and R. E. Orville. Subionospheric VLF signatures of nighttime D region perturbations in the vicinity of lightning discharges. *J. Geophys. Res.*, 93(A10):11455–11472, October 1988. ISSN 2156-2202. doi: 10.1029/JA093iA10p11455.

U. S. Inan, T. F. Bell, and J. V. Rodriguez. Heating and ionization of the lower ionosphere by lightning. *Geophys. Res. Lett.*, 18(4):705–708, April 1991. ISSN 1944-8007. doi: 10.1029/91GL00364.

U. S. Inan, D. Piddyachiy, W. B. Peter, J. A. Sauvaud, and M. Parrot. DEMETER satellite observations of lightning-induced electron precipitation. *Geophys. Res. Lett.*, 34(7):L07103, April 2007. ISSN 1944-8007. doi: 10.1029/2006GL029238.

U. S. Inan, S. A. Cummer, and R. A. Marshall. A survey of ELF and VLF research on lightning-ionosphere interactions and causative discharges. *J. Geophys. Res. Space Physics*, 115(A6):A00E36, June 2010. ISSN 2156-2202. doi: 10.1029/2009JA014775.

Umran S. Inan. VLF heating of the lower ionosphere. *Geophys. Res. Lett.*, 17(6): 729–732, May 1990. ISSN 1944-8007. doi: 10.1029/GL017i006p00729.

Umran S. Inan, Victor P. Pasko, and Timothy F. Bell. Sustained heating of the ionosphere above thunderstorms as evidenced in "early/fast" VLF events. *Geophys. Res. Lett.*, 23(10):1067–1070, May 1996. ISSN 1944-8007. doi: 10.1029/96GL01360.

M. P. Johnson, U. S. Inan, S. J. Lev-Tov, and T. F. Bell. Scattering pattern of lightning-induced ionospheric disturbances associated with early/fast VLF events. *Geophys. Res. Lett.*, 26(15):2363–2366, August 1999. ISSN 1944-8007. doi: 10.1029/1999GL900521.

R. Kabirzadeh, R. A. Marshall, and U. S. Inan. Early/fast VLF events produced by the quiescent heating of the lower ionosphere by thunderstorms. *J. Geophys. Res. Atmos.*, 122(12):2017JD026528, June 2017. ISSN 2169-8996. doi: 10.1002/2017JD026528.

Kuang Liang Koh, Simon Ghilian, Adam Peverell, Alec Bennett, Zhongjian Liu, and Martin Füllekrug. Multi-frequency observations of Early sub-ionospheric radio disturbances caused by lightning. 2018a.

Kuang Liang Koh, Zhongjian Liu, and Martin Füllekrug. Lower ionosphere effects on narrowband VLF transmission propagation: Fast variabilities and frequency dependence. *Radio Sci.*, 2018b. doi: 10.1002/2017RS006456.

Kuang Liang Koh, Zhongjian Liu, Simon Ghilian, Alec Bennett, and Martin Füllekrug. Lower ionospheric conductivity modification during a convection surge. 2018c.

Erin H. Lay and Xuan-Min Shao. High temporal and spatial-resolution detection of D-layer fluctuations by using time-domain lightning waveforms. *J. Geophys. Res.*, 116(A1):A01317, January 2011. ISSN 2156-2202. doi: 10.1029/2010JA016018.

Erin H. Lay, Xuan-Min Shao, and Abram R. Jacobson. D region electron profiles observed with substantial spatial and temporal change near thunderstorms. *J. Geophys. Res. Space Physics*, 119(6):4916–4928, June 2014. ISSN 2169-9402. doi: 10.1002/2013JA019430.

Ningyu Liu, Matthew G. McHarg, and Hans C. Stenbaek-Nielsen. High-altitude electrical discharges associated with thunderstorms and lightning. *Journal of Atmospheric and Solar-Terrestrial Physics*, 136, Part A:98–118, December 2015. ISSN 1364-6826. doi: 10.1016/j.jastp.2015.05.013.

Zhongjian Liu, Kuang Liang Koh, Andrew Mezentsev, Sven-Erik Enno, Jacqueline Sugier, and Martin Füllekrug. Lightning Sferics: Analysis of the Instantaneous Phase and Frequency Inferred from Complex Waveforms. *Radio Sci.*, 2018. doi: 10.1002/2017RS006451.

R. A. Marshall, U. S. Inan, and V. S. Glukhov. Elves and associated electron density changes due to cloud-to-ground and in-cloud lightning discharges. *J. Geophys. Res. Space Physics*, 115(A4):A00E17, April 2010. ISSN 2156-2202. doi: 10.1029/2009JA014469.

Andrew Mezentsev and Martin Füllekrug. Mapping the radio sky with an interferometric network of low-frequency radio receivers. *J. Geophys. Res. Atmos.*, 118(15):8390–8398, August 2013. ISSN 2169-8996. doi: 10.1002/jgrd.50671.

Robert C. Moore, Christopher P. Barrington-Leigh, Umran S. Inan, and Timothy F. Bell. Early/fast VLF events produced by electron density changes associated with sprite halos. *J. Geophys. Res. Space Physics*, 108(A10), October 2003. ISSN 2156-2202. doi: 10.1029/2002JA009816.

V. P. Pasko, U. S. Inan, and T. F. Bell. Sprites as luminous columns of ionization produced by quasi-electrostatic thundercloud fields. *Geophys. Res. Lett.*, 23(6): 649–652, March 1996. ISSN 1944-8007. doi: 10.1029/96GL00473.

V. P. Pasko, U. S. Inan, T. F. Bell, and Y. N. Taranenko. Sprites produced by quasi-electrostatic heating and ionization in the lower ionosphere. *J. Geophys. Res. Space Physics*, 102(A3):4529–4561, March 1997. ISSN 2156-2202. doi: 10.1029/96JA03528.

Victor P. Pasko. Electric jets. *Nature*, 423(6943):927–929, June 2003. ISSN 0028-0836. doi: 10.1038/423927a.

Victor P. Pasko. Recent advances in theory of transient luminous events. *J. Geophys. Res. Space Physics*, 115(A6):A00E35, June 2010. ISSN 2156-2202. doi: 10.1029/2009JA014860.

Victor P. Pasko, Umran S. Inan, Yuri N. Taranenko, and Timothy F. Bell. Heating, ionization and upward discharges in the mesosphere, due to intense quasi-electrostatic thundercloud fields. *Geophys. Res. Lett.*, 22(4):365–368, February 1995. ISSN 1944-8007. doi: 10.1029/95GL00008.

Victor P. Pasko, Umran S. Inan, and Timothy F. Bell. Ionospheric effects due to electrostatic thundercloud fields. *Journal of Atmospheric and Solar-Terrestrial Physics*, 60(7–9):863–870, May 1998a. ISSN 1364-6826. doi: 10.1016/S1364-6826(98)00022-4.

Victor P. Pasko, Umran S. Inan, and Timothy F. Bell. Spatial structure of sprites. *Geophys. Res. Lett.*, 25(12):2123–2126, June 1998b. ISSN 1944-8007. doi: 10.1029/98GL01242.

Victor P. Pasko, Mark A. Stanley, John D. Mathews, Umran S. Inan, and Troy G. Wood. Electrical discharge from a thundercloud top to the lower ionosphere. *Nature*, 416(6877):152–154, March 2002. ISSN 0028-0836. doi: 10.1038/416152a.

Victor P. Pasko, Yoav Yair, and Cheng-Ling Kuo. Lightning Related Transient Luminous Events at High Altitude in the Earth's Atmosphere: Phenomenology, Mechanisms and Effects. *Space Sci Rev*, 168(1-4):475–516, June 2012. ISSN 0038-6308, 1572-9672. doi: 10.1007/s11214-011-9813-9.

S. Pasupathy. Minimum shift keying: A spectrally efficient modulation. *IEEE Communications Magazine*, 17(4):14–22, July 1979. ISSN 0163-6804. doi: 10.1109/MCOM.1979.1089999.

Jianqi Qin, Sebastien Celestin, and Victor P. Pasko. On the inception of streamers from sprite halo events produced by lightning discharges with positive and negative polarity. *J. Geophys. Res. Space Physics*, 116(A6):A06305, June 2011. ISSN 2156-2202. doi: 10.1029/2010JA016366.

Vladimir A. Rakov, Martin A. Uman, and Rajeev Thottappillil. Review of lightning properties from electric field and TV observations. *J. Geophys. Res. Atmos.*, 99(D5):10745–10750, May 1994. ISSN 0148-0227. doi: 10.1029/93JD01205.

Henry Rishbeth and Owen K Garriott. *Introduction to Ionospheric Physics*, volume 14 of *International Geophysics*. Academic Press, Amsterdam, 1969. ISBN 978-0-12-588940-7. OCLC: 428097375.

William Rison, Paul R. Krehbiel, Michael G. Stock, Harald E. Edens, Xuan-Min Shao, Ronald J. Thomas, Mark A. Stanley, and Yang Zhang. Observations of narrow bipolar events reveal how lightning is initiated in thunderstorms. *Nat Commun*, 7:10721, February 2016. doi: 10.1038/ncomms10721.

David M. Romps, Jacob T. Seeley, David Vollaro, and John Molinari. Projected increase in lightning strikes in the United States due to global warming. *Science*, 346(6211):851–854, November 2014. ISSN 0036-8075, 1095-9203. doi: 10.1126/science.1259100.

Mohammad A. Salem, Ningyu Liu, and Hamid K. Rassoul. Modification of the lower ionospheric conductivity by thunderstorm electrostatic fields. *Geophys. Res. Lett.*, 43(1):5–12, January 2016. ISSN 1944-8007. doi: 10.1002/2015GL066933.

H. T. Sampath, U. S. Inan, and M. P. Johnson. Recovery signatures and occurrence properties of lightning-associated subionospheric VLF perturbations. *J. Geophys. Res. Space Physics*, 105(A1):183–191, January 2000. ISSN 2156-2202. doi: 10.1029/1999JA900329.

Clive Saunders. Charge Separation Mechanisms in Clouds. *Space Sci Rev*, 137 (1-4):335–353, April 2008. ISSN 0038-6308, 1572-9672. doi: 10.1007/s11214-008-9345-0.

Martin Schimmel and Hanneke Paulssen. Noise reduction and detection of weak, coherent signals through phase-weighted stacks. *Geophysical Journal International*, 130(2):497–505, August 1997. ISSN 1365-246X. doi: 10.1111/j.1365-246X.1997.tb05664.x.

B. F. J. Schonland, J. S. Elder, D. B. Hodges, W. E. Phillips, and J. W. van Wyk. The Wave Form of Atmospherics at Night. *Proceedings of the Royal Society of London A: Mathematical, Physical and Engineering Sciences*, 176(965):180–202, October 1940. ISSN 1364-5021, 1471-2946. doi: 10.1098/rspa.1940.0085.

U. Schumann and H. Huntrieser. The global lightning-induced nitrogen oxides source. *Atmos. Chem. Phys.*, 7(14):3823–3907, July 2007. ISSN 1680-7324. doi: 10.5194/acp-7-3823-2007.

C. F. Sechrist. Comparisons of techniques for measurement of D-region electron densities. *Radio Sci.*, 9(2):137–149, February 1974. ISSN 1944-799X. doi: 10.1029/RS009i002p00137.

Xuan-Min Shao, Erin H. Lay, and Abram R. Jacobson. Reduction of electron density in the night-time lower ionosphere in response to a thunderstorm. *Nature Geosci*, 6(1):29–33, January 2013. ISSN 1752-0894. doi: 10.1038/ngeo1668.

Israel Silber and Colin Price. On the Use of VLF Narrowband Measurements to Study the Lower Ionosphere and the Mesosphere–Lower Thermosphere. *Surv Geophys*, 38(2):407–441, March 2017. ISSN 0169-3298, 1573-0956. doi: 10.1007/s10712-016-9396-9.

M. T. Taner, F. Koehler, and R. E. Sheriff. Complex seismic trace analysis. *Geophysics*, 44(6):1041–1063, January 1979. ISSN 0016-8033, 1942-2156. doi: 10.1190/1.1440994.

Y. N. Taranenko, U. S. Inan, and T. F. Bell. Interaction with the lower ionosphere of electromagnetic pulses from lightning: Heating, attachment, and ionization. *Geophys. Res. Lett.*, 20(15):1539–1542, August 1993a. ISSN 1944-8007. doi: 10.1029/93GL01696.

Y. N. Taranenko, U. S. Inan, and T. F. Bell. The interaction with the lower ionosphere of electromagnetic pulses from lightning: Excitation of optical emissions. *Geophys. Res. Lett.*, 20(23):2675–2678, December 1993b. ISSN 1944-8007. doi: 10.1029/93GL02838.

B. D. H. Tellegen. Interaction between Radio-Waves? *Nature*, 131(3319):840, June 1933. ISSN 1476-4687. doi: 10.1038/131840a0.

Neil R. Thomson, Mark A. Clilverd, and Craig J. Rodger. Daytime midlatitude D region parameters at solar minimum from short-path VLF phase and amplitude. *J. Geophys. Res.*, 116(A3):A03310, March 2011. ISSN 2156-2202. doi: 10.1029/2010JA016248.

Neil R. Thomson, Mark A. Clilverd, and Craig J. Rodger. Midlatitude ionospheric D region: Height, sharpness, and solar zenith angle. *J. Geophys. Res. Space Physics*, 122(8):8933–8946, August 2017. ISSN 2169-9402. doi: 10.1002/2017JA024455.

Oscar A. van der Velde and Joan Montanyà. Statistics and variability of the altitude of elves. *Geophys. Res. Lett.*, 43(10):5467–5474, May 2016. ISSN 1944-8007. doi: 10.1002/2016GL068719.

H. D. Voss, W. L. Imhof, M. Walt, J. Mobilia, E. E. Gaines, J. B. Reagan, U. S. Inan, R. A. Helliwell, D. L. Carpenter, J. P. Katsufrakis, and H. C. Chang. Lightning-induced electron precipitation. *Nature*, 312(5996):740–742, December 1984. doi: 10.1038/312740a0.

H. D. Voss, M. Walt, W. L. Imhof, J. Mobilia, and Umran S. Inan. Satellite observations of lightning-induced electron precipitation. *Journal of Geophysical Research: Space Physics*, 103(A6):11725–11744, June 1998. ISSN 0148-0227. doi: 10.1029/97JA02878.

Earle Williams and Eugene Mareev. Recent progress on the global electrical circuit. *Atmospheric Research*, 135–136:208–227, January 2014. ISSN 0169-8095. doi: 10.1016/j.atmosres.2013.05.015.

C. T. R. Wilson. The electric field of a thundercloud and some of its effects. *Proc. Phys. Soc. London*, 37(1):32D, January 1924. ISSN 1478-7814. doi: 10.1088/1478-7814/37/1/314.